POLITECNICO DI TORINO

MASTER's Degree in AEROSPACE ENGINEERING

MASTER's Degree Thesis

n-BODY BALLISTIC ESCAPE WITH REVISITED WEAK STABILITY BOUNDARY CONCEPT FOR A MOON MARS TRANSFER

Supervisors

Prof. MANUELA BATTIPEDE

Dr. LUIGI MASCOLO

Candidate

GABRIELE MOCCIOLA

April 2024

A mia madre

Summary

In recent years, the next declared goal of the human race is landing on Martian soil and, in view of this, the roadmap to Mars envisages, as an intermediate step, the creation of a Moon Village in order to accumulate experience of extraterrestrial life, improving the technological and generation capabilities of energy sources outside our Earth. In light of this, the study carried out within this research work tries to explore possible ways for future unmanned supply missions to the Martian soil both in preparation for subsequent human exploration and for the creation of a possible Mars Village.

Therefore, this paper presents a minimum propellant study for an interplanetary trajectory from the Moon to Mars, focusing on exploiting Weak Stability Boundary (WBS) trajectories. The mission assumptions at departure include impulsive manoeuvres, N bodies perturbation, and JPL's DE440 ephemerides for the Moon and other celestial bodies position at epoch. The payload fraction is maximized via a genetic evolution method. The escape trajectory from the Earth-Moon binary sphere of influence towards Mars is optimized by a revised WSB trajectory that includes an Earth gravity assisted slingshot at departure. The epoch-dependent position of Mars and the cost to reach it from Earth are derived by solving the Lambert problem and by slicing isocurves at the threshold identifying solution at lower cost using WSB trajectories or traditional Earth-gravity assist strategies. The spacecraft state at the Earth-Moon sphere of influence is patched to the heliocentric leg, which evolves under Keplerian motion.

The analysis contains a study concerning the influence of solar pressure on the escape phase, with references to variations in velocity and energy, and based on the Sun-spacecraft relative position depending on the starting date. Results clearly show that there is a significant bifurcation phenomenon between using WSB trajectories and traditional Earth-gravity assist strategies. Future studies could explore the possibility of using Deimos and Phobos gravity assists to further optimize trajectories and reduce mission costs.

Ringraziamenti

"La conclusione di questo percorso ha per me un sapore agrodolce. Il traguardo è senza dubbio individuale e sancisce la fine di un capitolo della mia vita che mi riporta alla mente tante immagini di com'ero prima, prima di questi anni che mi hanno cambiato, e qualche immagine di come sarò. Soprattutto, mi riporta alla mente tante immagini di quello che sono oggi e delle persone che hanno formato il mio essere e che, giorno dopo giorno, mi fanno sentire in evoluzione; quindi no, non è solo un traguarda individuale. A fondo tesi, e con un animo diverso, ci sarà l'occasione di ringraziare chi mi ha accompagnato fino ad oggi con uno spirito leggero e che, con questo spirito, ha alleggerito le fatiche che, come accade per tutte le avventure, hanno accompagnato anche questa mia. Questo piccolo spazio però, mi piace dedicarlo a chi mi ha stupito più di tutti dando vita ad una rapporto che, nel corso di diversi anni di università, non avevo mai sentito così vero.

Professoressa Manuela Battipede, siamo in una scuola di ingegneria dove il lato tecnico troppo spesso oscura quello romantico. Potrei ringraziarla perché ha deciso di tenere vivo *un corso unico all'interno del panorama del Politecnico e che ha permesso, non soltanto a me, di appassionarci a un mondo di nicchia come quello dell'astrodinamica. Potrei ringraziarla perché ha fatto tutto questo con passione e con amore nei confronti dell'arte dell'insegnamento. Potrei ringraziarla perché nel corso di questo anno di tesi, spesso in ombra, ha seguito il nostro lavoro e ci ha sostenuti, ha creduto in noi e ci ha fatti sentire valorizzati. Scelgo di ringraziarla perché ha acceso in me quella* techne, *quel lato artistico di una ingegneria che non può e non deve essere mera tecnica. Le ore di lezione e i progetti di tesi passano ma le assicuro che queste sensazioni le porterò con me, come positività e passione."*

Caro Luigi, meglio Dottor Luigi Mascolo, provo a mantenere un briciolo di formalità ma allo stesso tempo non voglio fingere distacco né tantomeno perdere, neanche per un paragrafo, il rapporto che si è creato durante questi mesi. Non

capita tutti i giorni di trovare un professore così vicino agli studenti, questa è già merce rara per chi vuole capirlo, ma capita ancora meno spesso di poter trovare un mentore di cui potersi fidare nei momenti buoni e in quelli meno buoni. Un punto di riferimento. Ti ringrazio perchè hai saputo quando starci vicino e quando lasciarci liberi, perchè hai saputo valorizzarci come squadra e credere in noi come singoli. È stato un anno lungo e intenso, pieno di nuove responsabilità e ricco di esperienze inaspettate. Un anno che ho vissuto mai da solo, molto grazie a te. Non mi soffermo sulle tue conoscenze e capacità tecniche... quelle abbiamo provato a rubartele ma spesso non è stato facile!"

Acknowledgements

"The conclusion of this journey has a bittersweet taste for me. The achievement is undoubtedly individual and marks the end of a chapter of my life that brings back many images of how I was before, before these years that changed me, and some images of how I will be. Above all, it brings back many images of what I am today and of the people who have shaped my being and who, day after day, make me feel evolving; so no, it's not just an individual achievement. At the bottom of the thesis, and with a different spirit, there will be an opportunity to thank those who have accompanied me up to now with a light spirit and who, with this spirit, have lightened the burdens that, as happens for all adventures, have accompanied even this one of mine. However, I like to dedicate this small space to those who have amazed me the most, giving life to a relationship that, over several years of university, I had never felt so real."

Professor Manuela Battipede, we are in an engineering school where the technical side too often overshadows the romantic one. I could thank you because you decided to keep alive *a unique course within the panorama of the Polytechnic and that allowed, not only me, to become passionate about a niche world like that of astrodynamics. I could thank you because you did all this with passion and love for the art of teaching. I could thank you because during this thesis year, often in the shadows, you followed our work and supported us, believed in us and made us feel valued. I choose to thank you because you ignited in me that* techne*, that artistic side of an engineering that cannot and must not be mere technique. Lecture hours and thesis projects pass but I assure you that I will carry these feelings with me, as positivity and passion."*

Dear Luigi, better Dr. Luigi Mascolo, I try to maintain a hint of formality but at the same time I don't want to pretend detachment nor lose, not even for a paragraph, the relationship that has been created during these months. It's not

every day that you find a professor so close to the students, this is already a rare commodity for those who want to understand it, but it's even rarer to find a mentor you can trust in good times and bad. A reference point. I thank you because you knew when to be close to us and when to let us be free, because you knew how to value us as a team and believe in us as individuals. It's been a long and intense year, full of new responsibilities and rich in unexpected experiences. A year that I never lived alone, thanks to you very much. I won't dwell on your knowledge and technical skills... we've tried to steal them from you but often it wasn't easy!"

Table of Contents

List of Tables

List of Figures

Acronyms

2BP

Two-Body Problem

3BP

Three-Body Problem

CR3BP

Circular Restricted Three-Body Problem

EGA

Earth Gravity Assist

EM

Earth-Moon

EME2000

Earth Mean Equator and Equinox of Epoch J2000

EOM

Equation of Motion

GA

Genetic Algorithm

GEO

Geostationary Earth Orbit

GRACE

Gravity Recovery and Climate Experiment

HF

High Fidelity

HFOP

High Fidelity Orbit Propagator

HPOP

High Precision Orbit Propagator

IAU

International Astronomical Union

ICRF

International Celestial Reference Frame

ICRS

International Celestial System

IVP

Initial Value Problem

JPL

Jet Propulsion Laboratory

LEO

Low Earth Orbit

LO

Lunar Orbit

LP

Lagrange Point

MGA

Moon Gravity Assist

NAIF

Navigation and Ancillary Information Facility

NASA

National Aeronautics and Space Administration

NBP

n-Body Problem

ODE

Ordinary Differential Equation

PCR3BP

Planar Circular Restricted Three-Body Problem

RF

Reference Frame

RKF

Runge-Kutta-Fehlberg

RS

Reference System

SC

Spacecraft

SME

Specific Mechanical Energy

SOI

Sphere of Influence

SPICE

Spacecraft Planet Instrument Camera-matrix Events

TPBVP

Two Points Boundary Value Problem

WSB

Weak Stability Boundary

WO

Waiting Orbit

Chapter 1

Introduction

In the most fervent years of space exploration, the avowed goal of this and future generations is the human landing on Martian soil and, with it, the conquest of an extraterrestrial independence that is as much a sign of strength as it is of hope, so that a life beyond our cradle is possible. In order for human settlement on Mars to be functional and sustainable, in addition to the realisation of manned missions to the red planet, it is necessary to envisage what resources may be required to build a living and liveable environment and optimise their interplanetary expedition: communication technologies, life-support systems, space habitats, food and energy production systems as well as surface vehicles and radiation protection technologies will be necessary.

With this in mind, and attempting to respond to this need, the present paper proposes to study a low-cost Moon-Mars transfer by exploiting and readapting the concept of Weak Stability Boundary (WSB) to the n-Body Problem (NBP). The research work carried out and reported here has investigated, in particular detail, the phase of escape from the sphere of influence of the Earth-Moon complex from a lunar orbit (LO) with the aim of minimising the required delta-V. The study carried out was organised in two phases.

At first, out of a desire to better understand the WSB concept and, at the same time, to lighten the computational cost, it was decided to model the motion in the Planar Circular Restricted 3-Body Problem (PCR3BP) on which an ad hoc genetic algorithm was stitched. The PCR3BP has been employed as the chosen model for describing the dynamics of a minute particle within the Earth-Moon system. In this particular framework, relative to an inertial reference frame, two primary celestial bodies, denoted as P1 and P2 with masses $m1 > m2 > 0$, respectively, execute circular orbits around their common centre of mass, influenced solely by their mutual gravitational interaction. A third body, represented as P3(standing as the spacecraft) and regarded as having infinitesimal mass, moves within the same plane as the primaries, experiencing gravitational forces from P1 and P2.

Importantly, the motion of this infinitesimal mass, corresponding to a spacecraft in our context, does not perturb the orbits of the primary bodies, which stand for the Earth and the Moon. This is where the concept of WSB takes shape, i.e. a region in the phase space of a dynamical system in which orbits can be weakly stable. In this context, invariant manifolds are geometric spaces that remain unchanged under the action of a dynamical map or flow and assume importance because they can define boundaries or separations between different stability regions of the dynamical system. The exploitation of these regions allows the design of low-energy missions.

This approach, although functional at an embryonic stage of the work and useful for carrying out a large number of simulations, proved to be incomplete. To achieve a comprehensive and high-fidelity trajectory optimization, it becomes essential to utilize a dynamical system that closely approximates the complexities of the actual solar system. This entails accounting for all gravitational influences, perturbations, and phenomena originating from various celestial bodies within the solar system. For this purpose, we employ JPL's DE440 planetary ephemerides within the framework of the NBP dynamical system. This dynamical model encompasses the gravitational interactions of a complete-body system, consisting of the Sun, Earth, Moon, and the spacecraft itself as well as other celestial bodies in the solar system itself, while also addressing various additional perturbations and effects, which will be elaborated upon in subsequent sections.

Once the physical model, CR3BP or NBP as it may be, the trajectory search was carried out using a Genetic Algorithm (GA) stitched onto the model itself and based on a merit function that would naturally direct evolution towards the desired results. Within the GA, the different candidates are represented as combinations of four different genes that, randomly shuffled together, lead to the creation of a pilot population (first generation) from whose evolution subsequent generations will be born. Using offspring, ex novo generation, more or less forced mutation, crossover and recombination operators and exclusion of individuals deemed unsuitable, the mass of candidates evolves towards compliance with the imposed figures of merit. The GA assumed a pivotal role in our study, facilitating the generation of diverse yet comparable outcomes.

This approach enabled to conduct a comprehensive analysis, not only of individual solutions but also of the broader spectrum of potential trajectories stemming from a shared initial concept. Our emphasis extended beyond singular trajectories, encompassing a collective exploration of different trajectories, all originating from the same fundamental concept. This approach afforded a valuable opportunity for critical evaluation and comparison. As elaborated upon in the subsequent section dedicated to results and analysis, this study has unveiled the potential for executing escape manoeuvres from the sphere of influence of the Earth-Moon system, originating from low lunar orbits. This manoeuvre leverages a gravitational interdiction zone and entails a delta-V expenditure of approximately 400 m/s

enabling a ballistic escape manoeuvre.

Chapter 2

Dynamics Model

"Nec fas est propius mortali attingere Divos"

-Edmond Halley

2.1 Reference System

In the scope of this work, as clearly explained in [1], the geocentric equatorial Reference System(RS) aligns precisely with the Earth Mean Equator and Equinox of Epoch J2000(EME2000), which will also be referred to more simply as J2000. The analysis leverages JPL ephemerides from the DE4xx series, with a specific focus on the JPL DE440 dataset. Notably, these ephemerides are referenced in the International Celestial Reference Frame(ICRF) and encompass nutational and librational phenomena. Historically, these intrinsic wobbling effects have conferred upon the EME2000 Reference Frame(RF), also recognized as J2000, a quasi-inertial characterization.

However, it is essential to acknowledge that the rotational offset between the ICRF and the dynamical EME2000 amounts to a mere hundredth of an arcsecond. Consequently, the EME2000 RF is now unequivocally regarded as inertial.

2.1.1 International Celestial Reference Frame

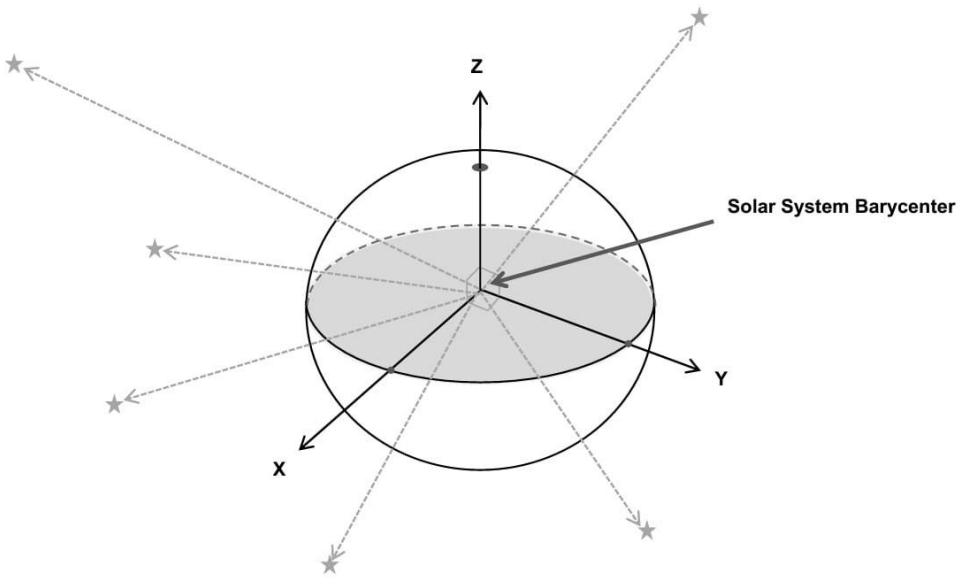

Figure 2.1: ICRF

The International Celestial Reference System (ICRS) is the current standard celestial reference system adopted by the International Astronomical Union (IAU) starting from the XXIII General Assembly held on 20 August 1997 in Kyoto, Japan [2]. Its origin is at the barycenter of the Solar System, and its axes are intended to show no global rotation with respect to a set of distant extragalactic objects.

The ICRF is a realization of the ICRS using reference extragalactic radio sources observed at radio wavelengths.

Thus, the main objective of the ICRF is to provide a reference frame that is conceptually independent of the Earth's motion in space. The ICRF forms the stable reference points from which the orientation of the Earth in three dimensional space can be measured.

This reference frame is widely used for navigation both on Earth and in space and is a starting point for astrophysical observations.

2.1.2 Earth Mean Equator and Equinox of Epoch J2000

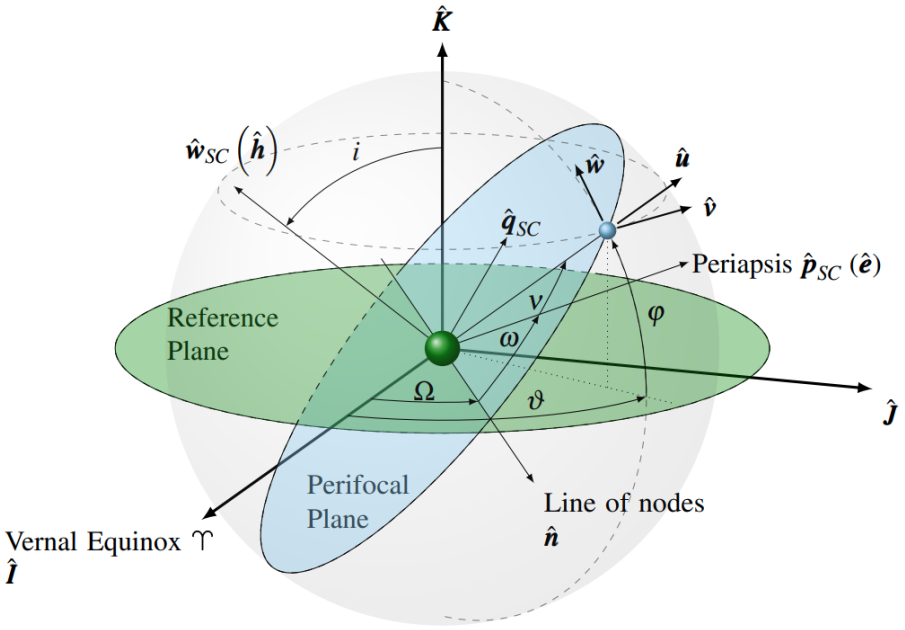

Figure 2.2: EME2000 RF [1]

As shown in the figure 2.2, the equatorial plane is the reference plane of the J2000 system. The axis $\hat{\boldsymbol{I}}$ lies on the reference plane along the direction of the vernal equinox, while the axis $\hat{\boldsymbol{K}}$ is normal to the mean equator of date at epoch J2000 TDB, which is approximately Earth's spin axis orientation at that epoch. The axis $\hat{\boldsymbol{J}}$ completes the right-hand triad.

The line of nodes is defined as the intersection of the reference plane and the perifocal plane (plane on which the orbit lies).

2.2 Historical background

"In outlining a quick historical background to astrodynamics, reference is made to the paper The History and Background of Astrodynamics, focusing on the aspects most pertinent to the present discussion".[3]

Celestial mechanics is centuries-old knowledge rooted in the history of human civilisation, from Ancient Greece to the present day.

Although this curiosity has always burdened the thinking of the sharpest minds, the figure of *sir Isaac Newton* remains to this day a watershed figure who marked

the birth of astrodynamics. In this sense, it is possible to identify four main periods:

(1) The pre-Newtonian period, beginning with Aristoteles and ending with Galileo;

(2) The Classical(or Newtonian) period, beginning with Newton and ending with Hamilton;

(3) The "modern" period, the 19th century;

(4) The contemporary period, until today.

2.2.1 The Pre-Newtonian Period

The first(long) years led to a broad and deep philosophical discernment of the subject with rare excursions of a more mathematical nature.

It was between the second half of the 15th century and the first half of the 16th that *Copernicus*(1473-1543) proposed an early heliocentric model (as convenient for calculating planetary orbits).

In the years that followed, his circular orbits were improved by *Kepler*(1571-1630) who, by introducing the concept of an elliptical orbit, arrived at the definition of his laws of planetary motion (Kepler's Laws) using the *Tycho Brahe*'s(1545-1601) observational results .

(i) *First Kepler's law* - The orbit of a planet is elliptical (so it lies on a plane) and the Sun occupies one of the foci of the ellipse;

(ii) *Second Kepler's law* - The planet-Sun line sweeps equal areas at equal times;

(iii) *Third Kepler's law* - The square of the period of revolution of a planet is proportional to the cube of the average distance from the Sun.

2.2.2 The Classical Newtonian Period

The figure of Newton(1642-1727) brought a great revolution to the scientific world, introducing a new dynamic and a new meaning of science.

Limiting himself to aspects directly related to astrodynamics, Newton is credited with having been able to connect distant phenomena(legend of the apple - elliptical orbits). With his *Principia*(1687), Newtonian Mechanics was born and he conceived the three laws of motion.

I law - The law of Inertia

"Objects in motion tend to stay in motion, and objects at rest tend to stay at rest unless an outside force acts upon them".

II law

"The rate of change of the momentum of a body is directly proportional to the net force acting on it, and the direction of the change in momentum takes place in the direction of the net force".

$$\sum \vec{F} = \frac{d(m\dot{\vec{r}})}{dt} = m\ddot{\vec{r}}^{*} \tag{2.1}$$

*assuming mass as constant

Following at the Newton original formulation, it's surprising how he haven't connected force with acceleration, but with the change of momentum: this allows the direct application of Newton's laws to the variable mass equations and rocket propulsion.

III law - Conservation of Momentum

"To every action (force applied) there is an equal but opposite reaction (equal force applied in the opposite direction)".

Law of Universal Gravitation

Besides these three fundamental laws, Isaac Newton've also conceived the *law of graviting* as it follow.

"Every point mass(M) attracts every other point mass(m) by a force acting along the line intersecting the two points. The force magnitude($\left|\vec{F}_g\right|$) is proportional to the product of the two masses, and inversely proportional to the square of the distance(r) between them".

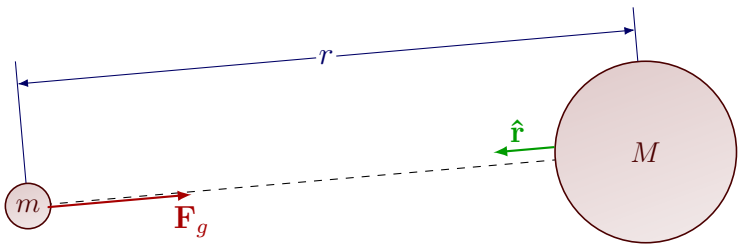

Figure 2.3: Newton's Law of Gravity

$$\vec{F}_g = -\frac{GMm}{r^2}\frac{\vec{r}}{r} \tag{2.2}$$

where G refers to the Universal Gravitational Constant and has the value of $6{,}67 \cdot 10^{-11} Nm^2/kg^2$.

Applying the equation 2.2 to the equation 2.1,it is possible to obtain the EOM of planets and satellites.

2.3 Hints at the Two-Body Problem

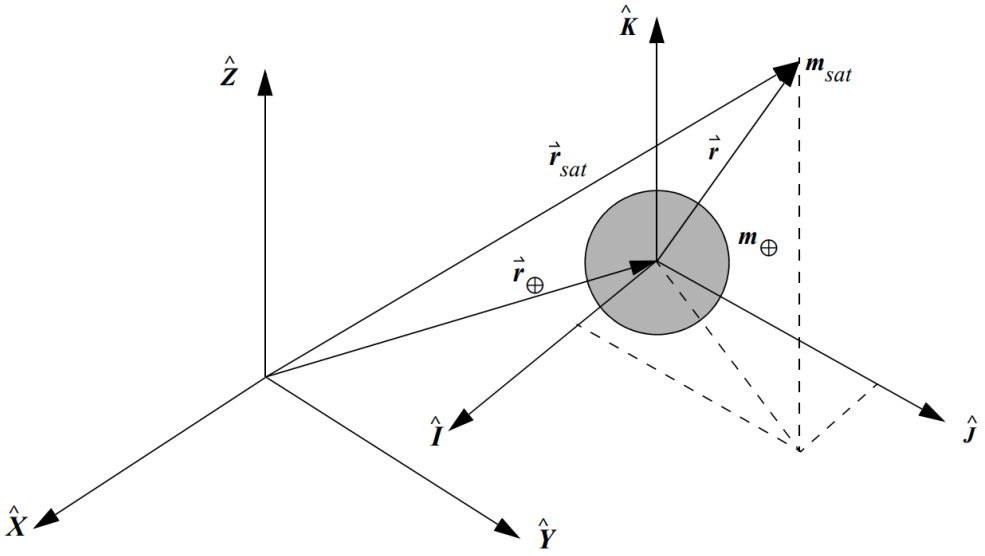

Figure 2.4: Geometry for Two Bodies in an Inertial Reference Frame [4]

Starting from Newton's second law, it is possible to derive equation 2.6 a (equation of the two-body problem) by considering the rayvectors describing the position of the two masses with respect to an inertial XYZ reference system [4], as shown in Figure 2.4.

For the sake of practicality in the discussion, the Earth will be considered for illustrative purposes as the primary (more massive) body and the spacecraft as the secondary body.

$$\vec{r}_{\oplus SC} = \vec{r}_{SC} - \vec{r}_{\oplus} \tag{2.3}$$

The importance of the inertial coordinate system is apparent now because it allows us to differentiate this vector equation without considering the derivatives of each axis of the coordinate system.

$$\ddot{\vec{r}}_{\oplus SC} = \ddot{\vec{r}}_{SC} - \ddot{\vec{r}}_{\oplus} = \ddot{\vec{r}} \tag{2.4}$$

By referring to equation 2.2 and factoring out, it is possible to write:

$$\ddot{\vec{r}} = -\frac{G(m_{\oplus} + m_{SC})}{r^2}\frac{\vec{r}}{r} \tag{2.5}$$

At this point it makes sense to consider the satellite's mass negligible in relation to the more massive gravitational body and to introduce the Earth's gravitational parameter $\mu_{\oplus} = Gm_{\oplus}$:

$$\ddot{\vec{r}} = -\frac{\mu_{\oplus}}{r^2}\frac{\vec{r}}{r} \tag{2.6}$$

This is the equation for the two-body problem and is only valid under certain assumptions:

1. The mass of the satellite is negligible compared to that of the attracting body. This is reasonable for artificial satellites in the foreseeable future;
2. The coordinate system chosen for a particular problem is inertial. This hypotesis allows to remove derivatives of the coordinate system itself when differentiating vectors;
3. The bodies of the satellite and attracting body are spherically symmetrical, with uniform density. This allows us to treat each as a point mass;
4. No other forces act on the system except for gravitational forces that act along a line joining the centers of the two bodies.

Within this dynamic model, the equation 2.6 governs the motion of bodies describing ideal orbits in space. The introduction of perturbations (new gravitational influences, asymmetries, solar radiation pressure, etc.) complicates the problem and requires the introduction of the perturbative term itself within the equations of motion.

2.3.1 Specific Angular Momentum

The angular momentum for an orbit is a variable that is independent of the mass of the principal body and is a characteristic of the orbit, as it is constant for the orbit. Both its vector and scalar nature are derived and described below.

Start by multiplying the terms in the equation 2.6 by the radiusvector $\vec{r}$:

$$\vec{r} \wedge \ddot{\vec{r}} + \vec{r}\frac{\mu_{\oplus}}{r^3}\vec{r} = 0 \tag{2.7}$$

Because of $\vec{r} \wedge \vec{r} = 0$, the second term of the equation disappeares. Considering

$$\frac{d}{dt}(\vec{r} \wedge \dot{\vec{r}}) = \vec{r} \wedge \ddot{\vec{r}} + \dot{\vec{r}} \wedge \dot{\vec{r}} = \vec{r} \wedge \ddot{\vec{r}} \tag{2.8}$$

then, substituting, it is possible to write

$$\frac{d}{dt}(\vec{r} \wedge \dot{\vec{r}}) = 0 \implies \vec{r} \wedge \dot{\vec{r}} = constant \tag{2.9}$$

By replacing $\dot{\vec{r}}$ with the velocity vector $\vec{v}$ the specific angular momentum vector is made explicit

$$\vec{h} = \vec{r} \wedge \vec{v} \tag{2.10}$$

Notice how the vector $\vec{h}$, being the vector product between position and velocity, is always perpendicular to the plane of the orbit (plane to which the satellite is constrained under the assumptions of the two-body problem). It is also evident how, once a given pair of $\vec{r}$ and $\vec{v}$ is given, the specific angular momentum will be univocally determined.

The magnitude can be written as

$$h = r^2 \dot{v} \tag{2.11}$$

Or alternatively, by referring to orbital parameters such as semilatus rectum p, semi-major axis a and eccentricity e of the orbit, can be deduced from the following relation:

$$p = \frac{h^2}{\mu_{\Theta}} = a(1 - e^2) \qquad h = \sqrt{\mu_{\Theta} p} \tag{2.12}$$

2.3.2 Specific Mechanical Energy

The specific mechanical energy (SME) is also independent of mass and is a constant identifying the orbit. To derive it, we follow a similar path as in the previous subsection.

Begin by rewriting the equation 2.6 in terms of the velocity vector and multiplying both members by $\dot{\vec{r}} = \vec{v}$

$$\vec{v} \wedge \dot{\vec{v}} + \vec{v} \frac{\mu_{\Theta}}{r^3} \vec{r} = 0 \tag{2.13}$$

By rewriting, one comes to

$$v\dot{v} + \dot{r} \frac{\mu_{\Theta}}{r^3} r = 0 \tag{2.14}$$

Recognising the remarkable derivatives and integrating the terms of the resulting equation, we can write the *visviva equation*:

$$\mathscr{E} = \frac{v^2}{2} - \frac{\mu_{\Theta}}{r} + c \tag{2.15}$$

$\mathscr{E}$ varies with height and speed and is zero at the Earth's surface. In astrodynamics c is defined to be zero.

$$\mathscr{E} = \frac{v^2}{2} - \frac{\mu_\oplus}{r} = -\frac{\mu_\oplus}{2a} \tag{2.16}$$

Using this definition, the same concept still applies: the higher and faster you go, the more your energy increases. However, you start with a negative value for energy when at rest at the surface of the Earth. [4]

It is also possible to look at the definition of specific mechanical energy 2.16 as the difference between a kinetic term and a potential term. A consequence of this definition is the concept of Sphere of Influence (SOI). The SOI of a central (ideally symmetrical) body is that region of space, precisely spherical, within which the body itself is solely responsible for all orbital motions. Outside the aforementioned SOI, other celestial bodies have a greater influence on the spacecraft's motion.

$$r_{SOI} = a_{ES}\left(\frac{m_\oplus}{m_\odot}\right)^{2/5} \tag{2.17}$$

The one given in the equation 2.17 is a good approximation. The value of the radius of the SOI r_{SOI} is a function of the masses of the two massive bodies and the distance between them a_{ES}.

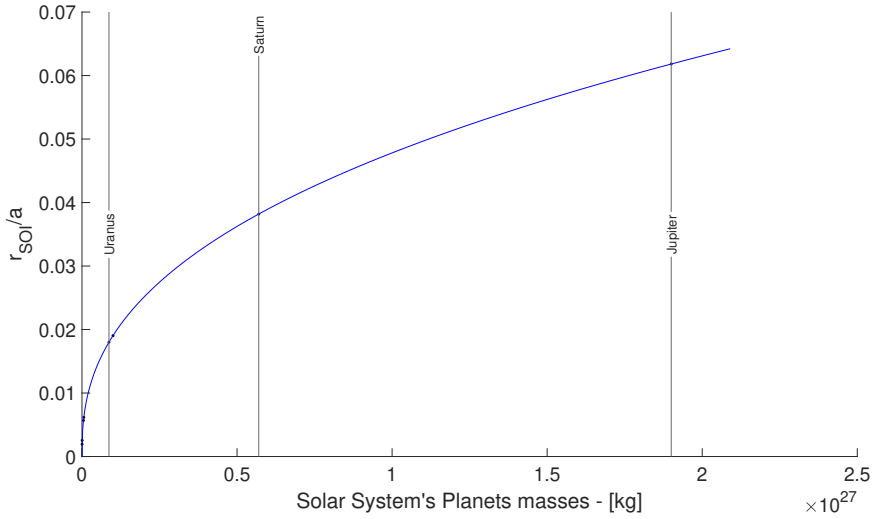

Figure 2.5: r_{SOI}/a vs planets' masses

In Fig. 2.5, the trend relative to the approximation of equation 2.17 is shown.

Planet //	Mass [kg] $\cdot 10^{24}$	Distance from ☉ [AU]	Distance from ☉ [km]$\cdot 10^6$	SOI [km]$\cdot 10^6$
Mercury	0.33	0.39	57.9	0.117
Venus	4.867	0.723	108.2	0.616
Earth	5.972	1	149.6	0.929
Mars	0.65	1.524	227.9	0.578
Jupiter	1900	5.203	778.3	48.2
Saturn	570	9.539	1427.0	54.5
Uranus	87	19.18	2871.0	51.9
Neptune	100	30.06	4497.1	86.2

Table 2.1: Solar System's SOI

The table 2.1 shows values of interest for the Solar System and its celestial bodies.

2.3.3 Hohmann Transfer

Walter Hohmann (1880–1945) proposed a theory which suggested the minimum change in velocity transfer could be achieved between orbits by using two tangential burns(Hohmann, 1925).

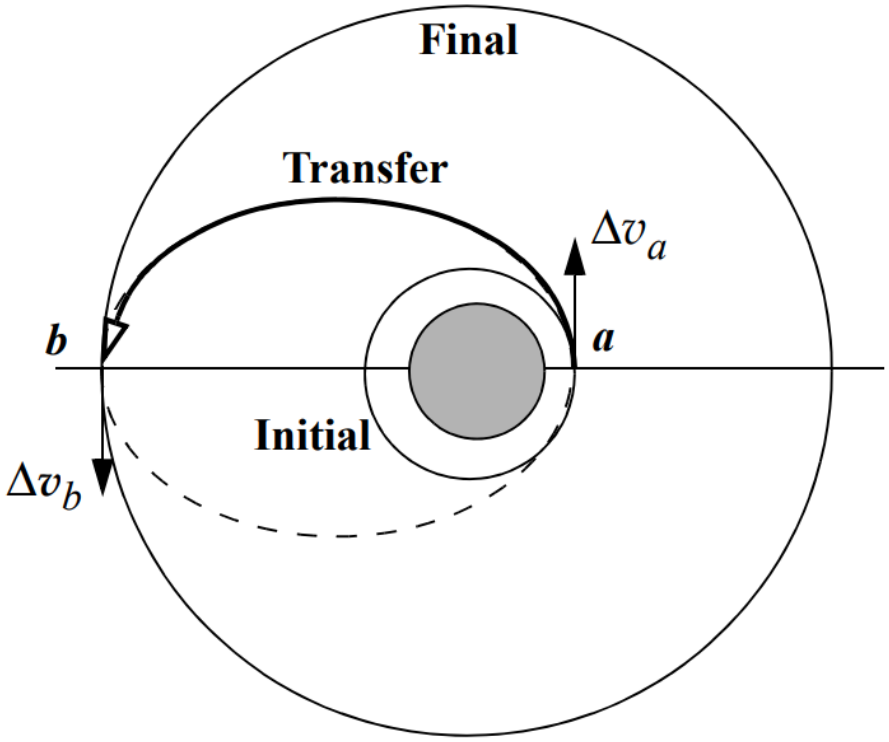

Figure 2.6: Hohmann Transfer [4]

The *Hohmann transfer* is the elliptical transfer orbit between two circular orbit. As evident from the Hohmann transfer (to an outer orbit) shown in the figure, the point of the first burn becomes the perigee of the Hohmann orbit while the point of the second burn represents its apogee.

In general, it is possible to calculate the velocity at a point $\bar{v}$ in the orbit from the equation 2.16:

$$\bar{v} = \sqrt{2\left(\mathscr{E} + \frac{\mu_\Phi}{\bar{r}}\right)} \tag{2.18}$$

Velocity of a circular orbit is constant for the orbit itself:

$$v_{circ} = \sqrt{\left(\frac{\mu_{\oplus}}{r}\right)} \tag{2.19}$$

Because of the perigee and the apogee altitude are known, the semi-major axis of the Hohmann transfer a_H is known too and consequently the time of flight τ:

$$a_H = \frac{r_a + r_p}{2} \tag{2.20}$$

$$T_H = 2\pi\sqrt{\frac{a_H^3}{\mu_{\oplus}}} \qquad \tau = \frac{T_H}{2} \tag{2.21}$$

At this point, Hohmann's Δv can be calculated as the sum of the two Δv at a and b, defined as the magnitude of the difference in velocity between the orbits at the point.

$$\Delta v_a = |v_{H,perigee} - v_{circ,1}| \qquad v_{H,perigee} > v_{circ,1} \tag{2.22a}$$

$$\Delta v_b = |v_{circ,2} - v_{H,apogee}| \qquad v_{H,apogee} < v_{circ,2} \tag{2.22b}$$

$$\Delta v_H = \Delta v_a + \Delta v_b \tag{2.23}$$

Exploiting the SOI concept, it may be useful to apply Hohmann for an initial cost estimate of interplanetary manoeuvres by distinguishing between planetocentric and heliocentric phases.

2.4 Circular Restricted Three-Body Problem

As mentioned in section 2.3, the Three-Body Problem(3BP) introduces a perturbation to the 2BP and is a first step towards the completeness of the n-body physical model. In this thesis, the CR3BP model is considered close enough to the actual scenario to allow certain preliminary considerations to be made. The 3BP studies the motion of a *third body* immersed in the resulting gravitational field of two *primary bodies* (bigger primary and smaller primary). While 2BP presents closed-form analytical solutions (conics), by adding a third body it has not been possible to date to find closed-form solutions for the equations of motion[5][1][4]. The considerations outlined so far are also considered valid under certain assumptions that allow the transition from 3BP to CR3BP:

1. *Circular*, the two primary bodies describe circular orbits relative to the system's centre of mass and this one is a good approzimation for the natural bodies in the Solar System;

2. *Restricted*, the mass of the third body m is considered negligible compared to the other two M_1, M_2.

Consequently, the CR3BP fundamental assumptions are:

- $m << M_2 < M_1$;
- distance between the two primaries, ℓ^*, constant during motion;
- the only gravitational forces are those of the two primaries.

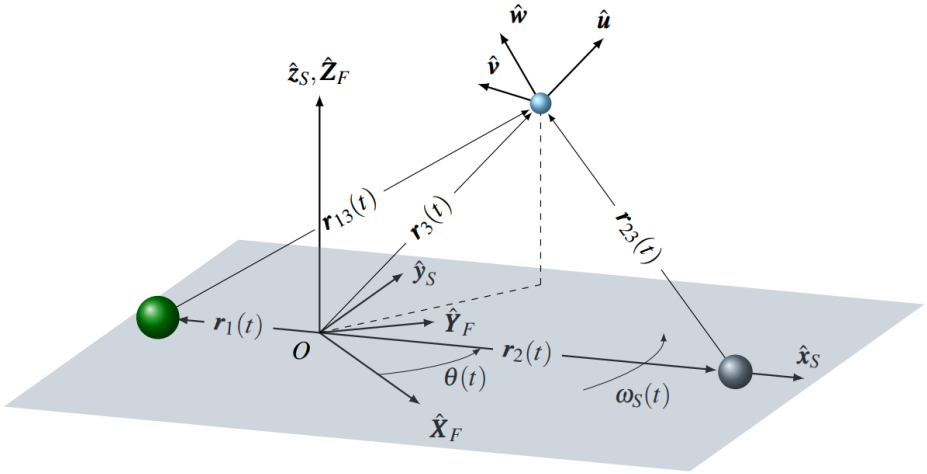

Figure 2.7: Synodic RF [1]

In Fig. 2.7 a generic synodic system is shown when observed from an inertial RS such as $\{\hat{\boldsymbol{X}}_F, \hat{\boldsymbol{Y}}_F, \hat{\boldsymbol{Z}}_F\}$. The two primary bodies rotate around the barycentre of the system (which lies on the conjunction) at a *mutual angular velocity* $\omega(t)$. The dependence on time t is the result of the mutual distance between the two primaries varying over t. In the CR3BP hypothesis, this dependence falls (ℓ^* constant).

The non-inertial, rotating RF centered in the barycenter is also called Synodic RF, $\{\hat{\boldsymbol{x}}_S, \hat{\boldsymbol{y}}_S, \hat{\boldsymbol{z}}_S\}$, and follows the main bodies' path; the $\hat{\boldsymbol{x}}_S$ axis lies on the line joining the two primaries, the $\hat{\boldsymbol{z}}_S$ axis is normal to the plane on which the orbits of the primaries lie and $\hat{\boldsymbol{y}}_S$ completes the right triad.

$$\omega = \sqrt{G \frac{M_1 + M_2}{\ell^{*3}}} \tag{2.24}$$

Thus, the advantage in introducing and using a non-inertial, rotating system is the fall of the dependence of motion on time, as will also be seen in the next

section. The relationship that exists between the inertial RS and the synodic RS can be expressed in matrix form:

$$\begin{Bmatrix} \hat{\boldsymbol{X}}_F \\ \hat{\boldsymbol{Y}}_F \\ \hat{\boldsymbol{Z}}_F \end{Bmatrix} = [\boldsymbol{A}] \begin{Bmatrix} \hat{\boldsymbol{x}}_S \\ \hat{\boldsymbol{y}}_S \\ \hat{\boldsymbol{z}}_S \end{Bmatrix} \tag{2.25}$$

where

$$\boldsymbol{A} = \begin{bmatrix} \cos\omega t & -\sin\omega t & 0 \\ \sin\omega t & \cos\omega t & 0 \\ 0 & 0 & 1 \end{bmatrix} \tag{2.26}$$

is the rotation matrix required to transforme the inertial RS to the synodic one.

In addition, both for historical convention and for the sake of numerical precision and neatness, the investigated quantities within the synodic reference system are nondimensionalized with respect to some characteristic values:

Fundamental Quantity	Unit of Measurement	Equivalence
Mass	kilogram	$m^* = M_1 + M_2$
Lenght	meter	$\ell^* = r_1 + r_2$
Time	second	$T^* = \sqrt{(\ell^{*3})/(Gm^*)}$

Table 2.2: CR3BP nondimensionalization

The characteristic length, denoted as ℓ^*, represents the consistent average separation distance between the two primary bodies within the system. Similarly, the characteristic mass, symbolized as m^*, signifies the combined total mass of these primary bodies. Notably, the characteristic time, denoted as T^*, is not explicitly prescribed but rather emerges as a consequence of enforcing the nondimensional universal gravitational constant to equate unity within the formulation of Kepler's third law. Consequently, it is implicitly derived from this fundamental constraint.

Therefore, the nondimensional quantities for distances, masses, and times, under the CR3BP assumptions, are

$$\begin{cases} \rho_{12} = \frac{r_{12}}{\ell^*} = 1 \\ \mu \triangleq \frac{m_2}{m^*} \\ \tau = \frac{T}{T^*} \end{cases} \tag{2.27}$$

Hence, the nondimensional masses are:

$$\mu \triangleq \frac{\mu_2}{\mu_1 + \mu_2}, \qquad \frac{\mu_1}{\mu_1 + \mu_2} = 1 - \mu \tag{2.28}$$

and similarly, the barycenter position relative to the bigger primary can be readily deduced:

$$\rho_{CG} = \frac{\sum_i \rho_i \mu_i}{\sum_i \mu_i} = \mu \tag{2.29}$$

So

$$\rho_1 = \frac{r_1}{\ell^*} = -\mu\rho_2 = \frac{r_2}{\ell^*} = 1 - \mu \tag{2.30}$$

2.4.1 Equations of motion

Starting from the Newton's Second Law(see equation 2.1), a dimensional compact form can be written:

$$\ddot{\vec{r}} = -\frac{\mu_1}{r_{12}^2}\frac{\dot{\vec{r}}_{13}}{r_{13}} - \frac{\mu_2}{r_{22}^2}\frac{\dot{\vec{r}}_{23}}{r_{23}} \tag{2.31}$$

where

$$\vec{r}_{i3} = \vec{r}_3 - \vec{r}_i, \qquad i = 1{,}2. \tag{2.32}$$

are the radius vector of the spaecraft with respect to the primaries.

Considering the "restricted" assumption of the CR3BP, it is understood that the primary bodies influence the motion of the spacecraft (SC) but remain unaffected by the SC itself. Therefore, for clarity, the subscript "3" denoting the sole SC is dropped. Henceforth, its coordinates are simply represented by $\{x, y, z\}$ values.

By projecting the EOMs into the synodic RF cardinal directions one has

$$\ddot{x} = -\frac{\mu_1}{r_{13}^3}(x - x_1) - \frac{\mu_2}{r_{23}^3}(x - x_2) \tag{2.33a}$$

$$\ddot{y} = -\frac{\mu_1}{r_{13}^3}y - \frac{\mu_2}{r_{23}^3}y \tag{2.33b}$$

$$\ddot{z} = -\frac{\mu_1}{r_{13}^3}z - \frac{\mu_2}{r_{23}^3}z \tag{2.33c}$$

where

$$r_{i3} = \sqrt{(x - x_i)^2 + y^2 + z^2}, \qquad i = 1{,}2. \tag{2.34}$$

It is useful to project the EOMs in the interial RF. To accomplish this, the total differentiation of the position vector $\vec{r}$ in the inertial RF is expressed as the sum of the differentiation of the same vector in the synodic frame and the transport component. Generally, the transport theorem for a generic quantity "$*$" gives the following expression:

$$\frac{^F d*}{dt} = \frac{^R d*}{dt} + {}^{R/F}\vec{\omega} \wedge {}^R* \tag{2.35}$$

Therefore the inertial acceleration can be computed as [6] [1]

$${}^F\ddot{\vec{r}} = {}^R\ddot{\vec{r}} + \dot{\vec{\omega}}_S \wedge {}^R\vec{r} + 2^{R/F}\vec{\omega} \wedge {}^R\dot{\vec{r}} + \vec{\omega}_S \wedge (\vec{\omega}_S \wedge {}^R\vec{r}) \tag{2.36}$$

where the prescripts "F" or "R" indicate the corresponding fixed and synodic RFs, as in Fig 2.7. Equation 2.36 taking into account apparent forces such as centripetal, tangential, and Coriolis acceleration.

Moreover, based on the definition of Keplerian motion, the mean motion is as follows

$$\omega_S = \frac{\mu_1 + \mu_2}{r_{12}^3}. \tag{2.37}$$

However, considering the assumptions of the CR3BP, the angular velocity $\omega_S = 1$, and thus $\dot{\omega}_S = 0$, as there are no rotational or pulsating behaviors present.

Thus, by explicitly expressing the various terms in the equation and applying dimensionalizations, it becomes feasible to derive the complete system of nondimensional Ordinary Differential Equations (ODEs) for the Cartesian components within the CR3BP dynamical model

$$\ddot{\xi} - 2\dot{\eta} - \xi = -\frac{1-\mu}{\rho_{13}^3}(\xi - \mu) - \frac{\mu}{\rho_{23}^3}[\xi - (\ -\mu)] \tag{2.38a}$$

$$\ddot{\eta} + 2\dot{\xi} - \eta = -\frac{1-\mu}{\rho_{13}^3}\eta - \frac{\mu}{\rho_{23}^3}\eta \tag{2.38b}$$

$$\ddot{\zeta} = -\frac{1-\mu}{\rho_{13}^3}\zeta - \frac{\mu}{\rho_{23}^3}\zeta \tag{2.38c}$$

where ρ_1 and ρ_2 are defined as

$$\rho_1 = \sqrt{(\xi + \mu)^2 + \eta^2 + \zeta^2} \tag{2.39}$$

$$\rho_2 = \sqrt{[\xi - (1-\mu)]^2 + \eta^2 + \zeta^2} \tag{2.40}$$

Thus, the equations of motion consist of three nonlinear second-order differential equations, each coupled with the others. Therefore, the only feasible method to solve them is through numerical integration.

2.4.2 Potential function and Jacobian Integral

Among the historical and contemporary challenges presented by the CR3BP in analytically solving its EOMs, which might not even be feasible, as extensively discussed in Szebehely's work [5], a significant glimmer appears from the Jacobian Integral. This quantity represents a pseudo-integral of motion within the CR3BP in the rotating synodic RF, offering valuable insights into stability and accessible regions within the binary system. Its derivation starts for an inertial RF by defining a positive potential function U as:

$$U = \frac{\mu_1}{r_{13}} + \frac{\mu_2}{r_{23}} + \frac{1}{2}\omega_S(x^2 + y^2) \tag{2.41}$$

or, equivalently, in nondimensional form (see Fig 2.8) as

$$\mathscr{U} = \frac{1-\mu}{\rho_{13}} + \frac{\mu}{\rho_{23}} + \frac{1}{2}(\xi^2 + \eta^2). \tag{2.42}$$

This quantity is defined as the pseudopotential within the domain of the CR3BP. It consists of the sum of the centrifugal potential, which accounts for the centrifugal forces present in the problem, and the gravitational potential, which encompasses all gravitational attractive forces acting within the system.

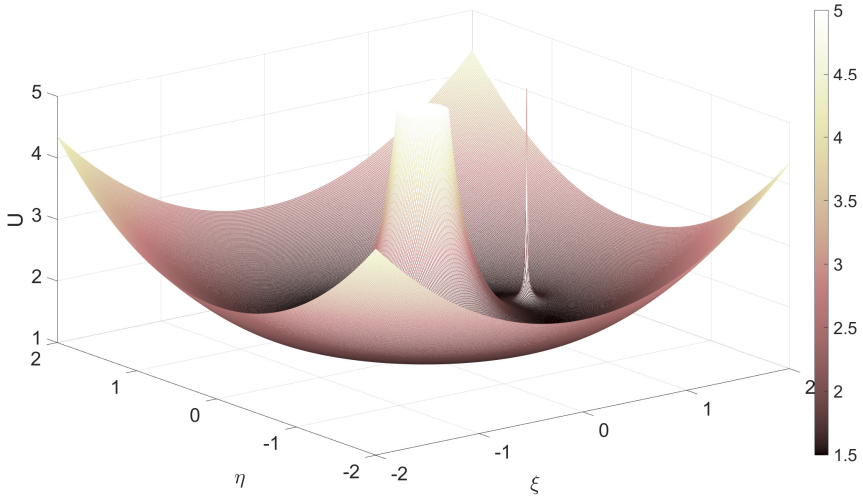

Figure 2.8: Potential function U in the Synodic Earth-Moon(EM) RF

Recalling the physical meaning of the ρ_1 and ρ_2 (eq 2.32), i.e. the position of the spacecraft relative to the two primary bodies, it can be seen that when the two radii tend to zero, the potential function tends to infinity: this means that at the centres of mass there is an infinite potential. Similarly, by moving infinite distances away from the centres of mass of the binary system, the potential function will also tend to infinity. These insights are easily deduced, in addition to Fig 2.8, from equation 2.42.

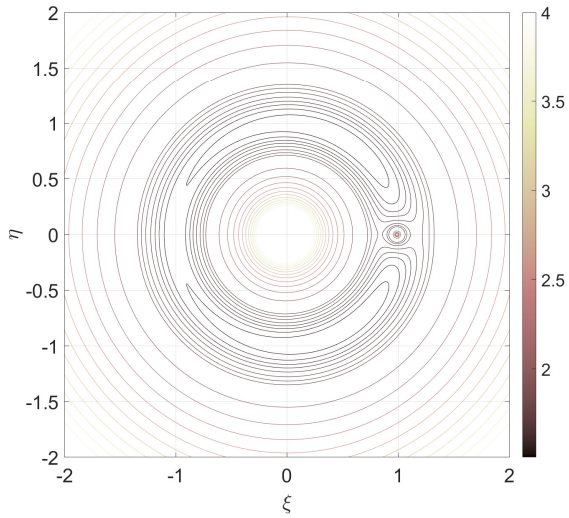

Figure 2.9: Iso-level curves of the potential function U in the Synodic Earth-Moon RF

As is clear from the Figure 2.9, the iso-level curves of the potential function of the Earth-Moon synod system assume a pseudo-circular pattern influenced, as is obvious, by the presence of the massive bodies. Once again, it is evident how, when approaching the centres of mass or moving away at great distances from them, the iso-potential curves tend to assume infinitely large values.

The study of the potential function within this reference system takes on a very important value as it allows us to identify the points of minimum potential, i.e. points of stationarity related to the derivatives of the potential function itself.

Before delving into this topic in the next section, it is necessary to introduce some useful relations, starting with the derivatives of $\mathscr{U}$

$$\frac{\partial \mathscr{U}}{\partial \xi} = \xi - \frac{1-\mu}{\rho_{13}^3}(\xi - \mu) - \frac{\mu}{\rho_{23}^3}[\xi - (1-\mu)] \tag{2.43a}$$

$$\frac{\partial \mathscr{U}}{\partial \eta} = \eta - \frac{1-\mu}{\rho_{13}^3}\eta - \frac{\mu}{\rho_{23}^3}\eta \tag{2.43b}$$

$$\frac{\partial \mathscr{U}}{\partial \zeta} = -\frac{1-\mu}{\rho_{13}^3}\zeta - \frac{\mu}{\rho_{23}^3}\zeta\,. \tag{2.43c}$$

Equations (2.43) can be recombined with equation 2.38 by obtaining as follows

$$\ddot{\xi} - 2\dot{\eta} = \frac{\partial \mathscr{U}}{\partial \xi} \tag{2.44a}$$

$$\ddot{\eta} + 2\dot{\xi} = \frac{\partial \mathscr{U}}{\eta} \tag{2.44b}$$

$$\ddot{\zeta} = \frac{\mathscr{U}}{\zeta}\,. \tag{2.44c}$$

The system of second-order differential equations has a first integral known as the *Jacobi integral*, expressed as

$$2U(x, y, z) - (\dot{x}^2 + \dot{y}^2 + \dot{z}^2) = C, \tag{2.45}$$

where C is the *Jacobi Constant* [7].

Furthermore, by respectively multiplying each of the nondimensional equations in 2.38 by $2\dot{xi}$, $2e\dot{t}a$, $2z\dot{e}ta$, and subsequently summing them, one attains:

$$\dot{\xi}\ddot{\xi} + \dot{\eta}\ddot{\eta} + \dot{\zeta}\ddot{\zeta} = \frac{\partial \mathscr{U}}{\partial \xi}\dot{\xi} + \frac{\partial \mathscr{U}}{\partial \eta}\dot{\eta} + \frac{\partial \mathscr{U}}{\partial \zeta}\dot{\zeta} \tag{2.46}$$

which, once integrated, provides the Jacobian integral equation which defines the spacecraft's field of motion:

$$\dot{\xi}^2 + \dot{\eta}^2 + \dot{\zeta}^2 = v^2 = 2\mathscr{U} - \mathscr{J}_C. \tag{2.47}$$

The dimensional Jacobi Constant J_C can be compared to an inverse energy-like quantity, similar to the specific mechanical energy $\mathscr{E}$ in the vis-viva equation (2.15) within the 2BP. Therefore, the specific mechanical energy $\mathscr{E}$ is the sum of the kinetic $V^2/2$ and the potential $-\mu/r$ specific energies. Consequently, the greater the value of J_C is, the lower the energy of the spacecraft within the synodic Reference Frame is.

When there are no disturbances present, the energy, or Jacobi's constant, remains unchanged throughout a specific orbit. Consequently, with an initial condition defined for the spacecraft's motion in terms of position vector and velocity, the value of the constant J_C remains unvaried.

2.4.3 Equilibrium Points

In light of the nondimensionalization and simplification of the EOMs, an investigation of the system is imperative. The remaining equations, characterized by their lack of intuitivity, present a big challenge in interpreting the motion of the third body(SC) within the gravitational environment. Simulations highlights the

a chaotic behavior, therefore an intrinsic unpredictability of the system without precise initial conditions and parameter settings. Consequently, the main objective moves to the identification of regions manifesting predictable behavior, a fundamental information for aerospace engineers and researchers. This knowledge has profound implications for practical applications in space missions and scientific exploration, providing priceless insights for mission planning and spacecraft design.

In this sense, in 1772 Joseph Louis Lagrange set a milestone by introducing the Libration Points of the Sun-Jupiter binary system to the scientific community: one of the greatest contributions to astrodynamics [3]. From this, equilibrium points are also known as Lagrange Points (LPs). This equilibrium comes from a balance in the centrifugal force and the gravitational attraction of the larger bodies.

Even though an analytical solution for the complete system of ODEs in equation (2.44) has yet to be discovered, valuable theoretical insights can still be gained by manipulating them and following Lagrange's steps [1]. The sistem of equations admit five stationary points, LPs are thus defined by the following conditions

$$\frac{\partial \mathscr{U}}{\partial \xi} = 0 = \xi - \frac{1-\mu}{\rho_{13}^3}(\xi - \mu) - \frac{\mu}{\rho_{23}^3}[\xi - (1-\mu)] \tag{2.48a}$$

$$\frac{\partial \mathscr{U}}{\partial \eta} = 0 = \eta - \frac{1-\mu}{\rho_{13}^3}\eta - \frac{\mu}{\rho_{23}^3}\eta \tag{2.48b}$$

$$\frac{\partial \mathscr{U}}{\partial \zeta} = 0 = -\frac{1-\mu}{\rho_{13}^3}\zeta - \frac{\mu}{\rho_{23}^3}\zeta\,. \tag{2.48c}$$

obtained by setting the vector gradient of the pseudopotential function to zero

$$\nabla \mathscr{U} = 0 \tag{2.49}$$

By settling $\zeta = 0$, the equation (2.48c) is immediatly matched, therefore it's clear that these equilibrium coordinates lie in the $\hat{\xi} - \hat{\eta}$ plane. The second equation, equation (2.48b), is validated under two distinct cases:

1. $\eta = 0$;
2. $\eta \neq 0$ and $\left[1 - \frac{1-\mu}{\rho_{13}^3} - \frac{\mu}{\rho_{23}^3}\right] = 0$;

and this two scenarios correspond to, respectively

1. Collinear Equilibrium Points (L_1, L_2, L_3);
2. Triangular Equilibrium Points (L_4, L_5);

L_1, L_2 and L_3 are referred to as collinear points because they are situated along the ξ-axis. By setting $\eta = 0$ and $\zeta = 0$, the equation of motion corresponding to ξ can be expressed as

$$\xi - \frac{1-\mu}{\rho_{13}^3}(\xi - \mu) - \frac{\mu}{\rho_{23}^3}[\xi - (1-\mu)] = 0 \tag{2.50}$$

To determine the values of ξ at which the equation has real roots, it's necessary to set up the equation along with a second distinct equation. This involves identifying three intervals on the ξ-axis, namely:

$$L_3: \quad \rho_{23} - \rho_{13} = 1, \quad \xi < -\mu \tag{2.51a}$$
$$L_1: \quad \rho_{23} + \rho_{13} = 1, \quad -\mu < \xi < (1-\mu) \tag{2.51b}$$
$$L_2: \quad \rho_{13} - \rho_{23} = 1, \quad \xi > (1-\mu) \tag{2.51c}$$

Assuming that the smaller primary is significantly smaller in size compared to the larger primary, the first two Collinear Lagrangian Points are approximately located at the same distance ρ_{23} from the smaller primary.

$$L_1: \quad \rho_{13} \simeq (1 - \sqrt[3]{\mu/3}), \quad \rho_{23} \simeq \sqrt[3]{\mu/3} \tag{2.52}$$
$$L_2: \quad \rho_{13} \simeq (1 + \sqrt[3]{\mu/3}), \quad \rho_{23} \simeq \sqrt[3]{\mu/3} \tag{2.53}$$

while the L_3 point is on the opposite side of the larger body

$$L_3: \quad \rho_{13} \simeq 1, \quad \rho_{23} \simeq 2 \tag{2.54}$$

Therefore, the coordinates of the Collinear Equilibrium System in the synodic RS are

$$L_1 = \left[1 - \mu - \sqrt[3]{\mu/3}, 0, 0\right] \tag{2.55a}$$
$$L_2 = \left[1 - \mu + \sqrt[3]{\mu/3}, 0, 0\right] \tag{2.55b}$$
$$L_3 = \left[1 - \mu - 2, 0, 0\right] \tag{2.55c}$$

where L_1 is named as *Cislunar Libration Point*, L_2 is named as *Translunar Libration Point* and L_3 is named as *Transearth Libration Point*.

As can be clearly seen in Fig 2.10, by cutting the potential function with the plane for $\eta = 0$, the collinear points correspond to the points of minimum of the potential function.

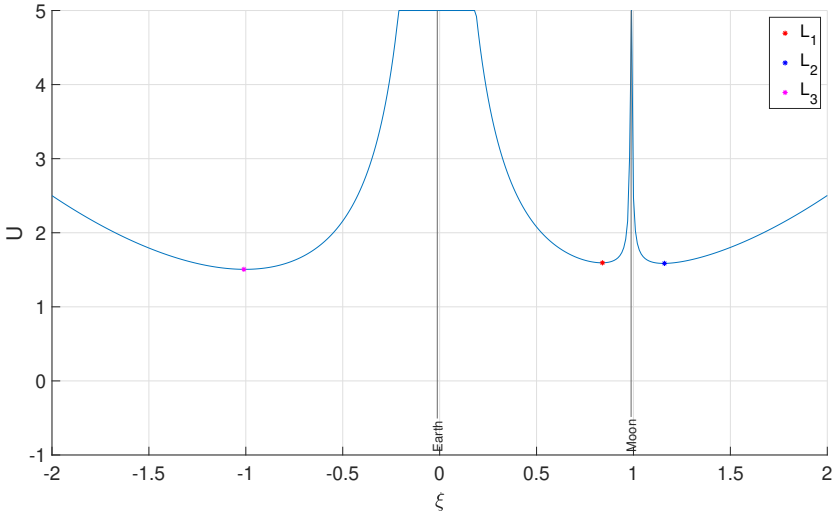

Figure 2.10: Collinear points in EM synodic RS for $\eta = 0$

The coordinates of the Triangular Equilibrium Points are obtained by solving the equations (2.48a) and (2.48b). It emerges that L_4 and L_5 are situated at the vertices of two equilateral triangles with sides of unit length, namely

$$L_4 = \left[\frac{1}{2} - \mu, \frac{\sqrt{3}}{2}, 0\right] \tag{2.56a}$$

$$L_5 = \left[\frac{1}{2} - \mu, -\frac{\sqrt{3}}{2}, 0\right] \tag{2.56b}$$

where the two primaries lie on the other two vertices. This observation is depicted in Fig 2.11, where the dash-dot-dot and dotted circles represent the circular orbits of the primaries relative to the system barycenter when observed from an inertial reference frame.

With reference to the Earth-Moon binary system, it is possible to define the position of Lagrangian points taking certain the following values

- unit of distance: 384400 km;
- unit of velocity: 1.02316 km/s ;
- dimensionless mass ratio μ: 0.01215052.

Consequently, values are reported in Table 2.3

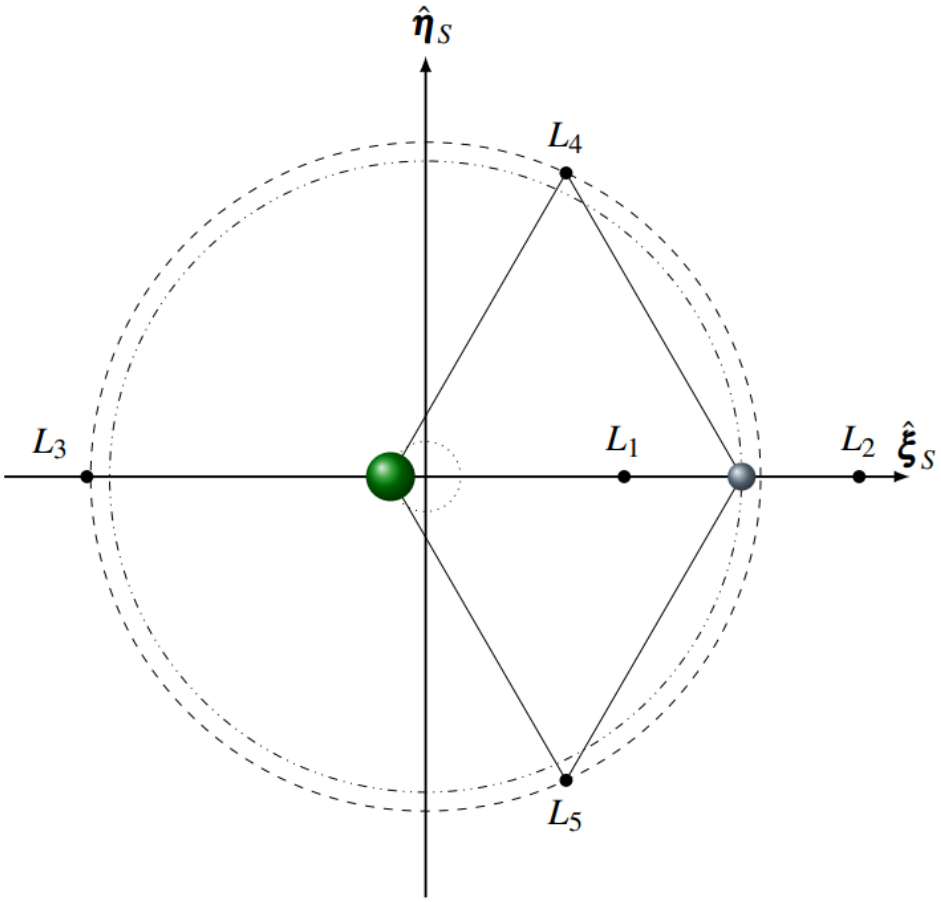

Figure 2.11: Lagrangian points in a generic synodic RS with $\mu = 0.1$ [1]

LP	ξ	η	ζ	$\mathscr{U}$
L_1	0.8500	0	0	1.59422
L_2	1.1700	0	0	1.58614
L_3	-1.0100	0	0	1.50611
L_4	0.4800	0.8700	0	1.49399
L_5	0.4800	-0.8700	0	1.49399

Table 2.3: Earth-Moon binary sistem's LPs location

2.4.4 Zero Velocity Surfaces

An important result obtained by setting the relative velocity in the synodic reference frame to zero, referred to as $v = 0$ within the Jacobi's integral, is the concept of the Zero-Velocity Surface.

$$v^2 = 2\mathscr{U} - \mathscr{J}_C \tag{2.57}$$

In order that motion be possible,

$$v \geq 0 \quad \Longrightarrow \quad v^2 \geq 0 \tag{2.58}$$

it is possible to conclude that during motion there is

$$2\mathscr{U} - \mathscr{J}_C \geq 0 \tag{2.59}$$

indeed, by analysing equation(2.45), it can be seen that the kinetic energy $\dot{x}^2+\dot{y}^2+\dot{z}^2$ is semi-defined positive.

In the specific scenario where the relative velocity in the synodic reference frame is zero, the function

$$2\mathscr{U} - \mathscr{J}_C = 0 \tag{2.60}$$

identifies, based on the value of C and hence the initial conditions, the boundaries of the regions of the physical space where motion is allowed to take place [8]. Such a constraint, given a specific value for the constant, provides the equation of a surface which is the extremal value of all the potential limit apogee-like locations.

So, equation 2.60 establishes the Zero-Velocity Surfaces, which delineate regions where the kinetic energy becomes negative, making motion not possible. These regions where the particle can orbit are referred to as *Hill's regions*. Consequently, Hill's regions are delimited by the Zero-Velocity Surface, or surfaces of zero kinetic energy, which are unattainable by the satellite.

If a SC is positioned near a primary and has an initial velocity close to the orbital velocity, its apogee-like condition (the maximum apogee it could reach if all the orbit's energy is converted into altitude) will be constrained within the gravitational well of the primary itself. The confinement shape near the primaries in the EM Zero-Velocity Surface representation shown in Figure 2.7 resembles a circle.

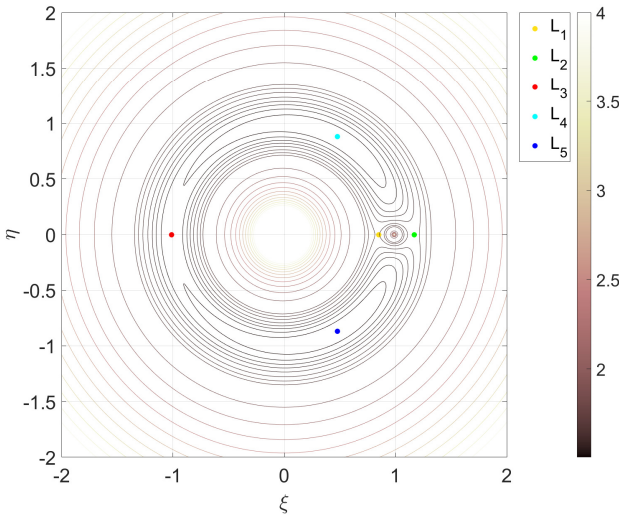

Figure 2.12: EM Zero-Velocity Surfaces at LPs energy

Recalling equation 2.60, the Jacobi constant can be uniquely defined as follows

$$\mathscr{J}_C = 2\mathscr{U} \tag{2.61}$$

Consequently, iso-level curves can be visualised in Fig 2.13, 2.14, 2.15 and 2.16, by cross-cutting the zero-velocity surfaces with the fundamental plane $\xi - \eta$

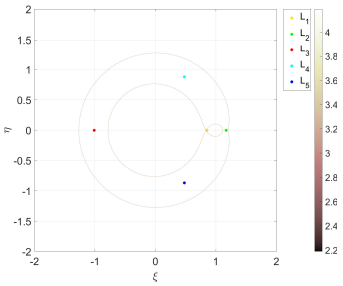

Figure 2.13: EM Zero-Velocity Surface at LP1

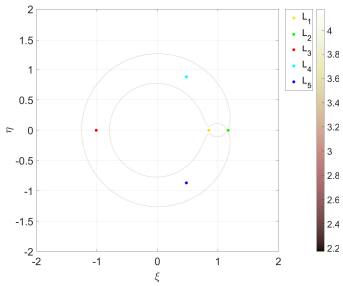

Figure 2.14: EM Zero-Velocity Surface at LP2

The value of Jacobi's constant that allows the points of minimum potential to be reached and to be able to overcome them are shown in the Table 2.4.

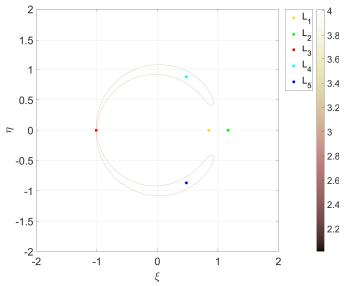

Figure 2.15: EM Zero-Velocity Surface at LP3

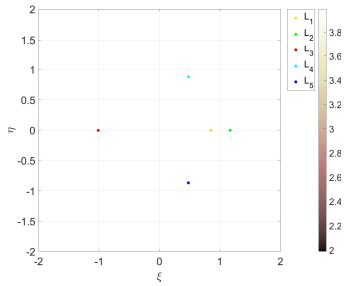

Figure 2.16: EM Zero-Velocity Surface at LP4 and LP5

LP	ξ	η	ζ	$\mathscr{U}$	$\mathscr{J}_C$
L_1	0.8500	0	0	1.59422	3.1885
L_2	1.1700	0	0	1.58614	3.1723
L_3	-1.0100	0	0	1.50611	3.0122
L_4	0.4800	0.8700	0	1.49399	2.9880
L_5	0.4800	-0.8700	0	1.49399	2.9880

Table 2.4: Earth-Moon binary sistem's LPs location, Potential function and Jacobi's constant

The naming convention of Lagrangian Points is determined by the values of the Jacobi's Constant $\mathscr{J}_C$ in decreasing order, which incidentally corresponds to the order in which they become accessible. Specifically, the LP with the highest value of the nondimensional $\mathscr{J}_C$, indicating the first accessible zone at a lower spacecraft energy, is designated as the first LP, followed by the others in sequence. Notably, L_4 and L_5 have the same value of $\mathscr{J}_C$, which is the lowest. If a spacecraft possesses enough energy to reach these Lagrangian Points, then all regions of space within the CR3BP become accessible.

So, technically, a spacecraft capable of traversing the Zero-Velocity Surfaces at L_2 from the inner regions possesses adequate energy to escape the EM binary system by utilizing specific trajectories that leverage the gravitational attractions of the primaries.

2.4.5 Weak Stability Boundary

The Weak Stability Boundary (WSB) serves as the transition region within phase space where the shift from gravitational or *ballistic escape* to *ballistic capture* takes

place. Research conducted on this intricate area of chaotic motion is aimed at exploring its distinct, fuel-saving properties in order to expand the boundaries of low-energy transfers. This region of "fuzzy stability" is typified by highly sensitive motion, and analysis of it has primarily relied on numerical methods [9].

In this section, with reference to Fig 2.17, an effort will be made to give a rigorous definition of the Weak Stability Boundary naming as *P1* and *P2* respectively the bigger primary body and the smaller one and naming as *P3* the SC, following the discussion in [10].

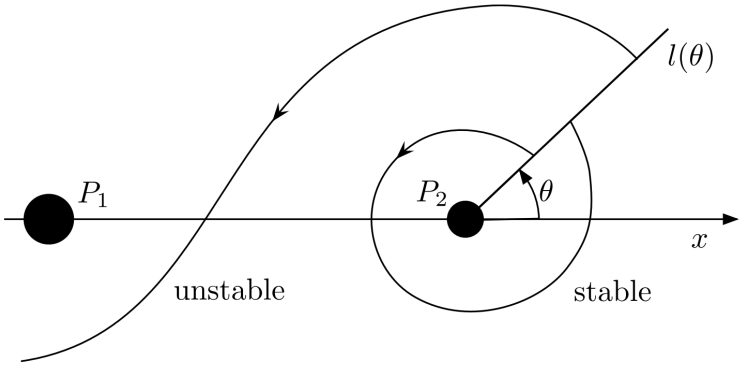

Figure 2.17: The stability criterion used to numerically define $\mathcal{W}$ [11]

We examine trajectories of an infinitesimal particle with the following initial conditions:

(i) The trajectory's initial position lies on a radial segment $\ell(\theta)$ in the configuration space, originating from *P2* and forming an angle of θ with the *P1*-*P2* line, relative to the rotating system. The trajectory initiates at the periapsis of an osculating ellipse around *P2*, with its semi-major axis lying on $\ell(\theta)$ and its eccentricity e held constant along $\ell(\theta)$. The initial velocity of the trajectory is perpendicular to $\ell(\theta)$, offering two distinct choices of initial velocities: one positive (direct motion) and one negative (retrograde motion); below, we will restrict ourselves to the case of positive initial velocity.

(ii) The initial Keplerian energy $\mathscr{E}_2$ relative to *P2* is negative, denoted as $\mathscr{E}_2 < 0$.

(iii) Subsequently, the motion is classified as n-stable if the infinitesimal mass *P3* departs from $\ell(\theta)$, completes n full revolutions around *P2* without completing a full revolution around *P1*, and all intersections of the trajectory with $\ell(\theta)$ along this trajectory are transverse intersections with negative Kepler energy relative to *P2*, i.e., $\mathscr{E}_2 < 0$. Otherwise, the motion is deemed n-unstable.

In condition (i) the distance from *P3* to *P2* is given by $r = a(1-e)$, where a is the semi-major axis of the osculating ellipse. The motion, for fixed values of the parameters θ and e, and for a choice of direction of the initial velocity vector depends only on the initial distance r.

In condition (ii), the initial Kepler energy is given by the equation

$$\mathscr{E}_2 = \frac{(e-1)\mu}{2r}, \tag{2.62}$$

obtained starting from the *visviva equation* (2.15), so the condition $\mathscr{E}_2 < 0$ is automatically satisfied since $e \in [0, 1)$.

In condition (iii), when we refer to $P3$ completing 1 full revolution around $P2$, it is defined as follows:

Let $\theta_2(t)$ represent the angle formed by the position vector of $P3$ relative to $P2$, measured continuously along the trajectory of $P3$. If we consider $P3$ starting from $\ell(\theta)$, then $\theta_2(0) = \theta$. Let τ_1 be the smallest positive time for which $|\theta_2(\tau_1) - \theta_2(0)| = 2\pi$. We assume that the intersection of the trajectory with $\ell(\theta)$ at $t = \tau_1$ is transverse. If such a τ_1 exists, then we say that $P3$ completed 1 full revolution around $P2$ in the time interval $[0, \tau_1]$.

Similarly, let τ_2 be the smallest positive time such that $|\theta_2(\tau_2) - \theta_2(\tau_1)| = 2\pi$. We assume that the intersection of the trajectory with $\ell(\theta)$ at $t = \tau_2$ is transverse. If such a τ_2 exists, it means that $P3$ completed 2 full revolutions around $P2$ in the time interval $[0, \tau_2]$. We can define inductively what it means for $P3$ to complete n full revolutions around $P2$. In this definition, we require that the successive intersections of $P3$'s trajectory with $\ell(\theta)$ are all transverse.

Similarly, we define what it means for $P3$ to complete 1 full revolution around $P1$. If $\theta_1(t)$ represents the angle formed by the position vector of $P3$ relative to $P1$, measured continuously along the trajectory of $P3$, and if for some $\tau > 0$ we have $|\theta_1(t) - \theta_1(0)| < 2\pi$ for all $t \in [0, \tau]$, it means that $P3$ did not complete one full revolution around $P1$ in the interval $[0, \tau]$.

In summary, condition (iii) says that a motion is said to be n-stable if there exist $\tau_n > 0$ such that $P3$ performed n complete turns about $P2$ in the interval $[0, \tau_n]$ and did not complete 1 turn around $P1$ in the same interval.

In the above definition we require that the successive intersections of the trajectory of $P3$ with $\ell(\theta)$ are all transverse. This makes the notion of n-stability under small perturbation, that is, if a trajectory is n-stable then any sufficiently close trajectory will also be n-stable.

We note that the n-stability condition defined as above is an open condition. This is due to the fact that $\mathscr{E}_2 < 0$ is an open condition.

The set of the n-stable points on $\ell(\theta)$ is an open subset of $\ell(\theta)$, hence it is a

countable union of open intervals which we denote

$$\mathcal{W}_n(\theta, e) = \bigcup_{k\geq 1} (r^*_{2k-1}, r^*_{2k}). \tag{2.63}$$

DEFINITION (*WSB*): "*The WSB of index n, denoted by* $\mathcal{W}^*_n$ *, is the locus of all points* $r^*(\theta, e)$ *along the radial segment* $\ell(\theta)$ *where there is a change of stability of the initial trajectory, that is,* $r^*(\theta, e)$ *is one of the endpoints of an interval* (r^*_{2k-1}, r^*_{2k}) *characterized by the fact that for all* $r \in (r^*_{2k-1}, r^*_{2k})$ *the motion is n-stable, and there exist* $r', r'' \notin (r^*_{2k-1}, r^*_{2k})$ *arbitrarily close to* r^*_{2k-1}, r^*_{2k}*, respectively, for which the motion is n-unstable" [10].* Thus

$$\mathcal{W}^*_n = \partial\mathcal{W}_n = \{r^*(\theta, e) \,|\, \theta \in [0,2\pi], e \in [0,1)\}\,. \tag{2.64}$$

2.4.6 Ballistic escape

Indeed, while the concept of the WSB originated in close connection with the concept of *weak capture*, it is also applicable to discussions regarding *ballistic escape* or *ballistic ejection*.

DEFINITION (*Ballistic escape*): P3 is ballistically ejected (or ballistically escapes) from P2 along the solution $\varphi(t)$ at a time t_1 if

$$\mathscr{E}(\varphi(t)) < 0, \quad \text{for} t < t_1 \qquad \text{and} \qquad \mathscr{E}(\varphi(t)) \geq 0, \quad \text{for} t \geq t_1 \tag{2.65}$$

where $H \equiv \mathscr{E}$ is still the SME defined in an Earth-centered RS.

DEFINITION (*Resonant orbit*): An $m : n$ resonant orbit about the Earth, in resonance with the Moon, is an orbit whose period T is related to the Moon's period T_2 by

$$mT = nT_2 \tag{2.66}$$

where m, n are positive integers.

Consequently, equation 2.66 lead to the following condition on semi-major axis a

$$a = \left(\frac{n}{m}\right)^{2/3} (1-\mu)^{1/3}. \tag{2.67}$$

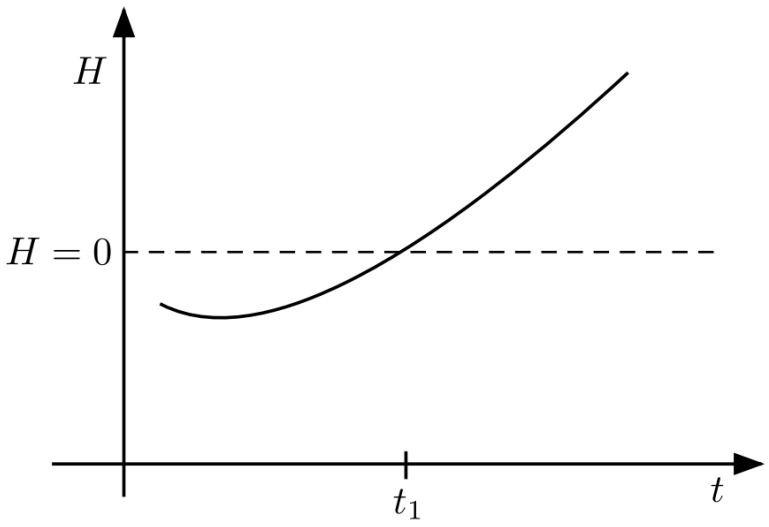

Figure 2.18: Specific mechanical energy in a generic ballistic escape [11]

In Fig 2.18, the energy trend of a ballistic ejection trajectory is shown.

2.5 Ballistic escape in a high-fidelity model

By introducing external perturbations to the CR3BP ('fourth bodies' for example), it is possible to perform a ballistic escape so, other celestial bodies' influence is now taking into account.

Specifically, the behavior of initial orbits in resonance with the Moon in the n-Body Problem (NBP) is investigated. This dynamics is even more intricate than that of the CR3BP since the potential function contains non-autonomous terms representing the gravitational attraction of the other celestial bodies on P3. These terms become particularly significant when P3 moves in the region outside the Moon's orbit. In this outer region, the resonance motion characteristic of the CR3BP is disrupted. Additionally, as noted by Belbruno (1990), particle P3 departs from the Earth–Moon system and enters a heliocentric orbit: this constitutes a ballistic escape and from that point a *patched-conics approximation* takes sense [11].

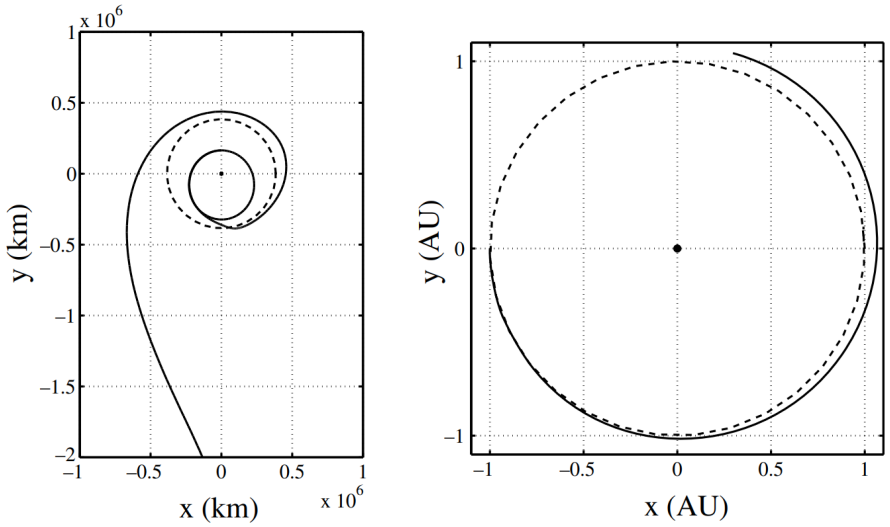

(a) *Earth-centered frame* **(b)** *Sun-centered frame*

Figure 2.19: The shown orbit is perturbated within the four-Body Problem, taking into account Earth, Moon and Sun gravitational influence [11]

Figure 2.19 illustrates a ballistic escape trajectory integrated under the perturbatedy dynamics over a time span equal to 10 lunar periods. P3 completes one orbit around the Earth before experiencing temporary capture by the Moon, leading to its entry into the exterior region (see Fig. 2.19(a)). In this scenario P3 is simply brought away from the Earth–Moon system due to the gravitational pull of the fourth bodies. Subsequently, the particle transitions to a heliocentric orbit and enters a temporary state where its motion is primarily governed by the Sun (as reported in Fig. 2.19(b)). It's noteworthy that this type of escape occurs without the need for any maneuvers; it exploits exclusively the intrinsic dynamics of the perturbated model.

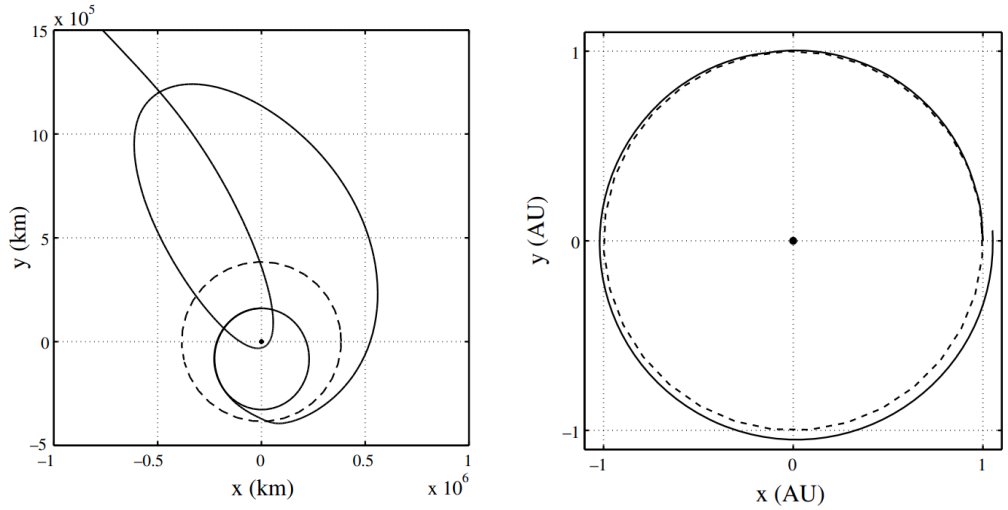

(a) *Earth-centered frame* **(b)** *Sun-centered frame*

Figure 2.20: The shown orbit is perturbated within the four-Body Problem, taking into account Earth, Moon and Sun gravitational influence [11]

Another example is depicted in Fig. 2.20. In this instance, an initial resonant orbit with the Moon is integrated for 13 lunar periods. Following the weak capture at the Moon, P3 is ejected into a highly elliptical orbit around the Earth, with an apogee of approximately 106 km. The perturbation caused by the Sun decreases the perigee of this orbit, leading P3 to perform a flyby of the Earth and execute a ballistic escape. The trajectory's shape—from the weak capture at the Moon to the Earth approach—is remarkably similar to exterior WSB transfers, as described by Belbruno and Miller (1993) [12], Belbruno (1994, 2004) [13], and Belbruno (2007) [14].

Once again, it's important to emphasize that this mechanism leverages the simultaneous gravitational attractions of the Sun, Earth, Moon and other bodies, resulting in an escape with zero cost. This characteristic makes it highly advantageous for spacecraft applications, particularly in the context of low-energy interplanetary transfers aimed at reaching Mars and Venus with minimal propellant mass, as discussed in [15].

2.6 The N-body problem

"The brief introduction to the N-Body Problem in this section takes its cue from the work of R. Bate, Donald D. Mueller and Jerry E. White as reported in the text Fundamentals of astrodynamics".[16]

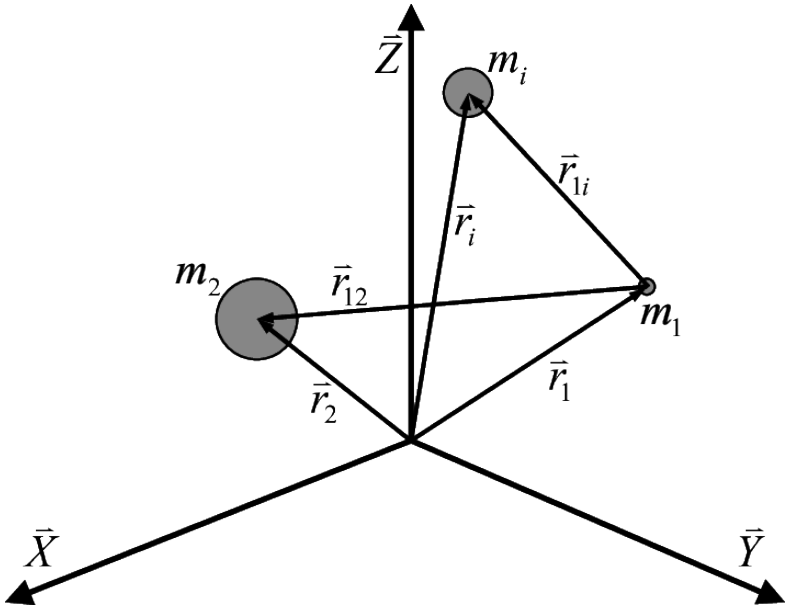

Figure 2.21: The N-Body Problem [17]

At any given moment of its journey, a body is subject to the influence of many gravitational masses and can experience forces such as drag, thrust, solar radiation pressure, etc.

In the following discussion, a system of N-bodies($m_1, m_2, m_3, ..., m_N$) is assumed, of which the one whose motion is to be studied is denoted by subscript i and will be called the i-th body, m_i.

The resultant vector of all gravitational forces and other external forces acting on the i-th body will be used to determine the equation of motion(EOM).

By applying Newton's law of universal gravitation, it is possible to determine the gravitational force of the n-th body on the i-th one.

$$\vec{F}_{gn} = -\frac{Gm_i m_n}{r_{ni}^3}(\vec{r}_{ni}) \tag{2.68}$$

where

$$\vec{r}_{ni} = \vec{r}_i - \vec{r}_n \tag{2.69}$$

The vector sum, $\vec{F}_g$, of all such gravitational forces acting on the i-th body may be written as

$$\vec{F}_g = -\frac{Gm_i m_1}{r_{1i}^3}(\vec{r}_{1i}) - \frac{Gm_i m_2}{r_{2i}^3}(\vec{r}_{2i}) - ... - \frac{Gm_i m_n}{r_{ni}^3}(\vec{r}_{ni}) \tag{2.70}$$

Obviously, equation 2.70 does not contain the term

$$-\frac{Gm_i m_i}{r_{ii}^3}(\vec{r}_{ii}) \tag{2.71}$$

since the i-th body cannot exert a force on itself. Using the summation notation, it's possible to obtain the following simplification

$$\vec{F}_g = -Gm_i \sum_{\substack{j=1 \\ j \neq i}}^{n} \frac{m_j}{r_{ji}^3}(\vec{r}_{ji}) \tag{2.72}$$

The other external forces, as illustrated in Figure **??** is the composition of drag, thrust, solar radiaton pressure, perturbations due to non-spherical shapes, etc. Therefore, the combined force acting on m_i is called $\vec{F}_{TOTAL}$

$$\vec{F}_{TOTAL} = \vec{F}_g + \vec{F}_{OTHER} \tag{2.73}$$

and, assuming the the mass m_i as constant, formulation of the i-th body acceleration can be written

$$\ddot{\vec{r}}_i = \frac{\vec{F}_{TOTAL}}{m_i} \tag{2.74}$$

where $\vec{F}_{TOTAL}$ is the vector sum of all gravitational forces and all other external forces.

To compute a comprehensive and high-fidelity trajectory optimization, it is necessary to utilize a dynamical system that closely calls to mind the real solar system, accounting for all effects and perturbations derived from other celestial bodies and phenomena. In this thesis, the JPL DE440 planetary ephemerides are employed in the NBP dynamical system. This model incorporates gravitational interactions from the main four bodies of the analysis (Sun, Earth, Moon, and the spacecraft itself), while also considering various perturbations, effects and other gravitational influences, which will be thoroughly discussed in the Chapter 3.

Chapter 3

High Fidelity Orbit Propagator

The motion of a satellite operating beyond Geostationary Earth Orbit (GEO) is affected by numerous forces. Among these forces is the central gravitation force exerted by the Earth, while the others are collectively referred to as perturbations. These perturbations can be categorized into:

- gravitational forces;
- non-gravitational forces.

The equation of motion can be modified to include these perturbations by incorporating an additional acceleration term that accounts for their influence. This modification adjusts the equation accordingly to accurately represent the satellite's motion under the combined effects of central gravity and various perturbations.

Recalling the equation of motion (EOM) for the two-body problem (2BP), already seen in 2.6

$$\ddot{\vec{r}} = -\frac{\mu_{\oplus}}{r^2}\frac{\vec{r}}{r}, \tag{3.1}$$

the writing of the EOM in the high-fidelity (HF) model becomes clearer, within which the compact acceleration term γ_p appears [16], grouping the different perturbations as mentioned above

$$\ddot{\vec{r}} = -\frac{\mu_{\oplus}}{r^2}\frac{\vec{r}}{r} + \gamma_p. \tag{3.2}$$

In the remainder of the chapter, the perturbative term γ_p will be exploded in its various components and analysed more deeply.

With reference to a high precision orbit propagator (HPOP) dedicated to low earth orbit (LEO) [18], a HF model was implemented for the study within this thesis.

3.1 Perturbing accelerations

The dynamical model gathers different perturbing effects on the bodies' motion: the acceleration induced by the gravitational forces of the Moon $\ddot{\vec{r}}_M$, the Sun $\ddot{\vec{r}}_S$ and the other solar system's planets $\ddot{\vec{r}}_P$, the acceleration resulting from the Earth's non-sphericity and inhomogeneous mass distribution within itself $\ddot{\vec{r}}_E$, the perturbation originating from direct $\ddot{\vec{r}}_{SP}$ and Earth-reflected solar radiation pressure $\ddot{\vec{r}}_A$.

Consequently, the vectorial expression for the cumulative combined perturbing acceleration from the system can be expressed as follows

$$\gamma_p = \ddot{\vec{r}}_M + \ddot{\vec{r}}_S + \ddot{\vec{r}}_P + \ddot{\vec{r}}_E + \ddot{\vec{r}}_{SP} + \ddot{\vec{r}}_A \tag{3.3}$$

Further on each perturbation is discussed singularly in the following Sections.

3.1.1 Lunisolar effect

The DE440 JPL ephemerides [19] serve as the source for retrieving the positions of the Moon (subscript ℓ) and the Sun (subscript s). Here, subscript b denotes a generic celestial body, and its position vector $\vec{r}_b$ is represented in rectangular coordinates x_b, y_b, z_b with respect to the Earth in the ICRF, denoted as $\vec{r}_b = x_b\boldsymbol{I} + y_b\boldsymbol{J} + z_b\boldsymbol{K}$. In this analysis, the small differences between the ICRF and the EME2000 reference frames are neglected, and the latter is utilized. The gravitational perturbation induced by the body, characterized by a gravitational parameter μ_b and a position vector $\vec{r}_b$ relative to the Earth, is computed as the difference between the gravitational accelerations acting on the spacecraft ($\vec{a}_{bg}$) and the Earth ($\vec{a}_{bE}$). One has

$$\vec{a}_{bg} = -\left(\frac{\mu_b}{R_b^3}\right)\vec{R}_b - \left(\frac{\mu_b}{r_b^3}\right)\vec{r}_b \tag{3.4}$$

where $\vec{R}_b = \vec{r} - \vec{r}_b$ is the spacecraft relative position vector (and $-\vec{r}_b$ is Earth's relative position) with respect to the perturbing body, as extensively explained in [20]. A schematic representation is provided in Figure 3.1 below.

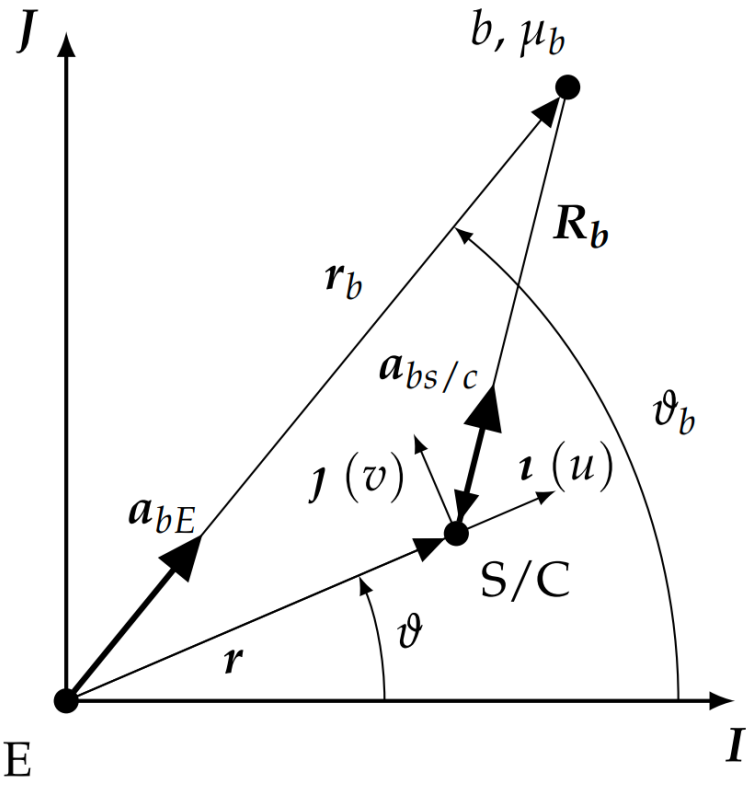

Figure 3.1: Schematic representation of third body gravitational perturbation in EME2000 RF [20]

The acceleration is projected onto the topocentric frame at the epoch to facilitate the extraction of perturbing components. In cases where the perturbing body is significantly distant compared to the Earth-spacecraft distance (i.e., when $\vec{r}_b \gg \vec{r}$, such as what happens with the Sun), and coplanarity is assumed, a simplified expression for the tangential and radial components of the perturbation can be derived (see [20] [21] [1]).

$$(\vec{a}_{ss\backslash c} - \vec{a}_{sE}) \cdot \hat{u}_j = \frac{3}{2}\frac{\mu_s}{r_s^3} \sin\left[2(\vartheta_s - \vartheta)\right] \tag{3.5a}$$

$$(\vec{a}_{ss\backslash c} - \vec{a}_{sE}) \cdot \hat{u}_i = \frac{3}{2}\frac{\mu_s}{r_s^3} \{1 + \cos\left[2(\vartheta_s - \vartheta)\right]\} \tag{3.5b}$$

where $\hat{u}_j$ and $\hat{u}_i$ are, respectively, the tangential and radial unit vectors.

The spacecraft velocity primarily consists of components along the tangential and radial directions. Therefore, these terms can be utilized to estimate the positive or negative effects of solar perturbation during the escape. Equations (3.5a) and

(3.5b) illustrate that it is possible to considering the dependence of the perturbation effect on the Sun-spacecraft position through the following two proportionality terms

$$\varsigma_v = \sin 2\Delta\vartheta \tag{3.6a}$$
$$\varsigma_u = 1 + \cos 2\Delta\vartheta \tag{3.6b}$$

where $\Delta\vartheta$ is the angular difference between the Sun and the spacecraft. Energy increases due to the acceleration component along the spacecraft direction. A large positive ς_v tends to be more advantageous during the initial phase (tangential velocity), whereas a large ς_u should be preferred in the final phases, when the velocity tends towards the radial direction. A large ς_v occurs when the Sun is in the first ($0° < \Delta\vartheta < 90°$) or third ($-180° < \Delta\vartheta < -90°$) quadrant in the spacecraft rotating frame, whereas other $\Delta\vartheta$ combinations may have null or negative influence on the spacecraft energy if the spacecraft is continuously moving outward. On the other hand, the radial acceleration cannot produce a negative effect (unless the spacecraft is moving towards the Earth) and has a maximum positive influence when the Sun is between the fourth and first quadrants ($-45° < \Delta\vartheta < 45°$) or between the second and the third quadrants ($\Delta\vartheta > 135°$ and $\Delta\vartheta < -135°$).

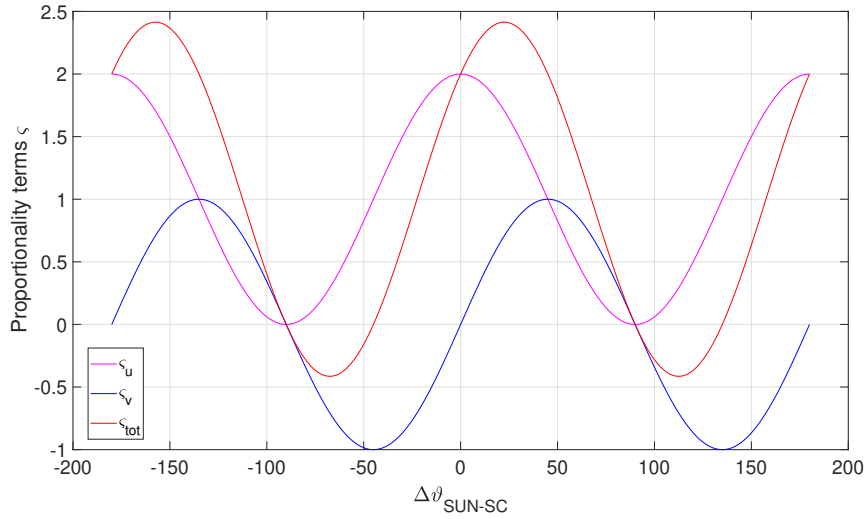

Figure 3.2: Tangential and radial components of the lunisolar perturbative effect ς_v and ς_u

In general, as shown in Figure 3.2,the combined effect of the two solar perturbation components may produce an overall positive effect on the spacecraft energy

when the Sun is either close to $-157.5°$ or $22.5°$ with respect to the Earth–spacecraft direction.

The gravitational influence of the other celestial bodies in the solar system is evaluated in a similar way to what is explained in this section. For the purposes of a study of ballistic escape manoeuvres from the EM system, the motion of the satellite will always occur in the proximity of the Earth and Moon, and the effect of the other planets will be secondary to that of the Sun, which can be referred to as the *primary fourth body*.

3.1.2 Earth asphericity

The perturbation is computed via the GRACE Gravity Model GGM03C [22].

The gravity field of the Earth exhibits variability both spatially and temporally, constituting an integral constraint on the mean and time-variable mass distribution within the Earth. To estimate global models for the mean and time-variable Earth gravity field, data from the Gravity Recovery and Climate Experiment (GRACE) mission has been utilized. Approximately every 30 days, science data from GRACE have been employed to derive these models. This data includes measurements of inter-satellite range changes, as well as accelerometer, GPS, and attitude measurements obtained from each satellite involved in the mission.

As deeply explained in [23], GRACE mission utilize a method of Satellite-to-Satellite Tracking exploiting a *low-low concept*, based on two satellites following each other along the same orbit, a few hundred kilometers apart. The spacecraft in the low orbit are the sensors in Earth's gravity field. One-way and two-way microwave intersatellite tracking systems can be used to measure the relative velocities. The irregular variations of this velocity contain gravitational information. The lower the satellite's orbit the more pronounced and detailed this information becomes.

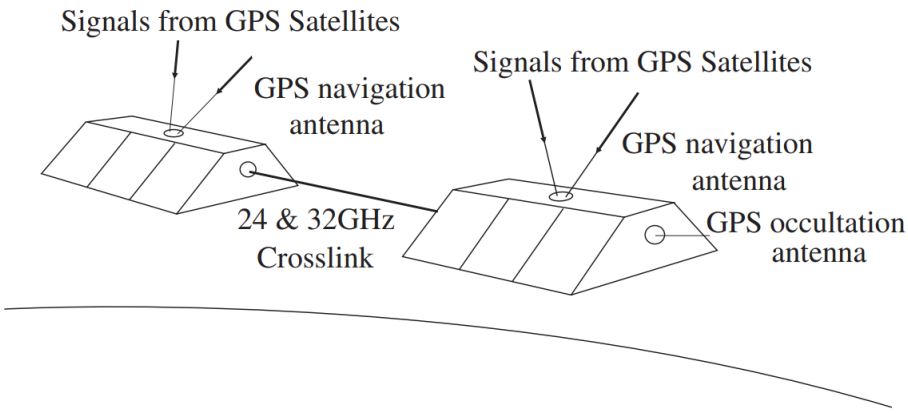

Figure 3.3: GRACE mission [23]

Two identical satellites were launched on March 17, 2002, into a near-polar orbit of about 500 km altitude with an inclination of 89°. In the nominal configuration the satellites fly in-echelon, 220 km apart, within ±50 km.

In essence, the twin GRACE satellites can be considered as one instrument in which:

- variations in the gravity field cause variations in the range between the two satellites; areas of stronger gravity will affect the lead satellite first and accelerate it away from the following satellite;
- range variations are measured by a high-accuracy microwave link; the relationship to the global reference frame is given by GPS;
- the observed range variations are corrected for non-gravitational effects by a precise accelerometer.

The observations will produce monthly global gravity maps with a spatial resolution of about 300 km on the ground, and a precision superior by a factor of up to 100 over existing models.

GRACE, a joint project between NASA and the German Space Agency (DLR), measured changes in the local pull of gravity as water shifted around Earth due to varying seasons, weather patterns, and climate processes.

GRACE introduced several innovations in Earth observation. It monitored the loss of ice mass from Earth's ice sheets, leading to an improved understanding of the processes contributing to sea level rise and ocean circulation. Additionally, GRACE provided insights into areas where global groundwater resources may be diminishing or expanding and identified regions where dry soils are getting worse

drought conditions. Moreover, GRACE monitored changes in the solid Earth, putting a focus on geophysical phenomena.

The GRACE science mission concluded in October 2017, having made significant contributions to our understanding of Earth's dynamic systems [24].

The perturbing acceleration resulting from Earth's non-sphericity is determined by the gradient of the function $\Phi = \mathcal{V} + \mu_{\Phi}/r$, where $\mathcal{V}$ is The dimensional potential due to the Earth asphericity of an object positioned at a geocentric distance r, with a certain longitude θ and a certain latitude φ . Its components in the topocentric frame are therefore evaluated as:

$$(a_J)_u = \frac{\partial \Phi}{\partial r} \tag{3.7a}$$

$$(a_J)_v = \frac{\partial \Phi}{\partial \theta} \frac{1}{r \cos \varphi} \tag{3.7b}$$

$$(a_J)_w = \frac{\partial \Phi}{\partial \varphi} \frac{1}{r} \tag{3.7c}$$

Harmonics of order 8 and degree 8 are implemented along the associated legendre functions and spherical harmonic coefficients [1].

Deriving with respect to r and θ is straightforward; however, deriving with respect to φ necessitates the computation of derivatives of the associated Legendre functions. These derivatives are obtained recursively, leveraging the properties of Legendre polynomials[1].

3.1.3 Solar Radiation Pressure

Since the early days of the first radiometers, like Crookes' radiometer, experiments on light's wave-particle duality have demonstrated that light can exert a net momentum when it strikes a surface [1]. Photons emitted from the Sun carry momentum and travel at the speed of light c. While some dynamical models consider spacecraft to be massless, they do possess specific physical properties. The spacecraft utilized in the analysis exhibits characteristics as outlined in Table 3.1.

Quantity		Value	
Mass	m_0	500	kg
Cross-section Surface	S	4	m^2
Surface reflectivity	C_r	1	

Table 3.1: SC characteristic values

The photon pressure p at a generic distance r from the Sun, considered a point source of light emitting spherical wavefronts, is given by:

$$p = \frac{\mathcal{I}}{4\pi r^2} c, \tag{3.8}$$

where $\mathcal{I} = 1367\mathrm{W/m}^2$is the radiated power, also referred to as the solar constant or solar irradiance, which scales with the inverse squared distance from the Sun in Astronomical Units. The photon pressure at $r^* = 1\mathrm{AU}$ equals $p^* = 4.55682 \times 10^{-6}\mathrm{N/m}^2$. By defining the quantity

$$\Gamma = (1 + C_r)pS \tag{3.9}$$

the acceleration on a spherical body of mass m and surface S at a distance from the Sun $r_{ss\backslash c}$ is

$$(a_{srp})_u = -\frac{\Gamma}{m r_{ss\backslash c}^3}[(r_{sE})_u - r] \tag{3.10a}$$

$$(a_{srp})_v = -\frac{\Gamma}{m r_{ss\backslash c}^3}(r_{sE})_v \tag{3.10b}$$

$$(a_{srp})_w = -\frac{\Gamma}{m r_{ss\backslash c}^3}(r_{sE})_w \tag{3.10c}$$

Once more, the Solar Radiation Pressure (SRP) is a function of r, θ and φ, but it also depends on the mass of the spacecraft itself, m, which could vary along the trajectory if thrusting maneuvers are performed; within this study, since it is intended to carry out ballistic type manoeuvres under the assumption of chemical and therefore impulsive propulsion, the mass of propellant emitted as a result of the required burn only (provided in the initial phases of the mission) will be neglected and m considered as constant. The formulation presented here is a partially simplified one in which the spacecraft's surface is assumed to be consistently facing the Sun at all times, thereby neglecting changes in perspective and effective area [1] [25].

3.2 Integraton method

One approach to ensure accuracy in solving an Initial Value Problem (IVP) is to solve the problem twice using step sizes h and $h/2$, and then compare the solutions at mesh points corresponding to the larger step size. However, this method requires a significant amount of computation for the smaller step size and may need to be repeated if the agreement is not satisfactory.

The Fehlberg method provides a solution to this problem by incorporating a procedure to determine if the proper step size h is being used. At each step, two

different approximations for the solution are computed and compared. If the two approximations are in close agreement, the current step size is deemed appropriate, and the solution is accepted. However, if the two approximations do not agree to a specified accuracy, the step size is reduced. Conversely, if the agreement between the approximations exceeds the required accuracy, the step size is increased. [26].

3.2.1 Initial Value Problems

Obtaining a particular solution of an $n-th$ order differential equation can be achieved by assigning specific values to the n constants in the general solution. However, in typical applications of differential equations, you are often tasked with finding a solution of a given equation that satisfies certain preassigned conditions. These conditions, known as initial conditions, are crucial in determining the specific solution that best describes the physical system or phenomenon under consideration. Solving the differential equation subject to these prescribed conditions allows us to obtain a solution that is not only mathematically correct but also physically meaningful in the context of the problem at hand.

An $n-th$ order IVP consists of an $n-th$ order differential equation

$$F(x, y, y', y'', ..., y^{(n)}) = 0 \tag{3.11}$$

together with n (initial) conditions of the form

$$y(c) = k_0, \quad y'(c) = k_1, \quad y''(c) = k_2, \quad \ldots, \quad y^{(n-1)}(c) = k_{n-1}. \tag{3.12}$$

where c and k_0, k_1, ..., k_{n-1} are given numbers.

3.2.2 Runge Kutta Fehlberg method

In 1969, Erwin Fehlberg introduced a variation of the Runge-Kutta method [27], which utilizes an estimate of local error to determine an appropriate step size [Ref 6]. For a given value of y_n, Fehlberg's method calculates two estimates of y_{n+1} using fourth- and fifth-order Runge-Kutta formulas. By comparing these two values of y_{n+1}, an estimate of the local error is obtained. Subsequently, the step size is adjusted based on the magnitude of this local error [28]. This adaptive step-size control mechanism ensures that the numerical integration scheme maintains accuracy while minimizing computational effort.

Fehlberg first uses

$$y_{n+1} = y_n + \sum_{i=1}^{6} c_i k_i \tag{3.13}$$

where the k_i satisfy

$$k_i = h_n f(x_n + \alpha_i h_n,\, y_n + \sum_{j=1}^{i-1} \beta_{ij} k_i) \qquad i = 1, \ldots, 6. \tag{3.14}$$

This method requires six function evaluations per step. The coefficients c_i are determined by expanding y_{n+1} in powers of h_n so that it aligns as closely as possible with the Taylor series solution. Fehlberg discovered that the two expansions match until the h_n^6 term, thus rendering the method fifth-order accurate. This deviates from the behavior of nth-order Runge-Kutta methods, where $n = 1,2,3,4$, which typically yield errors of $(n + 1)$st order. Obtaining one additional order of accuracy usually requires two more function evaluations. However, Fehlberg's method leverages the sixth function evaluation by determining a second value y^*_{n+1} using the following expression

$$y^*_{n+1} = y_n + \sum_{i=1}^{6} c^*_i k_i \tag{3.15}$$

The local error is then estimated by

$$D_n = \sum_{i=1}^{6} (c_i - c^*_i) k_i \tag{3.16}$$

which is used for stepwise control.

Increasing the accuracy of the integration method, Fehlberg also introduced a variation to the Runge-Kutta method with seventh-order evaluation [29]. Naming it as Runge-Kutta-Fehlberg (RKF) 7(8) and following the rationale explained above within this Section, a semplifying guide-line is reported below:

1. *Coefficient Calculation*: The RKF 7(8) method computes solutions in two main steps. The step at order 7 computes an estimate of the solution, while the step at order 8 computes a more accurate estimate;

2. *Step at Order 7*: In this step, coefficients are calculated to estimate the solution using a 7th order Runge-Kutta method. This is the initial step that produces an approximate solution;

3. *Step at Order 8*: Subsequently, using the same starting point and coefficients, a second step is performed with an 8th order Runge-Kutta method. This yields a more accurate estimate of the solution;

4. *Error Calculation*: After obtaining estimates from the solutions at order 7 and order 8, an estimated error is calculated by comparing the two estimates. If the error is acceptable relative to a certain specified tolerance criterion, the order 8 solution is used. Otherwise, an additional step is performed to reduce the error;

5. *Temporal Step Update*: Based on the calculated error, the temporal step can be adapted to ensure greater accuracy in the solution. This adjustment of the

temporal step helps maintain a desired level of accuracy without having to perform too many function evaluations.

Even if computational cost is heavier than lower orders Runge-Kutta embedded method, high algebraic order RKF methods are commonly used when stringent tolerances are demanded [30].

Fehlberg propose a numerical comparison between RKF 7(8) method and a standard method such as ones based on SHANKS's formulas. Studying a generical problem analised in *"Classical Fifth-, Sixth-, Seventh-, and Eighth-Order Runge-Kutta Formulas with Stepsize Control"* [29], which relative coefficients are shown in Figure 3.5

the resulting comparison are reported in Figure 3.4

Method	Number of Substitutions per Step	Results for x = 5 and Tolerance 10^{-18}				
		Number of Steps	Total Number of Evaluations	Running Time on IBM-7094 (min)	Accumulated Errors in y and z	
					Δy	Δz
SHANKS	17	1423	24 191	2,49	$-0,1332 \cdot 10^{-13}$	$-0,7377 \cdot 10^{-13}$
RK7(8)	13	818	10 634	1,12	$-0,2509 \cdot 10^{-13}$	$-0,5135 \cdot 10^{-13}$

Figure 3.4: Comparison of seventh-order methods for given x and Tolerance [29]

The table demonstrates that in this example, the computational running time for RK7(8) formula is only approximately 45% of the running time required for SHANKS's 7th-order one. The relatively large number of integration steps (1423) necessary for SHANKS's formula reflects the unfavorable magnitude of its error coefficients.

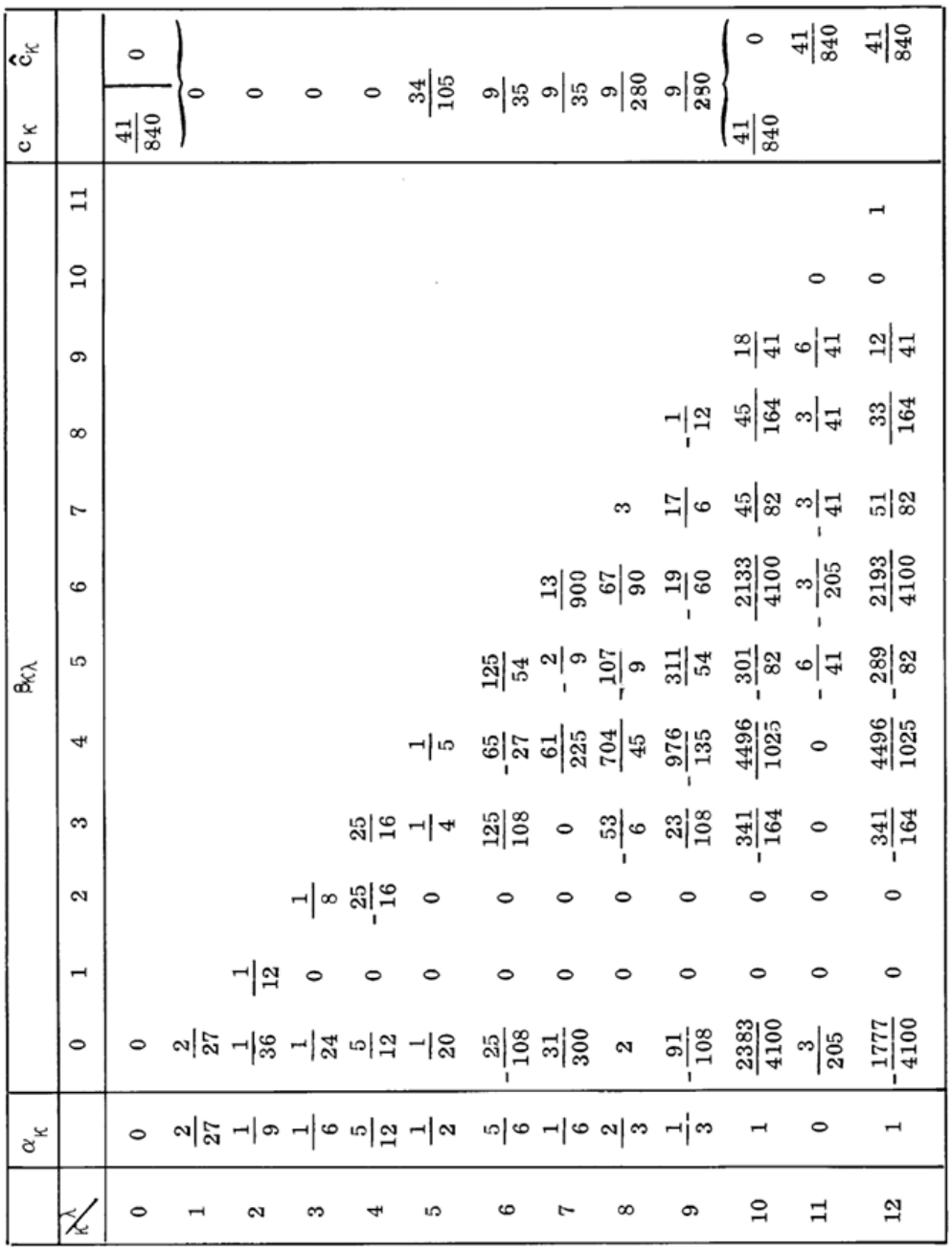

κ \ λ	α_κ	0	1	2	3	4	5	6	7	8	9	10	11	c_κ	$\hat{c}_\kappa$
0	0	0												$\frac{41}{840}$	0
1	$\frac{2}{27}$	$\frac{2}{27}$												0	
2	$\frac{1}{9}$	$\frac{1}{36}$	$\frac{1}{12}$											0	
3	$\frac{1}{6}$	$\frac{1}{24}$	0	$\frac{1}{8}$										0	
4	$\frac{5}{12}$	$\frac{5}{12}$	0	$-\frac{25}{16}$	$\frac{25}{16}$									0	
5	$\frac{1}{2}$	$\frac{1}{20}$	0	0	$\frac{1}{4}$	$\frac{1}{5}$								$\frac{34}{105}$	
6	$\frac{5}{6}$	$-\frac{25}{108}$	0	0	$\frac{125}{108}$	$-\frac{65}{27}$	$\frac{125}{54}$							$\frac{9}{35}$	
7	$\frac{1}{6}$	$\frac{31}{300}$	0	0	0	$\frac{61}{225}$	$-\frac{2}{9}$	$\frac{13}{900}$						$\frac{9}{35}$	
8	$\frac{2}{3}$	2	0	0	$-\frac{53}{6}$	$\frac{704}{45}$	$-\frac{107}{9}$	$\frac{67}{90}$	3					$\frac{9}{280}$	
9	$\frac{1}{3}$	$-\frac{91}{108}$	0	0	$\frac{23}{108}$	$-\frac{976}{135}$	$\frac{311}{54}$	$-\frac{19}{60}$	$\frac{17}{6}$	$-\frac{1}{12}$				$\frac{9}{280}$	
10	1	$\frac{2383}{4100}$	0	0	$-\frac{341}{164}$	$\frac{4496}{1025}$	$-\frac{301}{82}$	$\frac{2133}{4100}$	$\frac{45}{82}$	$\frac{45}{164}$	$\frac{18}{41}$			$\frac{41}{840}$	0
11	0	$\frac{3}{205}$	0	0	0	0	$-\frac{6}{41}$	$-\frac{3}{205}$	$-\frac{3}{41}$	$\frac{3}{41}$	$\frac{6}{41}$	0			$\frac{41}{840}$
12	1	$-\frac{1777}{4100}$	0	0	$-\frac{341}{164}$	$\frac{4496}{1025}$	$-\frac{289}{82}$	$\frac{2193}{4100}$	$\frac{51}{82}$	$\frac{33}{164}$	$\frac{12}{41}$	0	1		$\frac{41}{840}$

Figure 3.5: Runge-Kutta coefficients

3.3 NASA's NAIF SPICE Toolkit

The Spacecraft Planet Instrument Camera-matrix Events (SPICE) project [31] was initiated at National Aeronautics and Space Administration (NASA) in the 1980s in response to the increasing complexity of space missions and the need to standardize the way data regarding the position and orientation of celestial bodies were represented and utilized in calculations. The toolkit was developed at NASA's Jet Propulsion Laboratory (JPL), within the Navigation and Ancillary Information Facility (NAIF) with the aim of providing scientists and engineers with a common tool to work with spatial data from a wide range of missions.

As a direct descendant of its predecessor, the Supplemental Experiment Data Record (SEDR) program, today the SPICE toolkit is utilized at various levels and by numerous space agencies, as shown in Figure 3.6.

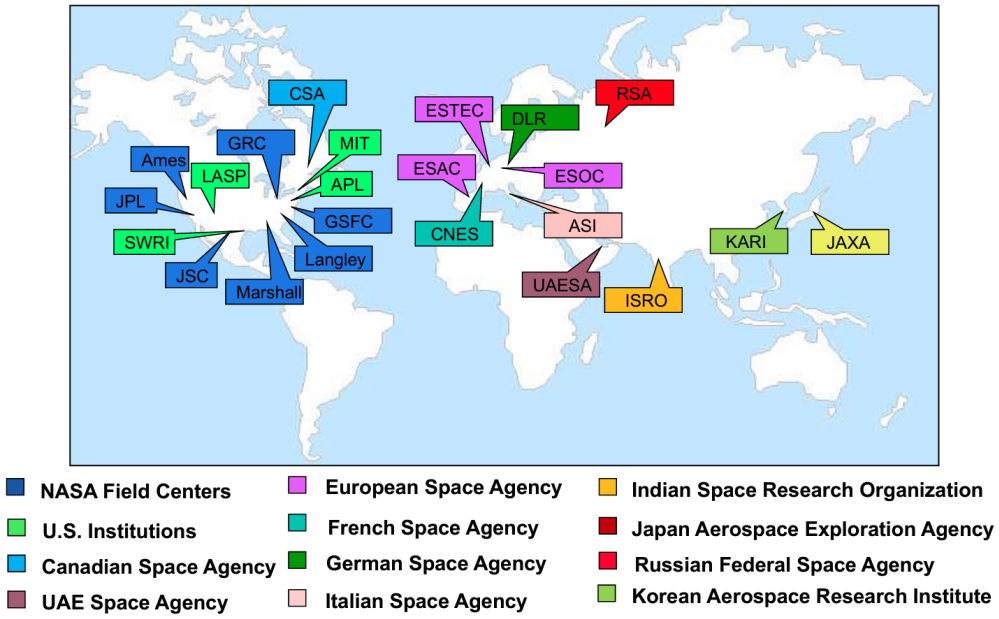

Figure 3.6: Space Agencies using SPICE in 2023

3.3.1 Generic SPICE capability

Utilizing NAIF's SPICE Toolkit within a space analysis (generically reported in Fig. 3.7) permits to compute many kinds of observation geometry parameters at selected times:

- Positions and velocities of planets, satellites, comets, asteroids and spacecraft;
- Size, shape and orientation of planets, satellites, comets and asteroids;

- Orientation of a spacecraft and its various moving structures;
- Instrument field-of-view location on a planet's surface or atmosphere.

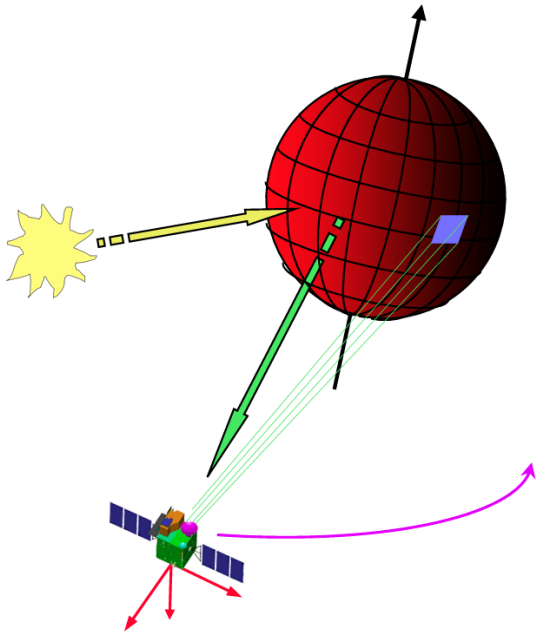

Figure 3.7: Scheme of a generic space scenario

Introducing a SPICE data overview allows us to identify various types of data kernels essential for conducting analyses within the SPICE environment. Table 3.2 provide a brief summary of these data files typologies.

3.3.2 SPICE Toolkit application at the analysis

For what concerns the work carried out within this thesis, some useful kernels have been recalled:

- *Spacecraft and Planet Kernel*, SPK - de440s.bsp;
- *Leapseconds Kernel*, LSK - naif0012.tls.

Now, let's introduce a brief description of the most useful tools for this dissertation from the SPICE library that are employed to compute the necessary ephemeris of celestial bodies:

Logical Components	Kernels	Contents
Planet and Spacecraft	SPK	Space Vehicle or Target Body Trajectory (Ephemris)
Planet	PCK	Target Body Size, Shape and Orientation
Instrument	IK	Instrument Field of View Size, Shape and Orientation
Camera-Matrix	CK	Orientation of Space Vehicle or any articulating Structure on it
Events	EK	Events Information
Other	FK	Reference Frame Specifications
Other	LSK	Leapseconds Tabulation
Other	SCLK	Spacecraft Clock Coefficients
Other	DSK	Digital Shape Models

Table 3.2: SPICE kernels

- *cspice_furnsh*: the routine cspice_furnsh loads SPICE kernel files into MATLAB;
- *cspice_kclear*: the routine cspice_kclear clears the KEEPER system: unload all kernels, clear the kernel pool, and re-initialize the system;
- *cspice_str2et*: the routine cspice_str2et converts a string representing an epoch to a double precision value representing the number of TDB seconds past the J2000 epoch corresponding to the input epoch;
- *cspice_spkezr*: the routine cspice_spkezr returns the state (position and velocity) of a target body relative to an observing body, optionally corrected for light time (planetary aberration) and stellar aberration. It is obviously necessary to define in input the time or the timespan of observation and the reference frame considered.

Chapter 4

Genetic Algorithm

In the context of analyzing space trajectories and escape manoeuvrs from Earth and Moon's sphere of influence in an n-Body Problem, the design and optimization of such trajectories represent a crucial challenge. The inherent complexity of these problems calls for advanced computational methods to effectively explore the solution space. Among various optimization approaches, Genetic Algorithms (GAs) emerge as a powerful tool to tackle the intricacies of space trajectories.

As explained in [32], GAs draw inspiration from the evolutionary mechanisms of nature, replicating the process of natural selection to generate optimal or near-optimal solutions. These algorithms are particularly well-suited for problems where the solution space is vast and intricate, as is the case with space escape manoeuvrs. In this study, a Genetic Algorithm specifically designed for pseud-optimizing space escape trajectories is presented. The GA plays a pivotal role in the research approach, enabling the exploration of a wide range of parameters and efficiently generating high-quality solutions.

In this Chapter, a detailed description of written GA will be provide, elucidating its key components and fundamental principles. It will also be examined how the GA has been applied to the specific space escape trajectories considered in this research. The goal is to offer a clear understanding of the crucial role played by the GA in optimizing space trajectories and how it contributes to the significant results achieved in the context of our investigation.

4.1 Optimisation Overview

This section will outline and categorize the techniques that can be utilized to tackle the optimization of space trajectories. These methodologies, when appropriately configured, are applicable to a wide range of scenarios beyond just astrodynamics. Depending on the specific problem being analyzed, certain methods may demonstrate varying degrees of effectiveness.

As widely clarified in [32], before tackling an optimization problem, three fundamental choices need to be made, which are crucial for the optimization itself: determining the *merit function* (or fitness function), identifying the *variables*, and establishing the *constraints*:

- The *merit function* represents the element of the problem that one actually aims to minimize. Constraints that the problem under analysis is subject to can also be included in the fitness function, so its correct choice is crucial for optimization purposes;
- The *variables* determine the value of the merit function. They can be chosen depending on the specific case. For example, when addressing an optimization problem of interplanetary orbit transfers, the variables could represent the thrust angle, transfer time, delta-V vector's components, etc;
- The *constraints* represent the limitations imposed on the variables. For example, if a variable represents the value of an angle, it can be limited to a specific interval.

When addressing an optimization problem, it is not always possible to find all the essential elements. Indeed, the existence of a merit function is not guaranteed; one may work with a known solution to verify if certain constraints are met. Conversely, in some cases, multiple fitness functions may exist, leading to what are known as multi-objective optimization problems. These multi-objective problems can also be simplified to single merit function optimization problems. Additionally, variables and constraints may not always be required in every optimization scenario.

Optimization problems are distinguished into two types[33]:

- local optimization problems;
- global optimization problems.

DEFINITION (*local minimum point*): A point x^* is called a local minimum if there exists an $\delta > 0$ such that for all $x \in \mathbb{R}^n$ satisfying $\|x - x^*\| < \delta$, we have $f(x^*) \leq f(x)$.

DEFINITION (*global minimum point*): A point x^* is called a global minimum if there exists a $\delta > 0$ such that for all $x \in \mathbb{R}^n$, we have $f(x^*) \leq f(x)$.

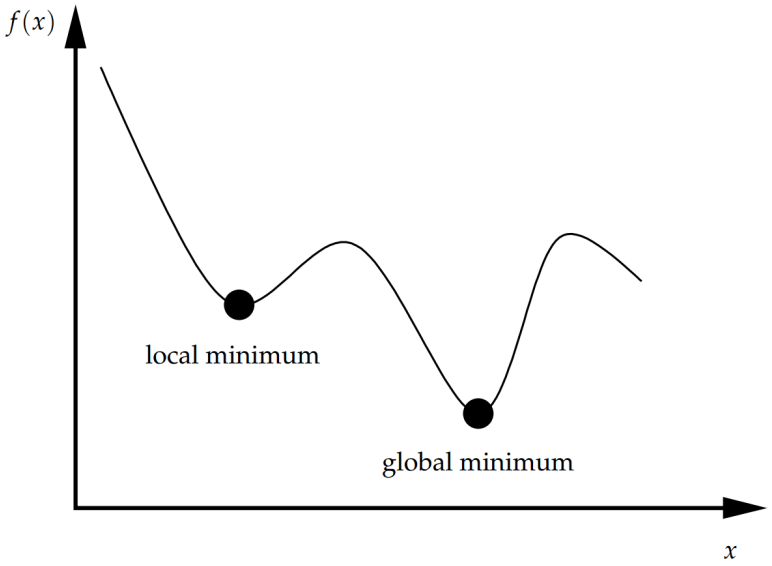

Figure 4.1: Local and global minima [34]

A schematic representation is shown in Figure 4.1. Taking full advantage of the ad-hoc genetic algorithm written for this thesis work, what we will do is search for some *pseudo-minimum points* that, physically, return a result of interest in terms of ballistic manoeuvering.

4.1.1 Local Optimisation methods

In general, methods to solve local minimum problems fall into two categories: *indirect methods* and *direct methods* [35] [36] [37] [38].

Indirect methods [32] [39] in optimization introduce a state vector and optimize the control variables indirectly by adjusting the initial values of this state vector. These methods are based on computing variations, and typically formulate the optimal control law as a Two Points Boundary Value Problem (TPBVP). An example of a function provided by MATLAB to solve TPBVP is the function called *bvp5c*. This function integrates a system of differential equations of the form $y' = f(x, y)$ subject to the boundary conditions described and the initial solution guess. To use *bvp5c*, it typically start by creating the initial guess. This initial guess also defines the points at which the boundary conditions are enforced.

The objective is to solve this problem in a manner that satisfies the final conditions and constraints. If a solution to the TPBVP is found, it represents an optimal solution for the specific initial conditions and constraints. However, obtaining a solution can be challenging due to the small convergence domain, which

is highly sensitive to the initial values of the variables and may not be intuitively clear. When optimizing space trajectories, the addition of gravity assist manoeuvrs further exacerbates the sensitivity to initial variables and reduces the convergence domain significantly.

To address these challenges, techniques are employed where a solution to a problem similar to the one being analyzed is known. The problem under analysis is then modified slightly and solved with the initial conditions of the known problem. This approach allows for obtaining a compatible optimal solution for the problem being analyzed. However, indirect methods are often difficult to implement with automatic and global optimization programs due to their long execution times and the small convergence region. Despite their convergence difficulties and limited robustness, indirect methods offer high numerical accuracy and require a low number of parameters.

In direct methods [32] [39], unlike indirect ones, there is continuous control, and the state variables are often discretized over certain time or length intervals. The result of this is a nonlinear programming technique that directly optimizes a specific performance index. In the case of interplanetary transfers, such a performance index can typically be the flight time or the amount of propellant used. Based on the performance index, discrete control variables are modified and optimized to satisfy boundary conditions and optimization criteria. There are several methods for discretizing control variables, and the choice of discretization strategy can significantly influence the final optimal solution. The number of control variables in the use of direct methods can become quite high, and for this reason, such types of problems are limited by current nonlinear programming techniques. Since direct methods discretize a continuous problem and although the accuracy of the results is sufficiently accurate for conceptual design analysis, the solution found is considered suboptimal. The main advantages of techniques using direct methods are high computational efficiency and robust convergence. The solution calculated with direct methods is less sensitive to initial conditions compared to those calculated with indirect methods. Additionally, these initial conditions are more physically intuitive compared to indirect methods. However, the choice of discretization for the purpose of calculating the optimal solution affects computation times. Indeed, very fine discretization, despite providing an accurate solution, results in significant computation times. For this reason, various discretization techniques have been calculated and tested, in order to guide those who want to use direct methods towards an optimal strategy for solving a specific problem.

Hybrid methods [32] [39] numerically integrate the Euler-Lagrange equations and control the vehicle through a vector. Like direct methods, hybrid methods

solve a nonlinear programming problem, but with the Euler-Lagrange multipliers completing part of the vector parameters while maximizing or minimizing some weight functions. Hybrid methods numerically search for a set of parameters that extremize the weight function while explicitly satisfying only the kinematic boundary conditions.

4.1.2 Global Optimisation methods

Global optimization algorithms [40] [41] can be broadly categorized into three main classes:

- **Stochastic Algorithms**: these algorithms start from a suitable choice of samples and are capable of manipulating these samples to find local minimum conditions. Stochastic algorithms are particularly useful in scenarios where the merit function is noisy or non-differentiable, making traditional gradient-based methods ineffective. Examples of stochastic algorithms include evolutionary algorithms, simulated annealing, and genetic algorithms;
- **Guaranteed Algorithms**: in contrast to stochastic algorithms, guaranteed algorithms are deterministic and capable of providing rigorous guarantees on the computation of a local minimum with high accuracy. These algorithms are often based on mathematical optimization techniques such as convex optimization or branch-and-bound methods;
- **Algorithms with Metamodels**: these algorithms leverage the construction of metamodels, which are simplified models used to represent complex systems, to search for a global optimal solution. An efficient exploration of the design space is enabled in scenarios where direct evaluation of the objective function is computationally expensive or time-consuming. Common techniques used in algorithms with metamodels include response surface methodology, kriging, and radial basis functions.

The stochastic algorithms further divide into two main subclasses:

- **Evolutionary Algorithms**: these algorithms aim to find a global solution by emulating the natural process of evolution: the most successful individuals are able to reproduce and persist into the next generation, thereby ensuring that the value of the fitness function improves over generations. However, there is a possibility that even individuals with low fitness can survive and reproduce;
- **Simulated Annealing**: these algorithms seek a global solution through iterative update steps. The magnitude of these updates is proportional to a predefined set of parameters, which function akin to a temperature. Similar

to the annealing process in metallurgy, the temperature is initially raised to facilitate rapid optimizations, and subsequently lowered to attain greater stability.

An additional subdivision of evolutionary algorithms is made into three subclasses:

- **Genetic Algorithms** (**GAs**): These algorithms (see Figure 4.2) conduct an exhaustive exploration of the space where the optimal solution might exist, as well as regions that may hold additional and superior solutions. Populations of individuals undergo modifications through the utilization of specific genetic operators, including mutation, crossover, and selection operators;
- **Evolutionary Programming**: The classical form of these algorithms involves the use of only one genetic operator, mutation, unlike GAs. They simulate natural evolution at the phenotypic level; furthermore, since a selection process is involved, these algorithms are based on a tournament selection. Such selection involves a population consisting of both parents and offspring individuals;
- **Evolutionary Strategies**: These algorithms are similar to Evolutionary Programming in that they simulate natural evolution at the phenotypic level, but with the difference that the selection operator is of a recombinative type.

Due to the complexity, the number of variables (multi-objectives optimization capabilities) involved and the interest in investigating a broader spectrum of possible trajectories (whether or not using Earth Gravity Assist (EGA) or Moon Gravity Assist (MGA)), using and writing a genetic algorithm proved to be the best choice.

4.1.3 Genetic Algorithm Overview

As seen above, a GA works as a stochastic optimization technique grounded in the biological principles of Darwinian evolution [42] [43]. It integrates operators that emulate natural selection and reproduction by employing a probabilistic search within a population of designs. The population undergoes evolutionary changes through the application of genetic operators, ultimately identifying the design most adapted to a given fitness landscape. This fitness landscape is delineated by a fitness function (previously named as merit function too) typically comprised of an objective function and a supplemental penalty function if the problem entails constraints. Unlike calculus-based methods, GAs are conceived as a framework for globally exploring the design space. They enable exploration of complex, expansive, and multimodal design spaces, unlike methods confined to locally optimal solutions in the vicinity of an initial estimate.

Genetic algorithms prove effective for challenging optimization problems characterized by nonconvexity, multimodality, or discontinuity in the design space. Nevertheless, while GAs excel in tackling complex problems, they are computationally intensive, often necessitating numerous function evaluations due to their population-based search. For continuous unimodal problems or situations where a local search suffices, traditional calculus-based techniques offer greater efficiency, demanding fewer function evaluations owing to their utilization of gradient information in a point-to-point search. Furthermore, as GAs do not leverage gradients, there exists no proof of convergence alike the Kuhn-Tucker conditions for calculus-based methods [44]. Moreover, GAs may not consistently achieve high precision due to the restricted resolution inherent in the binary encoding of design variables.

Additionally, genetic algorithms were not originally tailored for unconstrained problems, hence may exhibit limited efficacy in tightly constrained scenarios featuring small feasible regions. Despite these limitations, the GA emerges as a potent optimization tool for problems surpassing the capabilities of traditional methods. Its population-based formulation, albeit computationally burdensome, remains pivotal to its effectiveness. By incorporating probabilistic transition rules within a population rather than calculus-based rules for point-to-point search, GAs prove adept at optimizing problems devoid of gradient information, such as combinatorial or mixed problems. Moreover, the population-based approach endows GAs with the ability to avoid to *get stuck* in local optima. Through simultaneous exploration of multiple designs, the GA search process can strongly comprehensively traverse fitness landscapes characterized by numerous local optima [45].

4.2 Genetic Algorithms Structure

The GA is a computational method originally proposed by J.H. Holland in 1992 and inspired by the Darwinian theory of natural selection and inherits from it a consequent logic of nomenclature. The fundamental components of a GA include encoding cheme, chromosome representation, fitness (or merit) selection, and biological-inspired operators.

Each chromosome (see Fig. 4.3) comprises a defined number of elements referred to as "genes" (or characters, decoders). Each gene has the potential to influence the traits or behavior of one or more individuals. The genes pertaining to a specific individual are situated at specific positions termed as "string positions."

Typically, chromosomes (also referred to as strings, genotype or individuals) are represented as strings, where there are a defined number of loci or genes or characters (specific position on the chromosome). Each gene has the potential to influence the traits or behavior of one or more individuals. The genes pertaining to a specific individual are situated at specific positions termed as "string positions.

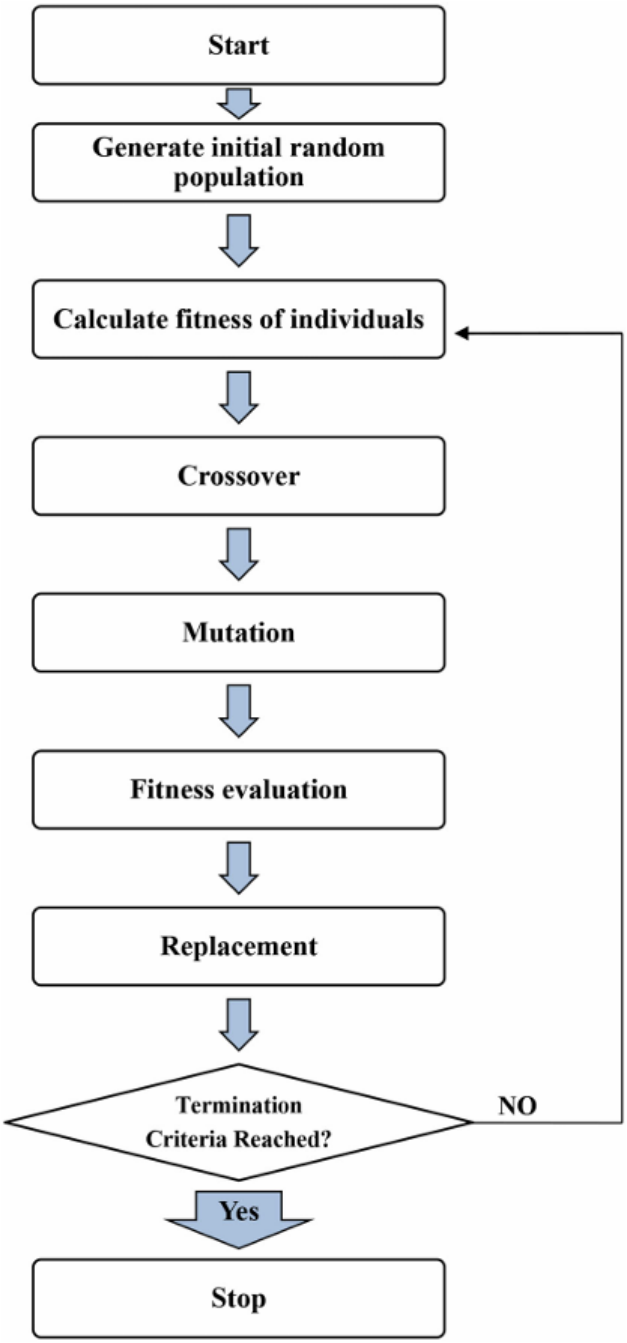

Figure 4.2: Basic structure of genetic algorithm [46]

These chromosomes serve as points in the solution space and undergo iterative processing through genetic operators, ultimately leading to the replacement of the

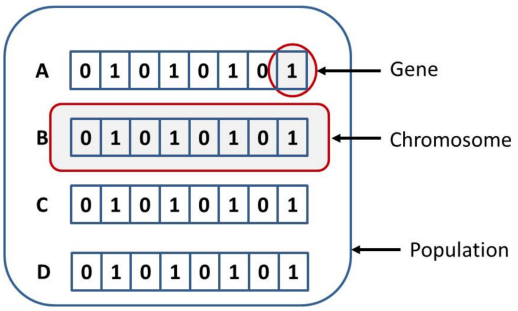

Figure 4.3: Population, Chromosomes and Genes

population.

A merit function is employed to assign a value to each chromosome in the population, aiding in fitness selection. The biological-inspired operators encompass selection, mutation, and crossover. During selection, chromosomes are chosen based on their fitness values for further processing. In the crossover operator, a random locus is selected, and subsequences between chromosomes are exchanged to generate offspring. Mutation involves randomly flipping some bits of the chromosomes based on a predefined probability [47].

4.2.1 Encoding Schemes

For most computational problems [47], the choice of encoding scheme—how information is converted into a particular form—is crucial. The information needs to be encoded into a specific bit string, and different encoding schemes are used depending on the problem domain [48].

Binary encoding is the most common scheme used. Each gene or chromosome is represented as a string of 1s and 0s [49]. In binary encoding, each bit signifies a characteristic of the solution. It facilitates quick implementation of crossover and mutation operations, although it requires additional effort for conversion and the algorithm's accuracy hinges on this conversion. The arrangement of the bit stream varies according to the problem. Binary encoding is not suitable for certain engineering design problems due to epistasis and natural representation issues.

In *octal encoding*, genes or chromosomes are represented as octal numbers (0–7), while hexadecimal encoding employs hexadecimal numbers (0–9, A-F) [50] [49]. Permutation encoding is typically used for ordering problems, where genes or chromosomes are represented by strings of numbers indicating their positions in a sequence.

Value encoding represents genes or chromosomes using strings of various values, which can be real numbers, integers, or characters [51]. This scheme is beneficial

for problems involving complex values where binary encoding may not suffice, such as in neural networks for determining optimal weights.

Tree encoding represents genes or chromosomes as trees of functions or commands, often resembling the structure of expressions in programming languages [52]. It is commonly used in evolving programs or expressions.

For the current study, a value encoding scheme was selected. Table 4.1 displays the various alleles defining the generic chromosome. The study was divided into two parts: initially focusing on the 3-Body Problem and subsequently transitioning to a more intricate high-fidelity model. However, the genetic algorithm developed was designed to provide flexibility in transitioning between these study phases. In this context, each individual consists of the perturbative *delta-V* of initial conditions and a specified mission duration.

ΔV	ϑ	φ	$\mathcal{T}$

Table 4.1: Genes of the generic individual

Moreover, this genetic approach employs the boundary problem principle, where the value constituting each individual's gene is selected within a lower and upper limit of the parameter being considered, randomly distributed between these bounds. Each individual will comprise four genes, structured as follows:

- ΔV: this gene represents, in absolute value, the velocity increment necessary to perturb the initial conditions and guide the spacecraft onto the trajectory, the quality of which will subsequently be evaluated by the merit function;

- ϑ: this gene represents the angle between the spacecraft's velocity vector and the direction of thrust exerted by the spacecraft's propulsion system within the plane of the velocity vector, commonly referred to as the in-plane thrust direction or simplier in-plane angle;

- φ: this gene represents the angle formed between the spacecraft's velocity vector and the direction of thrust applied by the spacecraft's propulsion system in a direction perpendicular to the plane of the velocity vector, commonly referred to as the out-of-plane thrust direction or simplier out-of-plane angle;

- $\mathcal{T}$: this gene represents the total duration of the manoeuvre, starting from the instant when the circular lunar orbit conditions are perturbed.

Equations (4.1) give an analytical writing of the initial condition.

$$x_{0,i} = x_\ell + h_0 \cdot \cos(\vartheta_i + \vartheta_\ell) \cdot \cos(\varphi_i + \varphi_\ell) \tag{4.1a}$$
$$y_{0,i} = y_\ell + h_0 \cdot \sin(\vartheta_i + \vartheta_\ell) \cdot \cos(\varphi_i + \varphi_\ell) \tag{4.1b}$$
$$z_{0,i} = z_\ell + h_0 \cdot \sin(\varphi_i + \varphi_\ell) \tag{4.1c}$$
$$u_{0,i} = u_\ell + V_C \cdot \cos(\vartheta_i + \vartheta_\ell + 90°) \cdot \cos(\varphi_i + \varphi_\ell) \tag{4.1d}$$
$$v_{0,i} = v_\ell + V_C \cdot \sin(\vartheta_i + \vartheta_\ell + 90°) \cdot \cos(\varphi_i + \varphi_\ell) \tag{4.1e}$$
$$w_{0,i} = w_\ell + V_C \cdot \sin(\varphi_i + \varphi_\ell) \tag{4.1f}$$

The initial conditions refer to the state immediately following the perturbation of the starting circular lunar orbit. Specifically, the state vector $X_{0,i} = \{x_{0,i},\, y_{0,i},\, z_{0,i},\, u_{0,i},\, v_{0,i},\, w_{0,i}\}$, where the subscript ℓ pertains to the Moon, and the subscript i pertains to the $i-th$ individual within the population, is composed of a combination of the following terms:

- (x, y, z): position information;
- (u, v, w): velocity information;
- ϑ: in-plane angle information;
- φ: out-of-plane angle information;
- V_C: starting circular lunar orbit velocity, in magnitude;
- h_0 starting circular lunar orbit height equal to 4000 km above the lunar surface.

where Moon's state vector has been obtained by the utilization of the NASA NAIF's SPICE toolkit and consequent ephemeris extraction, as seen in Section 3.3.

$$dv_{x,i} = \Delta V_i \cdot \cos(\vartheta_i + \vartheta_\ell + 90°) \cdot \cos(\varphi_i + \varphi_\ell) \tag{4.2a}$$
$$dv_{y,i} = \Delta V_i \cdot \sin(\vartheta_i + \vartheta_\ell + 90°) \cdot \cos(\varphi_i + \varphi_\ell) \tag{4.2b}$$
$$dv_{z,i} = \Delta V_i \cdot \sin(\varphi_i + \varphi_\ell) \tag{4.2c}$$

By recombining each other the different alleles of the $i-th$ chromosome, equations (4.2) are obtained and, accordingly to equations reported in (4.3), the initial conditions for the integration phase are defined.

$$\left\{c_{ini,i}\right\} = \begin{Bmatrix} x_{0,i} \\ y_{0,i} \\ z_{0,i} \\ u_{0,i} \\ v_{0,i} \\ w_{0,i} \end{Bmatrix} + \begin{Bmatrix} 0 \\ 0 \\ 0 \\ dv_{x,i} \\ dv_{y,i} \\ dw_{z,i} \end{Bmatrix} \tag{4.3}$$

4.2.2 Merit Function

The merit function serves as the milestone of the optimization process, embodying a multi-objective framework that encapsulates various criteria, objectives, and constraints inherent in the optimization problem. This multifaceted approach is crucial for tackling complex real-world scenarios where conflicting goals and trade-offs abound. Each objective or constraint integrated into the merit function represents a unique aspect of the optimization problem, spanning from minimizing fuel consumption to maximizing mission success probability, adhering to trajectory constraints, or meeting specific mission requirements.

The incorporation of multiple objectives enables a comprehensive evaluation of potential solutions. An essential aspect of the multi-objective fitness function involves assigning distinct weights to individual objectives and constraints. These weights convey the relative importance of each criterion within the optimization problem. Through careful adjustment of these weight assignments, specific objectives can be prioritized over others, aligning the optimization process with the mission's unique goals and priorities [32].

The significance of weight assignment cannot be exaggerated. It empowers decision-makers to finely adjust the optimization process, ensuring its precise alignment with objectives. In conclusion, the multi-objective nature of the merit function, coupled with deliberate weight allocation to objectives and constraints, enhances the versatility and efficiency of the genetic algorithm. This capability enables the algorithm to explore a broad spectrum of solutions.

During the course of the research, three distinct merit functions were adopted:

- The first merit function was tailored for analyzing the problem within the framework of the CR3BP, aiming to enable the spacecraft to achieve the WSB conducive to future ballistic escape maneuvers. The objectives are reported below:

  - *Apogee objective*: the primary objective is to achieve an altitude of 1.5 million kilometers above Earth's surface [53]. This objective is assigned the highest weight within the merit function, indicating its paramount importance in the optimization process;
  - *Apogee velocity objective*: the secondary objective is responsible for ensuring that the speed of the spacecraft within the WSB is as low as possible;
  - *Delta-V minimisation objective*: being at the preliminary stage of research, this objective helped to steer the range of delta-V modulus values required to bring the spacecraft into the WSB towards lower values.

- The second merit function leveraged the concept of Pareto efficiency, facilitating a multi-objective examination of the escape maneuver itself. This involved analyzing case studies that included or excluded gravitational slingshots within the HF model seen in Chapter 3, allowing for a comprehensive exploration of trade-offs and optimal solutions. The objectives are reported below:

  - *First apogee objective*: in order for the spacecraft to perform a ballistic escape, it must first reach a gravitational interdiction zone (previously recognised within the CR3BP as WSB). This objective ensures, in the course of evolution, that this target is reached;
  - *First apogee velocity objective*: similarly to what seen earlier, the spacecraft has to stay within high gravitational instability zone at a lower that is as low as possible;
  - *Last apogee objective*: once stationed in the ex-WSB, this objective allows the evolution of the species to be directed towards a family of trajectories in which the spacecraft is influenced by the gravitational attraction of the fourth-bodies to such an extent that it evades finding itself in a zone in which the patched-conics approximation can be consistently applied;
  - *Perigee objective*: this objective is an on/off switch objective and allowed for both trajectories that operated gravity assist and trajectories that did not.

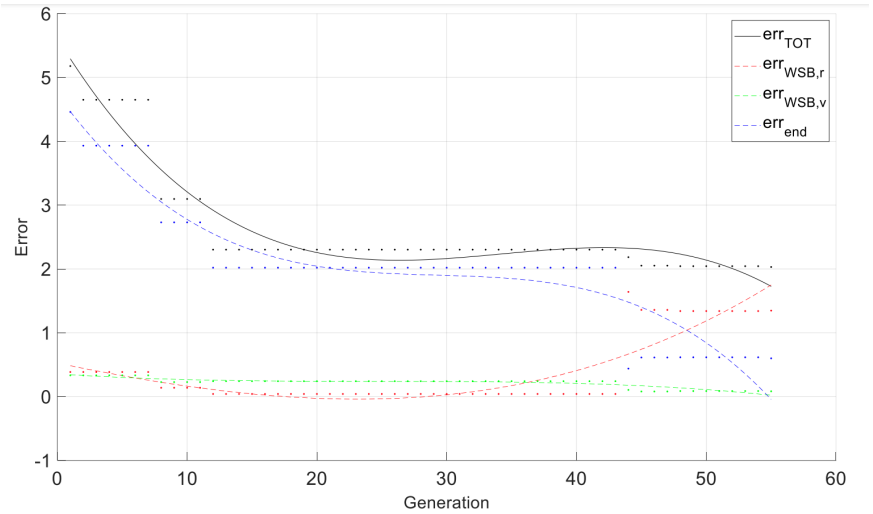

Figure 4.4: Multi-Objectives error trend

An example of genetic evolution guided by this merit function is shown in the Figure 4.4. From the figure, it is evident how the evolution is based on the concept of *Pareto Efficiency* [54].

DEFINITION (*Pareto Efficiency*): A solution (or individual) is considered Pareto efficient if there does not exist another solution in the set of considered solutions that is better in all objectives without being worse in at least one. In other words, a solution is Pareto efficient if it cannot be improved in all objectives simultaneously without worsening at least one of the objectives.

This definition of Pareto Efficiency is crucial in the context of genetic algorithms as it helps identify solutions that represent the best trade-offs among conflicting objectives. During the execution of the genetic algorithm, achieving Pareto efficient solutions aids in identifying the so-called "Pareto front," which represents the non-dominated solutions and hence the best possible alternatives.

- The third merit function was developed after defining the range of interest for the variables involved and refining the boundaries between them. This merit function enabled the differentiation of various solutions (elite trajectories) based on the energy level attained at the Earth-Moon binary system's escape. The objective is reported below:

  – *Specific mechanical energy objective*: this objective has allowed the search for trajectories that, by performing a ballistic escape, reach the same escape at different fixed energy levels (and consequently fixed velocities).

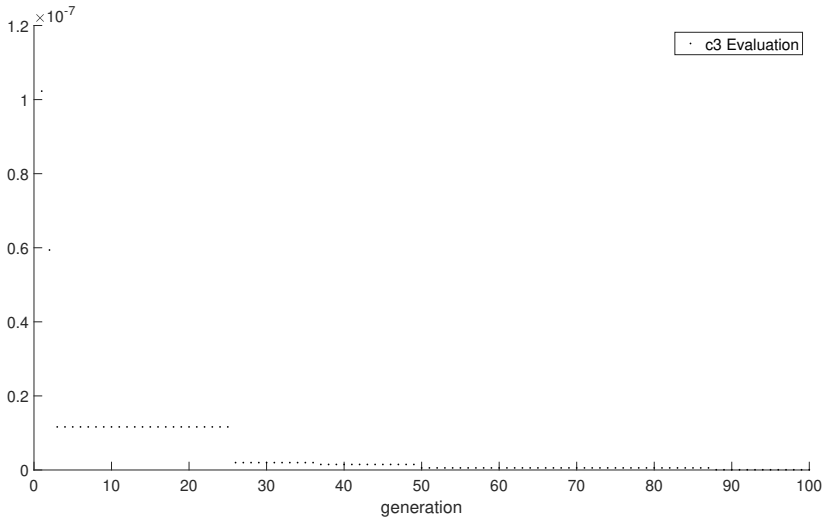

Figure 4.5: C3 error trend

Figure 4.5 illustrates how, from a perspective of sequential optimization, once the appropriate operating ranges for mission success have been identified, focusing solely on energy as the merit parameter allows for a better refinement of the desired final solution.

4.2.3 Selection techniques

As widely exposed in [47] [52], selection, a critical step in genetic algorithms, determines whether a particular string will participate in the reproduction process. This step is also known as the reproduction operator, and the convergence rate of a genetic algorithm depends on the selection pressure. Various selection techniques are employed, including roulette wheel, rank, tournament, Boltzmann, and stochastic universal sampling.

In *roulette wheel selection*, all possible strings are mapped onto a wheel portioned according to their fitness values. The wheel is then randomly rotated to select specific solutions for the next generation. However, this method suffers from errors introduced by its stochastic nature. To address this, De Jong and Brindle introduced determinism in the selection procedure.

Rank selection, a modified form of roulette wheel selection, assigns ranks based on fitness values, reducing the likelihood of prematurely converging solutions to local minima.

Tournament selection, proposed by Brindle, involves selecting individuals in pairs based on fitness values. Individuals with higher fitness values are added to

the next generation pool.

Stochastic universal sampling extends roulette wheel selection by selecting individuals at evenly spaced intervals from a random starting point. While it performs well for the Travelling Salesman Problem, traditional roulette wheel selection is more effective as problem size increases.

Boltzmann selection, based on entropy and sampling methods from Monte Carlo Simulation, mitigates premature convergence issues. It gives high probability to selecting the best string while executing quickly, although information loss may occur, which can be managed through elitism.

Elitism selection, introduced by K. D. Jong, ensures that the best individual from each generation is always propagated to the next. If the highest fitness individual is not selected through normal procedures, the elitist individual is automatically included in the next generation.

For the implementation of the genetic algorithm utilized in this study, the roulette wheel selection method was selected as the selection mechanism. In this approach, individuals were reordered based on their merit values, and an elitist strategy was employed. Specifically, only the top 30% of the best individuals proceeded to the next generation, while genetic operators such as crossover and mutation were applied to this subset to generate the complete new generation.

4.2.4 Crossover operators

Crossover operators are used to generate the offspring by combining the genetic information of two or more parents. The well-known crossover operators are single point, two-point, k-point, uniform, partially matched, order, precedence preserving crossover, shuffle, reduced surrogate and cycle [47].

In a *single-point crossover*, a random crossover point is selected, and the genetic information of two parents beyond that point is swapped with each other.

In *two-point* and *k-point crossovers*, two or more random crossover points are chosen, and the genetic information of the parents is swapped based on the segments created by these points.

In *uniform crossover*, parents are not decomposed into segments, and each gene is treated separately. The decision to swap genes with the corresponding location of another chromosome is made randomly.

Partially Matched Crossover is one of the most frequently used crossover operators, known for its superior performance compared to other methods. Proposed by D. Goldberg and R. Lingle, Partially Matched Crossover involves one parent donating a portion of genetic material, with the corresponding segment from the other parent contributing to the child. The remaining alleles are copied from the second parent once this process is completed.

Order Crossover, introduced by Davis in 1985, copies one or more parts of a parent to the offspring from selected cut-points, filling the remaining space with values other than those included in the copied section. While Order Crossover is beneficial for ordering problems, it's less efficient for the Traveling Salesman Problem.

Precedence Preserving Crossover maintains the ordering of individual solutions present in the parent offspring before applying crossover. The offspring is initialized with a string of random 1's and 0's to determine whether individuals from both parents are selected.

Shuffle Crossover, proposed by Eshelman, shuffles the values of an individual solution before and after crossover to reduce bias introduced by other techniques. However, its utilization has diminished in recent years.

Reduced Surrogate Crossover reduces unnecessary crossovers when parents have the same gene sequence for solution representations. It operates under the assumption that diverse parental genetic compositions yield better individuals.

Cycle Crossover, proposed by Oliver, generates offspring from parents by assigning each element's position based on their parents' positions. It iterates through cycles, taking elements from different parents to form the offspring.

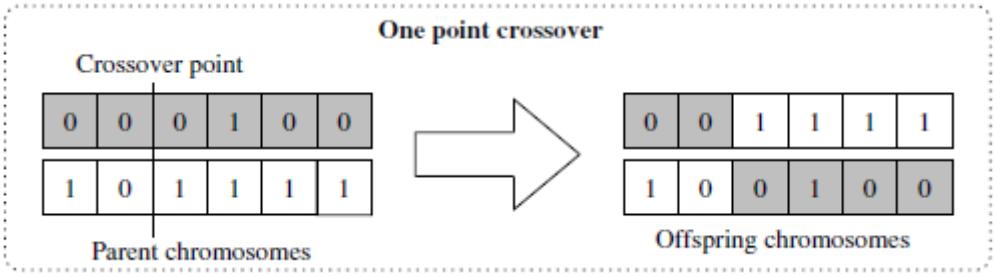

Figure 4.6: One-point crossover

In the implemented genetic algorithm of this work, a one-point crossover (see Fig. 4.6) was utilized, and three dice were defined for this purpose:

- *DICE 1*: randomly selects the index n at which the cut will occur, ranging from 1 to the length of the individual.
- *DICE 2*: randomly selects Parent 1 from among the elitists that have passed on to the next generation.
- *DICE 3*: randomly selects Parent 2 from among the elitists that have passed on to the next generation.

Additionally, it was stipulated that if *DICE 2* and *DICE 3* yield the same outcome, the throw must be repeated.

4.2.5 Mutation operators

Mutation is an operator crucial for maintaining genetic diversity from one population to the next. Common mutation operators include displacement, simple inversion, and scramble mutation [47].

Displacement mutation involves displacing a substring of an individual solution within itself. The displacement occurs at a randomly chosen position within the substring, ensuring the resulting solution remains valid and undergoes a random mutation. Variants of displacement mutation include exchange mutation and insertion mutation. In exchange mutation and insertion mutation, parts of the individual solution are exchanged with other parts or inserted at different locations, respectively [52].

The *simple inversion mutation operator* reverses the substring between two specified locations in an individual solution. It randomly selects a string and reverses it before placing it at a random location [52].

Scramble mutation shuffles the elements within a specified range of the individual solution in random order. The fitness of the resulting solution is then evaluated to determine if an improvement has occurred [52].

In this study, an additional die was introduced to perform a random genetic mutation in the GA. It was decided to carry out the mutation by *arithmetic averaging*: once Parent 1 and Parent 2 had been identified, the values of their respective genes were averaged. The implemented die is as follows:

DICE 4: Randomly identifies a number indicating the probability of mutation, which is then compared with the 'mutation rate'. In this case, the mutation rate was set at 0.05 (increasing much more the mutation doesn't occur). Therefore, the mutation is carried out on an individual only if the fourth die generates a number lower than the mutation rate.

However, the mutation rate must be handled with caution. A mutation rate that is too high can lead to a rapid loss of valuable genetic information within the population, making it difficult to converge on optimal solutions. Conversely, a mutation rate that is too low may reduce the effectiveness of the genetic algorithm in generating new solutions and diversifying the population.

Furthermore, to enhance genetic diversification even further, it was decided to introduce up to 5% new individuals per generation.

Below, in Figure 4.7, is a graph summarizing the operational process of the genetic algorithm described in this chapter.

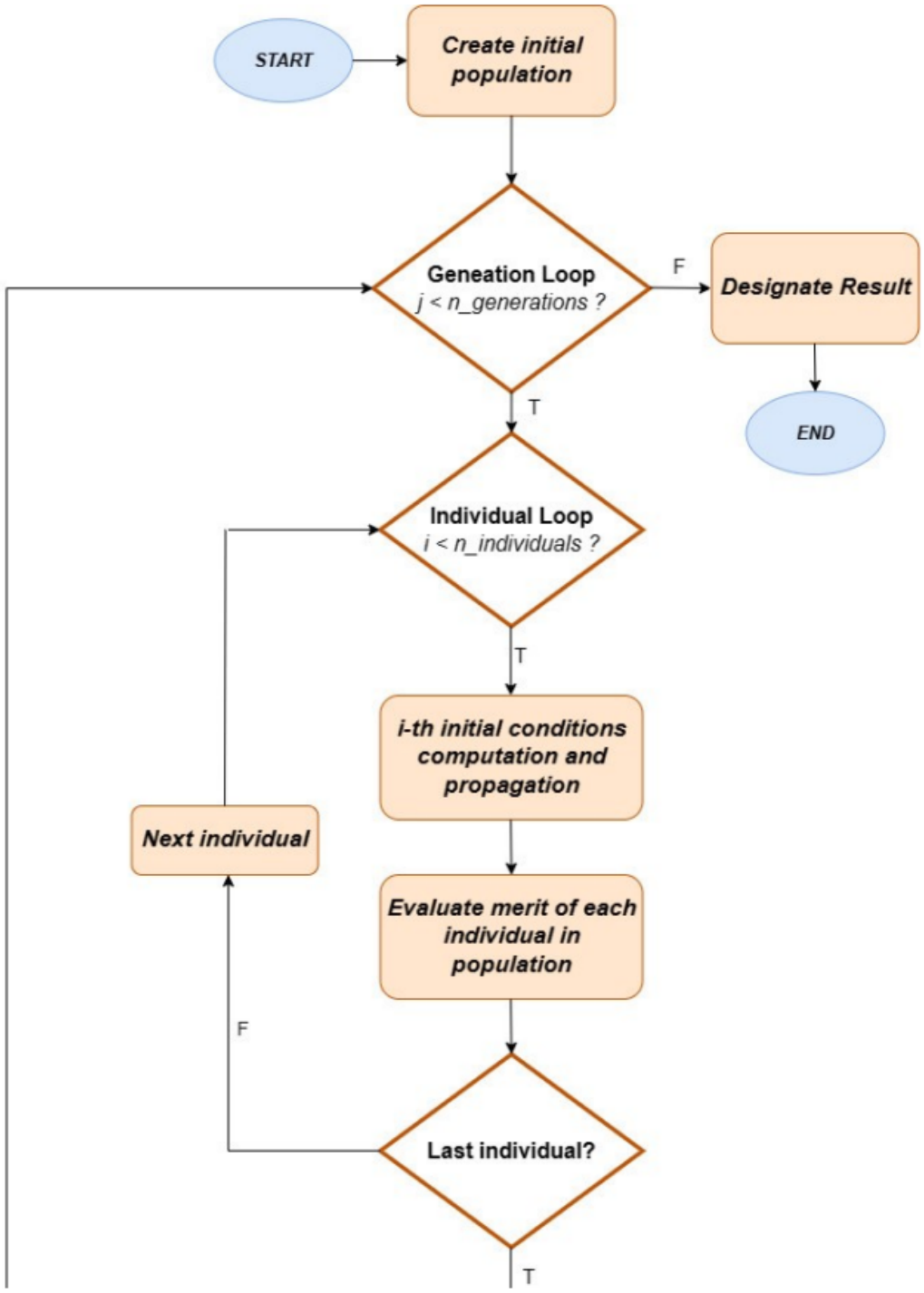
START
Create initial population
Geneation Loop
j < n_generations ?
F
Designate Result
END
T
Individual Loop
i < n_individuals ?
T
i-th initial conditions computation and propagation
Evaluate merit of each individual in population
Last individual?
F
Next individual
T

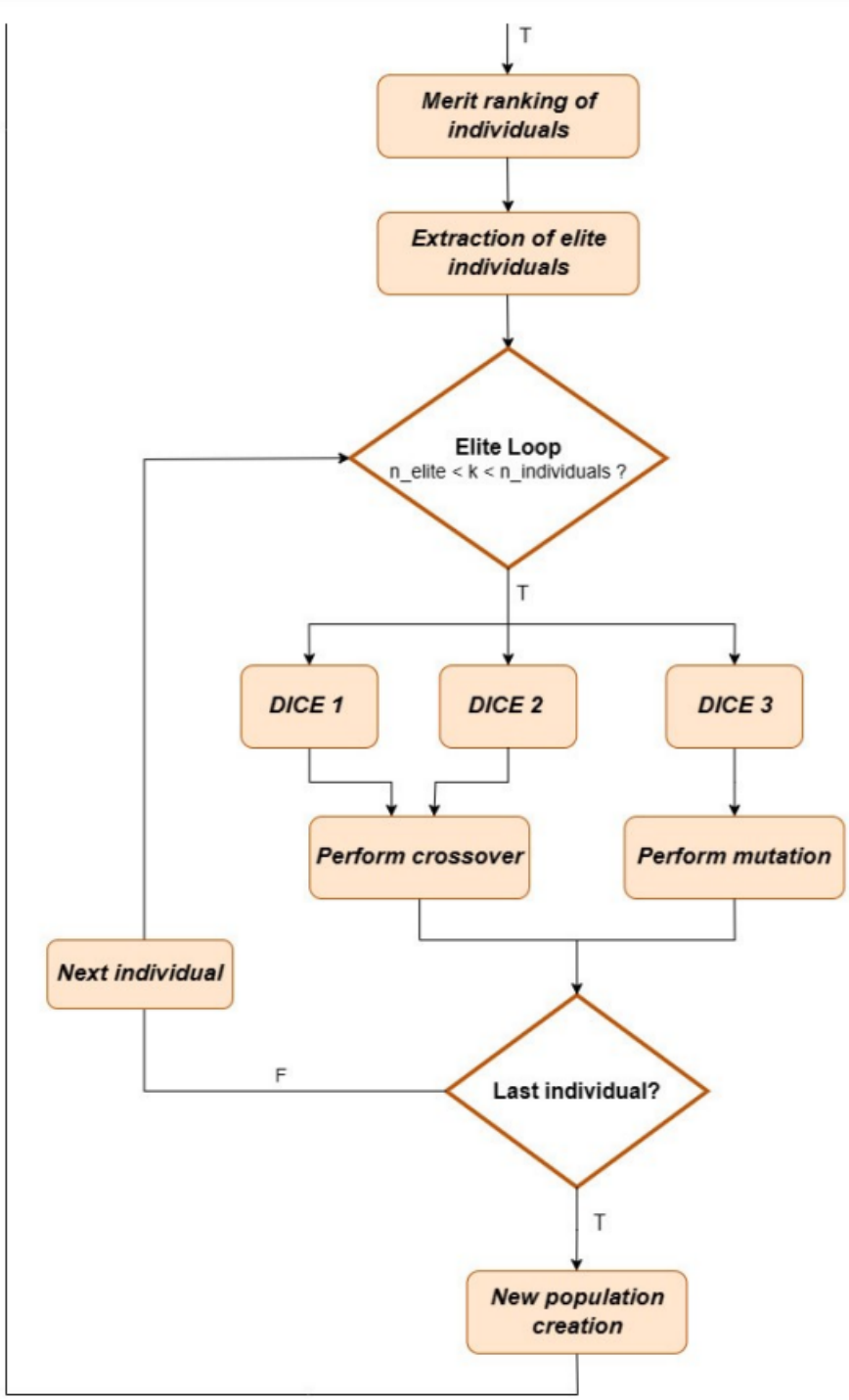

Figure 4.7: Structure of the genetic algorithm

Chapter 5

Ballistic Escape Trajectories from Earth-Moon Binary System

When it comes to space missions, particularly interplanetary ones, the concept of cost emerges as one of the primary constraints to human exploration of the universe. In this regard, the study of low-cost maneuvers capable of leveraging various gravitational effects becomes of paramount importance for both manned and unmanned missions.

Departing from the concept of manned missions and thus allowing for greater flexibility in terms of mission duration, the present research aimed to analyze the different families of trajectories enabling a ballistic escape from the Earth-Moon binary system.

Initially focusing on reducing the cost of escape with a view towards a Martian expedition, it was later realized that this type of maneuver could also be highly beneficial for reaching other smaller celestial bodies such as asteroids.

5.1 Estimate of launch date

As clarified in [55], the Porkchop plots are clear and straightforward graphical tools that assist mission designers in carefully planning the most convenient dates for scheduling a transfer between two celestial bodies. These charts consist of contour curves that can represent the value of various parameters as a function of the departure date and arrival date. One of the key parameters for determining the feasibility of a mission is the total transfer cost delta-V, in terms of the velocity difference required to perform the necessary maneuvers.

In consideration of the specific mission requirements, a strategic approach was implemented, necessitating the utilization of two distinct Porkchop plots.

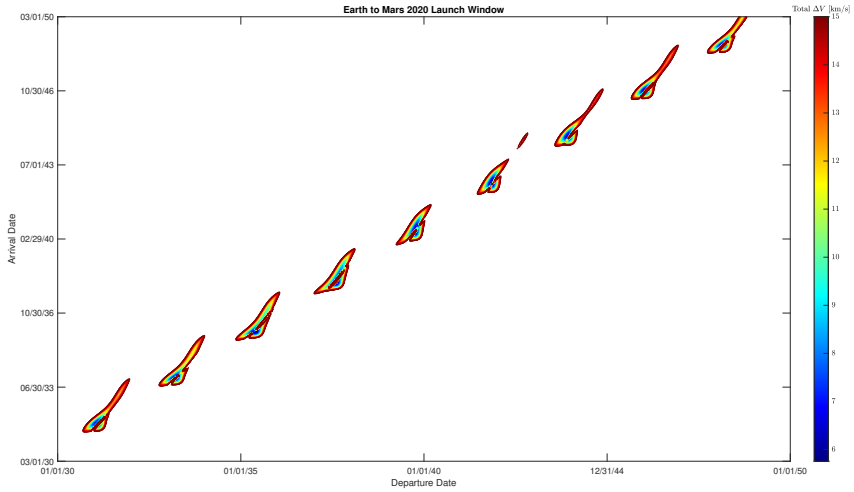

Figure 5.1: Big temporal span Porkchop Plot

The initial plot, shown in Figure 5.1, covering the period from 2030 to 2050 and helps the research work to find a first time window of inetrest.

The computational expense associated with the dynamic model and integration outlined in Chapter 3 is notably considerable. Within the scope of the analysis at hand, conducting simulations across a 20-year launch window was deemed impracticable. Consequently, the focus shifted towards examining the solution space of minimum delta-V within the Porkchop Plot in Fig 5.1.

The second plot (see Fig. 5.2) represented a concentrated effort aimed at pinpointing the absolute minima within the Porkchop family, crucial for identifying optimal transfer windows. This meticulous approach enabled us to pinpoint the most cost-effective and energetically efficient solutions, consequently minimizing requirements and overall mission costs.

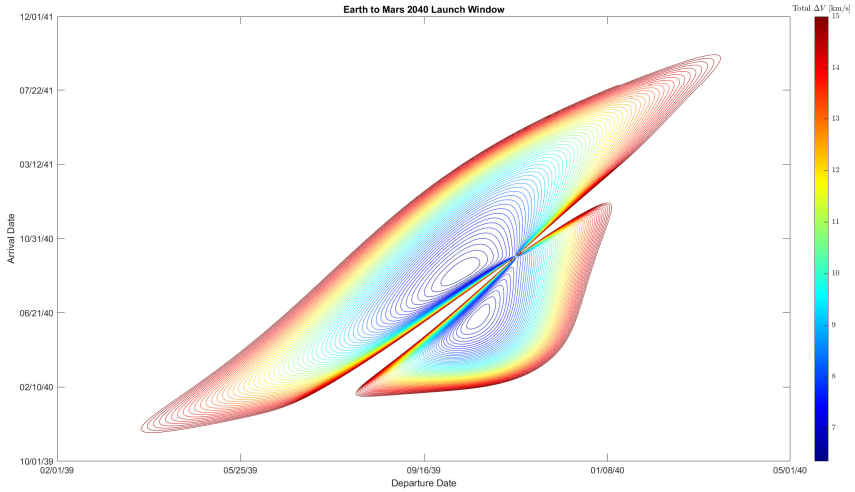

Figure 5.2: 2039 Porkchop Plot

As is evident, these Porkchop Plots, despite incorporating ephemerides, do not directly address Lambert's problem for a ballistic trajectory. Consequently, transer time required to escape from the SOI increases, and the area of interest was estimated to be slightly earlier in time.

5.2 Ballistic escape trajectories with time constraint

With the Porkchop Plot studies in mind, it was decided to focus the research by conducting the analysis on a smaller number of dates:

- 21th March 2039;
- 21th June 2039;
- 21th September 2039.

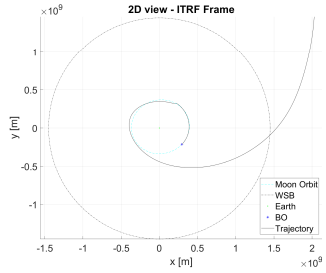

(a) *21/03/2039, Earth-centered frame*

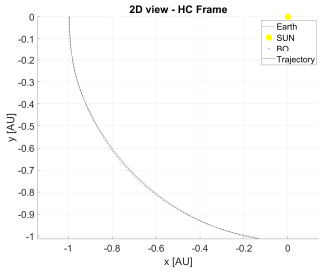

(b) *21/03/2039, Sun-centered frame*

Figure 5.3: The shown orbit is calculated in order to have a final specific mechanical energy value equals to $0.2\text{km}^2/\text{s}^2$

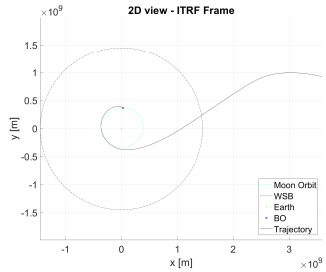

(a) *21/06/2039, Earth-centered frame*

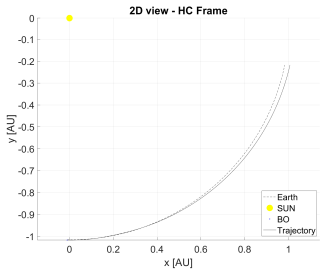

(b) *21/06/2039, Sun-centered frame*

Figure 5.4: The shown orbit is calculated in order to have a final specific mechanical energy value equals to $0.2\text{km}^2/\text{s}^2$

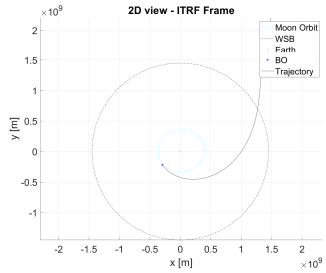

(a) *21/09/2039, Earth-centered frame*

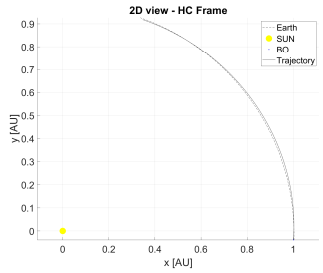

(b) *21/09/2039, Sun-centered frame*

Figure 5.5: The shown orbit is calculated in order to have a final specific mechanical energy value equals to $0.2\text{km}^2/\text{s}^2$

In figures 5.3, 5.4, and 5.5, the escape trajectories from the Earth-Moon binary

system for the three initial attempt dates are depicted. As can be observed from the results displayed in the heliocentric frame (figures (b)), the outcomes are consistent with what was seen in the figures 2.19 and 2.20 and presented in [11].

The trajectories just shown were derived from the elite individuals obtained downstream of the genetic algorithm. Starting from these, the initial lunar orbit was perturbed as seen in Chapter 4, following the equations reported here for convenience (see equations (5.1),(5.2) and (5.3))

$$x_{0,i} = x_\ell + h_0 \cdot \cos(\vartheta_i + \vartheta_\ell) \cdot \cos(\varphi_i + \varphi_\ell) \tag{5.1a}$$
$$y_{0,i} = y_\ell + h_0 \cdot \sin(\vartheta_i + \vartheta_\ell) \cdot \cos(\varphi_i + \varphi_\ell) \tag{5.1b}$$
$$z_{0,i} = z_\ell + h_0 \cdot \sin(\varphi_i + \varphi_\ell) \tag{5.1c}$$
$$u_{0,i} = u_\ell + V_C \cdot \cos(\vartheta_i + \vartheta_\ell + 90°) \cdot \cos(\varphi_i + \varphi_\ell) \tag{5.1d}$$
$$v_{0,i} = v_\ell + V_C \cdot \sin(\vartheta_i + \vartheta_\ell + 90°) \cdot \cos(\varphi_i + \varphi_\ell) \tag{5.1e}$$
$$w_{0,i} = w_\ell + V_C \cdot \sin(\varphi_i + \varphi_\ell) \tag{5.1f}$$

$$dv_{x,i} = \Delta V_i \cdot \cos(\vartheta_i + \vartheta_\ell + 90°) \cdot \cos(\varphi_i + \varphi_\ell) \tag{5.2a}$$
$$dv_{y,i} = \Delta V_i \cdot \sin(\vartheta_i + \vartheta_\ell + 90°) \cdot \cos(\varphi_i + \varphi_\ell) \tag{5.2b}$$
$$dv_{z,i} = \Delta V_i \cdot \sin(\varphi_i + \varphi_\ell) \tag{5.2c}$$

$$\left\{c_{ini,i}\right\} = \begin{Bmatrix} x_{0,i} \\ y_{0,i} \\ z_{0,i} \\ u_{0,i} \\ v_{0,i} \\ w_{0,i} \end{Bmatrix} + \begin{Bmatrix} 0 \\ 0 \\ 0 \\ dv_{x,i} \\ dv_{y,i} \\ dw_{z,i} \end{Bmatrix} \tag{5.3}$$

In Table 5.1, the individuals that generated the above trajectories are listed.

It is noted how the constraints imposed through the genetic algorithm were able to guide the evolution towards a specific family of ballistic escape trajectories. In particular, in this case, a constraint was added to the maneuver time alongside the merit function related to SME, varying it between 70 and 85 days. At this point in the discussion, it is important to make some observations:

OBSERVATION I (*Non-planar dynamic model*): in this study, the introduction of information on planetary ephemerides extracted from NASA's SPICE Toolkit

	ΔV [m/s]	In-plane angle ϑ[deg]	Out-of-plane angle φ[deg]	Time of transfer $\mathcal{T}$[days]
21/03/2039	357.4652	54.4750	109.2536	84.5
21/06/2039	370.5233	191.0265	-59.2879	80.0
21/09/2039	363.2421	321.3541	-35.6438	72.5

Table 5.1: List of individuals for fixed time and SME equals to $0.2\text{km}^2/\text{s}^2$

has allowed for the complication of the model by taking into account the non-planar components of positions and velocities. In other words, this means that the escape is enabled not only in coplanar terms but also in extraplanar terms. The potential applicability of these transfers for reaching minor celestial bodies such as asteroids is evident.

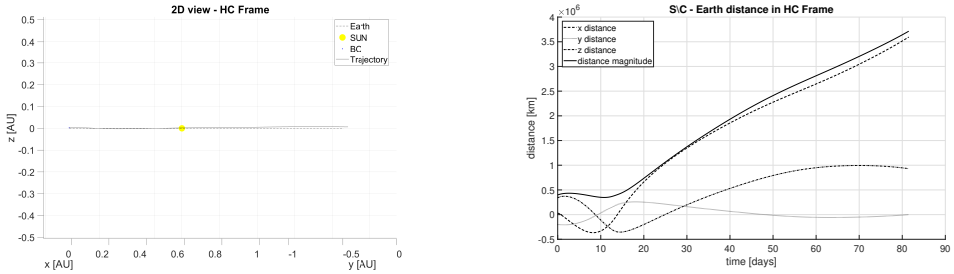

(a) *Sun-centered frame* **(b)** *Earth-SC distance*

Figure 5.6: For semplicity, the 21/06/2039 orbit is the only one shown. Analogous considerations can be mande on the other ones

Figure 5.6 shows how the spacecraft explores regions outside the fundamental plane of the heliocentric frame.

OBSERVATION II (*Moon Gravity Assist*): the presence of a MGA provides a velocity boost to the trajectory. This allows reaching certain regions of space while reducing the cost of access to them.

In Figure 5.7, the trends of SME are depicted and compared between a case featuring MGA and a case without it. In the 5.7(a), it's evident how MGA leads to a peak in mechanical energy due to the sudden velocity increase, akin to a free delta-V.

In both cases, the energy trends reflect those typical of a ballistic escape; the mathematical condition is reported below (for simplicity) and is respected.

$$\mathscr{C}_3(\varphi(t)) < 0, \quad \text{for } t < t_1 \qquad \text{and} \qquad \mathscr{C}_3(\varphi(t)) \geq 0, \quad \text{for } t \geq t_1 \tag{5.4}$$

where the SME is denoted by $\mathscr{C}_3$.

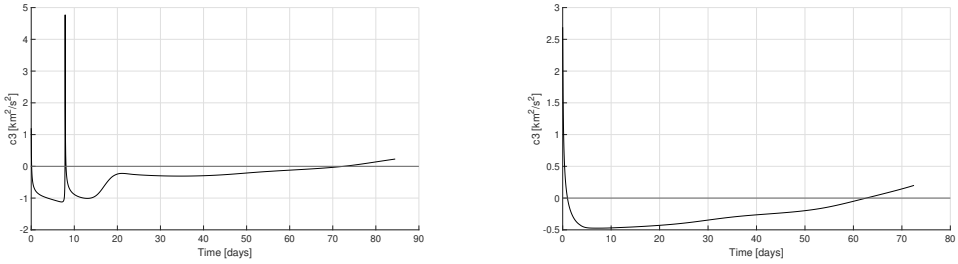

(a) *SME trend with MGA* **(b)** *SME trend without MGA*

Figure 5.7: SME trend comparison between trajectories with or without MGA

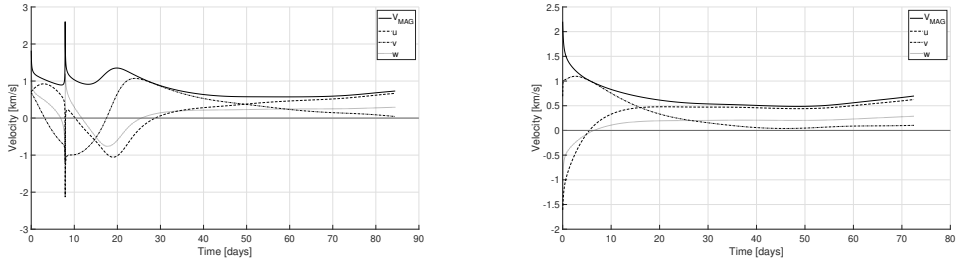

(a) *Velocity trend with MGA* **(b)** *Velocity trend without MGA*

Figure 5.8: Velocity trend comparison between trajectories with or without MGA

As anticipated, Figure 5.8 reveals how increases in energy translate into increases in speed (and vice versa) and make the presence or absence of Gravity Assist clearly recognisable.

OBSERVATION III (*Inner and outer orbits*): adopting a ballistic escape trajectory certainly allows for escaping the primary gravitational attraction of the Earth-Moon binary system, leveraging the gravitational influence of the Sun (and secondarily of other celestial bodies) to position oneself on an orbit that allows for the patched-conics approximation.

This orbit, as shown in Figure 5.9, can be inner or outer, enabling missions both towards inner and outer planets relative to the departure planet (Earth in this case).

5.2.1 Solar radiaton pressure influence

During the escape, the Sun evolves in its (apparent) motion with respect to the Earth in the EME2000 RF, producing a varying over time perturbation. As anticipated in Section 3.1.1, the solar perturbation, under simplifying assumptions,

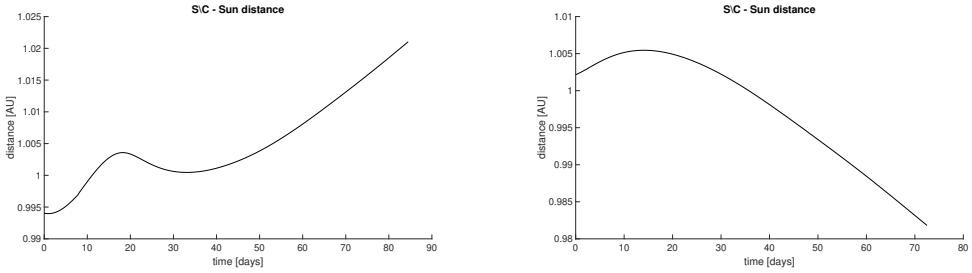

(a) *Outer orbit* **(b)** *Inner orbit*

Figure 5.9: Outer and inner orbits

produces a net perturbing acceleration in the radial and tangential directions of the SC, reported here from equations (3.5a) and (3.5b) for clarity

$$(\vec{a}_{ss\backslash c} - \vec{a}_{sE}) \cdot \hat{u}_j = \frac{3}{2}\frac{\mu_s}{r_s^3}\sin\left[2(\vartheta_s - \vartheta)\right] \tag{5.5a}$$

$$(\vec{a}_{ss\backslash c} - \vec{a}_{sE}) \cdot \hat{u}_i = \frac{3}{2}\frac{\mu_s}{r_s^3}\{1 + \cos\left[2(\vartheta_s - \vartheta)\right]\} \tag{5.5b}$$

Equations (5.5a) and (5.5b) show that it is possible to enclose the perturbation effect dependence on the Sun-SC position in two proportionality terms [1]

$$\varsigma_v = \sin 2\Delta\vartheta \tag{5.6a}$$

$$\varsigma_u = 1 + \cos 2\Delta\vartheta \tag{5.6b}$$

where $\Delta\vartheta$ is the angular difference between the Sun and the spacecraft.

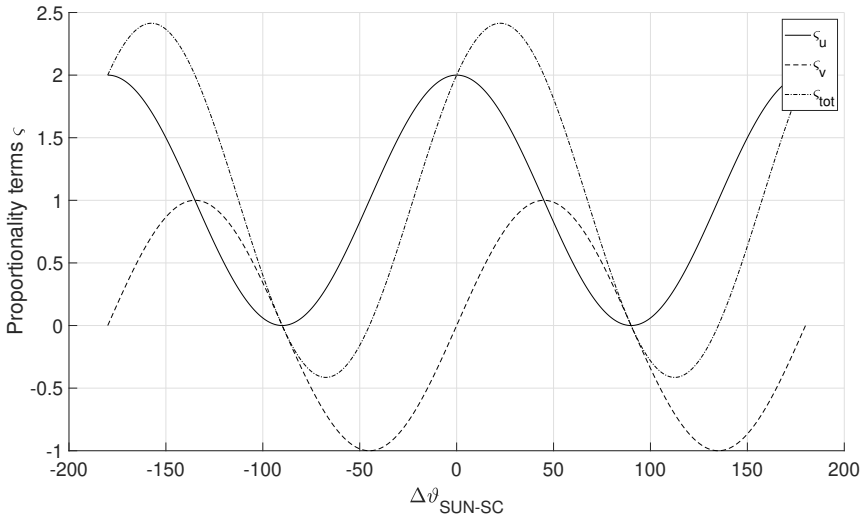

Figure 5.10: Tangential and radial components of the lunisolar perturbative effect ς_v and ς_u

In general, as shown in Figure 3.2,the combined effect of the two solar perturbation components may produce an overall positive effect on the spacecraft energy when the Sun is either close to $-157.5°$ or $22.5°$ with respect to the Earth–spacecraft direction.

Starting from this premise, it is possible to analyze the influence of this perturbative effect on the trajectories studied so far within this chapter. For each ballistic escape trajectory, a polar plot is proposed, which is able to convey information about the spacecraft's distance from Earth, the relative position between the spacecraft and the Sun, and the gravitational influence of the latter.

In Figure 5.11, the escape is enabled for values of $\Delta\vartheta$ between 0 and 30 degrees, when the perturbative effect provides a positive contribution.

In Figure 5.12, the escape is enabled for values of $\Delta\vartheta$ between 0 and 60 degrees, when the Earth-SC distance increases substantially.

In Figure 5.13, the escape is enabled for values of $\Delta\vartheta$ between 120 and 180 degrees, when, similarly with the firt one, the perturbative effect provides a positive contribution.

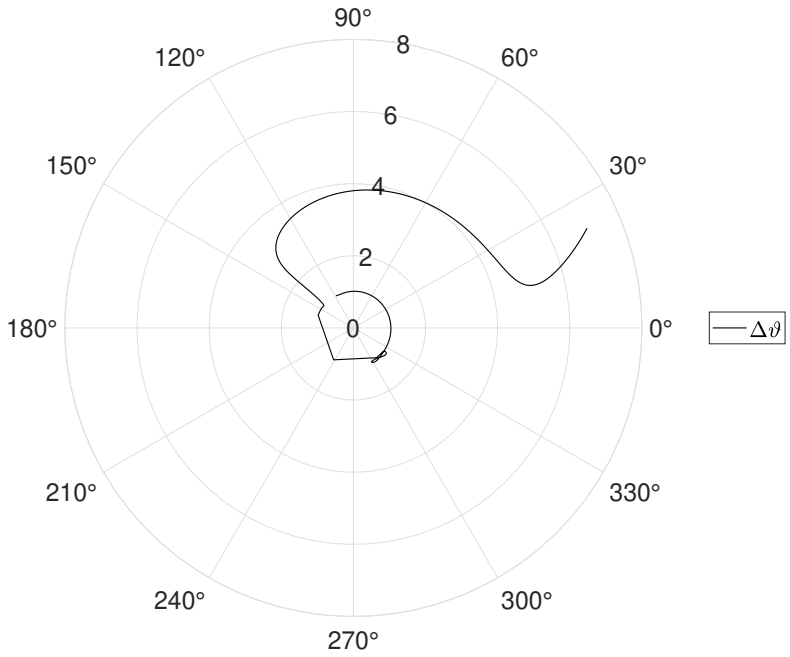

Figure 5.11: Solar perturbative effect on 21/03/2039 trajectory

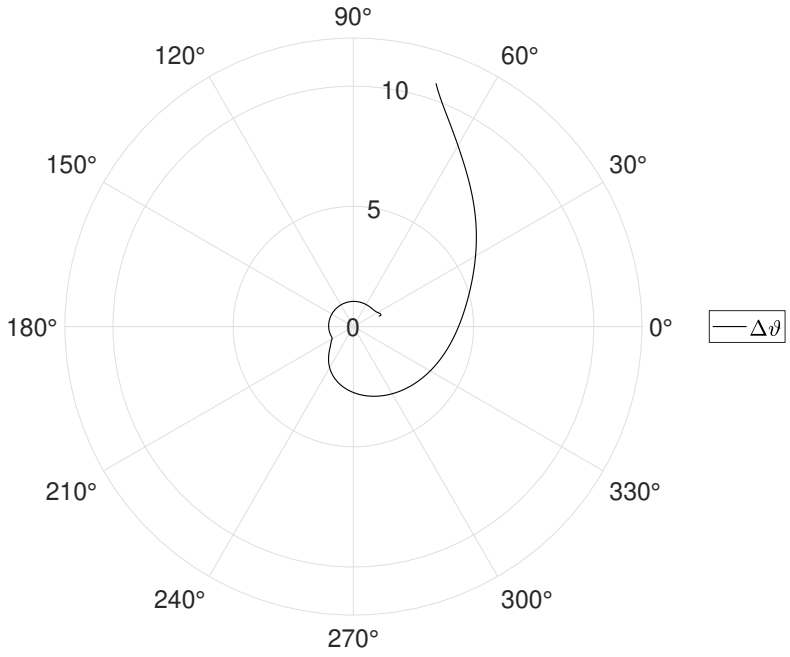

Figure 5.12: Solar perturbative effect on 21/06/2039 trajectory

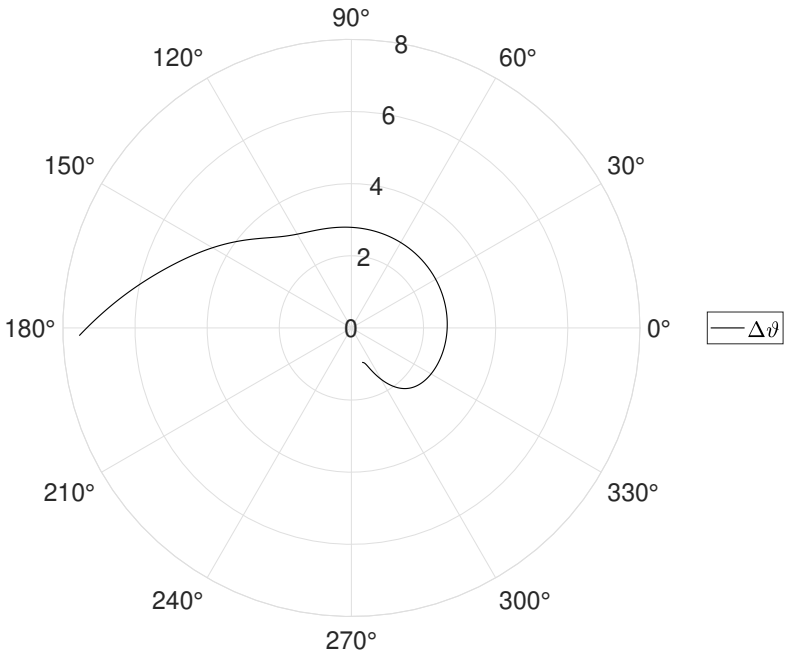

Figure 5.13: Solar perturbative effect on 21/09/2039 trajectory

5.3 Ballistic escape trajectories with time constraint free

By increasing the available time range for performing the escape maneuver, genetic evolution enables other families of trajectories that are distinguished by certain phenomena:

- Earth Gravity Assist;
- Waiting orbit;

5.3.1 Earth gravity assisted trajectory

Similarly to what was seen with the Moon, it is possible to construct trajectories that leverage the Earth's gravitational slingshot. In the case of MGA, the advantage lies in the spacecraft's position in space, already near the Moon's orbit. In this case, however, to enable an Earth gravity assist, the trajectory must be constructed in such a way that it first reaches the region of gravitational influence (defined as WSB in the PCR3BP) and then triggers a temporary capture towards the primary body.

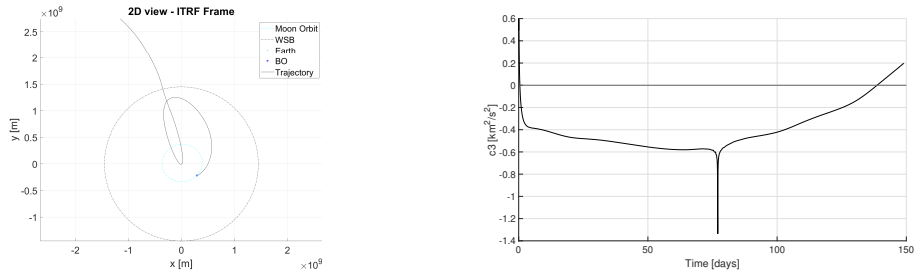

(a) *EGA trajectory* **(b)** *EGA trajectory SME trend*

Figure 5.14: The Figure puts the focus on a trajectory that exploit an Earth Gravity Assist

Figure 5.14(a) and Figure 5.14(b) show, respectively, the obtained trajectory (with a view in the plane) and the energy trend that certifies the success of the ballistic trajectory search. In particular, in Figure 5.14(b), the energy jump due to the EGA is evident.

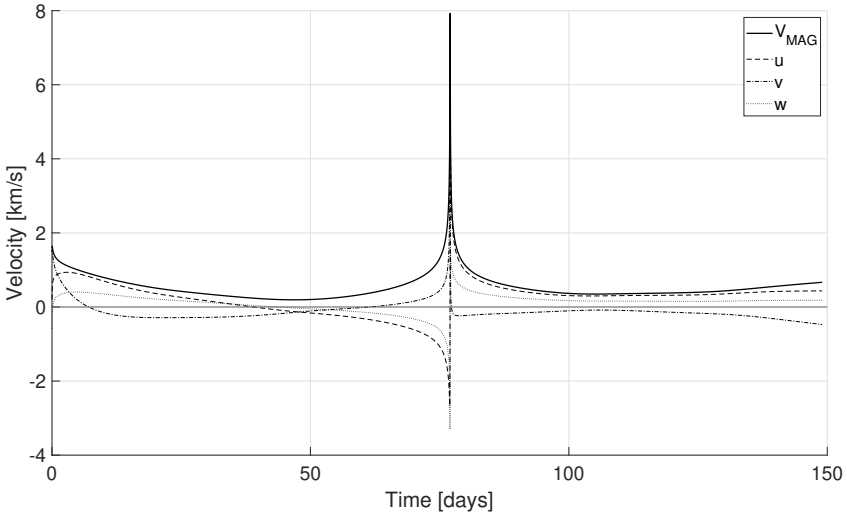

Figure 5.15: EGA trajectory velocity trend

Similarly to what was seen with the MGA, in this case too, the energy jump is synonymous with a speed boost. It's evident that if compared to Figure 5.8, the peak in speed is much higher, indicating that an Earth gravity assist is much more impactful on the energy and velocity profiles, as one might expect. Meanwhile, the losses due to staying for longer times in the gravitational influence zone of the Earth-Moon binary system are greater.

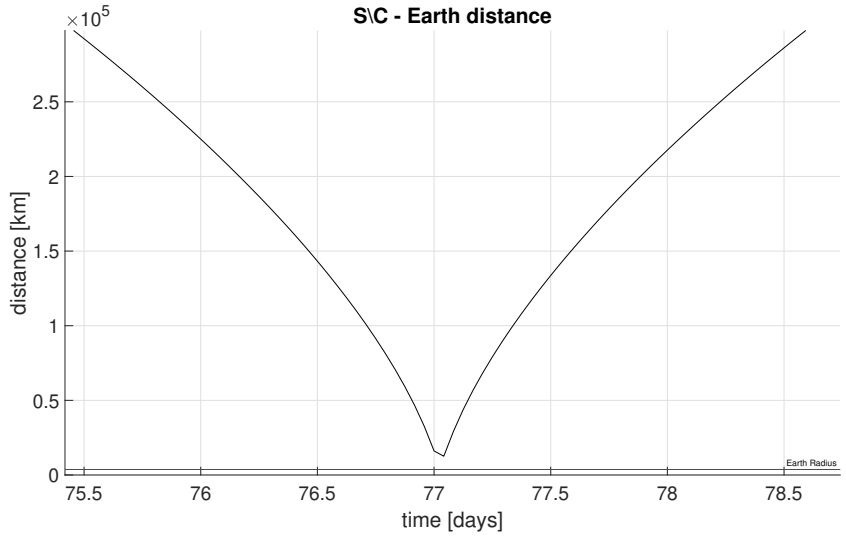

Figure 5.16: Feasibility of the EGA

In Figure 5.16, the focus is on the actual feasibility of the gravity assist maneuver with Earth. The horizontal line represents the value, in kilometers, of the Earth's equatorial radius and shows that the spacecraft does not approach excessively. It is noted that, in this study, the perturbative effect of atmospheric drag has been neglected, although it can be more or less influential for maneuvers of this kind; however, for altitudes on the order of 10^4km (akin happened for this perigee), this approximation is considered acceptable.

Again, Figure 5.17 shows how the ballistic escape is enabled for values of $\Delta\vartheta$ included between 25° and 90°.

	ΔV [m/s]	In-plane angle ϑ[deg]	Out-of-plane angle φ[deg]	Time of transfer $\mathcal{T}$[days]
21/03/2039	359.7132	58.9820	-22.5161	149

Table 5.2: Individual for EGA trajectory and SME equals to $0.2\text{km}^2/\text{s}^2$

Table 5.2 reports the characteristics of the elite individual selected downstream of the genetic algorithm, with the perigee objective considered within the merit function (see Chapter 4). The delta-V is similar to that obtained for the trajectory that exploits MGA, but the transfer time is significantly higher.

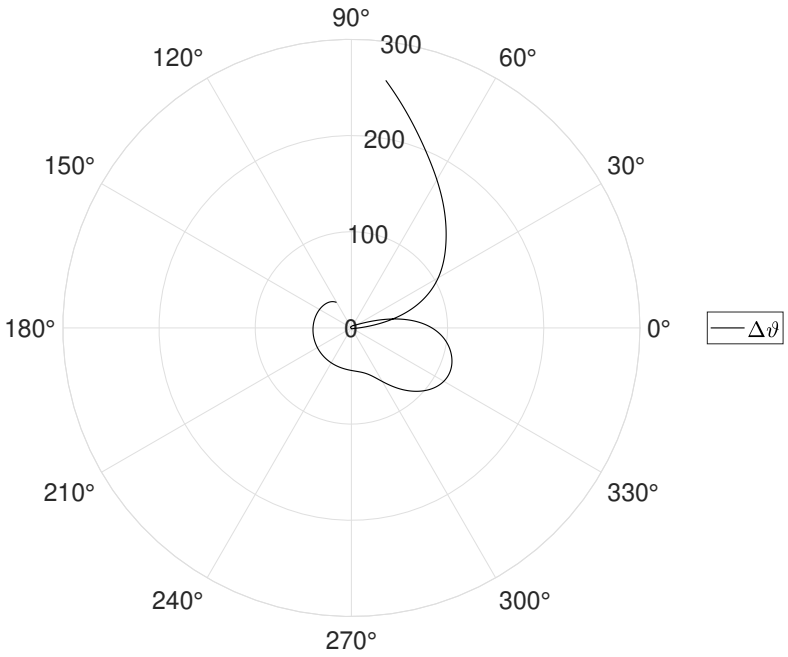

Figure 5.17: Solar perturbative effect on Earth Gravity Assisted orbit

5.3.2 Trajectory exploiting waiting orbit

Other families of trajectories analyzed within the study are those that involve the spacecraft's station-keeping on a certain number of waiting orbits (WOs) while waiting to achieve the necessary energy condition for the ballistic escape to occur. These waiting trajectories can occur around either the Earth or the Moon.

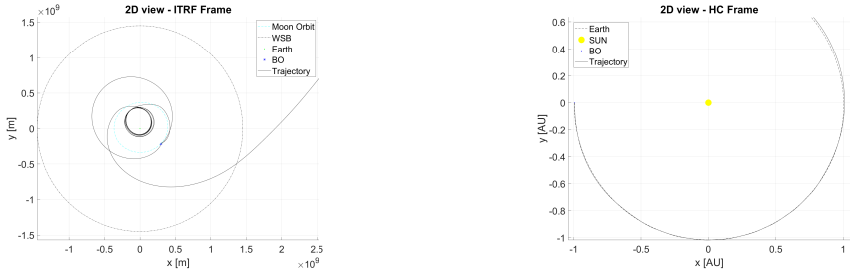

(a) *WO trajectory* **(b)** *WO trajectory HC frame*

Figure 5.18: The Figure puts the focus on a trajectory that exploit WOs

Figure 5.18 shows a trajectory that utilizes WOs around the Earth. In the first plot, it's possible to observe the trajectory in a reference frame centered on the Earth, while in the second plot, the outer orbit in the heliocentric system is

observable in its planar view.

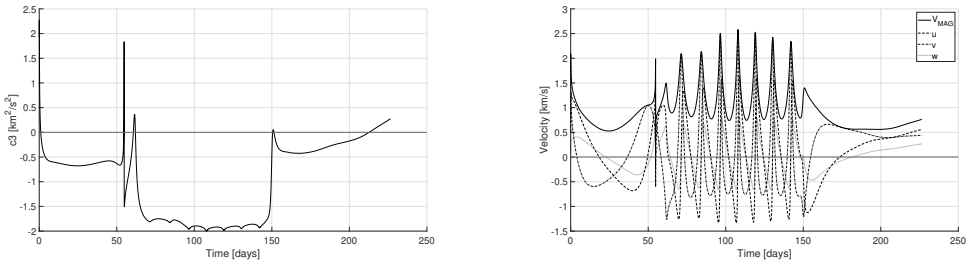

(a) *SME trend* **(b)** *Velocity trend*

Figure 5.19: SME and velocity representations

From the energy trend reported in Figure 5.19(a), two zones of temporary capture of the satellite due to the presence of the massive Earth are evident, a phenomenon more extensively described in [11]. The smaller peaks are related to the time spent on the WOs, while the larger ones are due to gravity assists. In the final part of the transfer, the obtained energy trend confirms the successful ballistic escape.

Figure 5.19(b) helps complete the interpretation of the energy picture of this transfer.

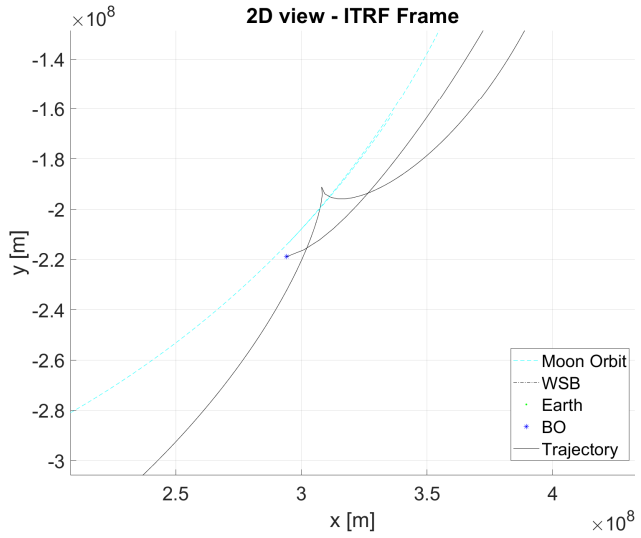

Figure 5.20: WO trajectory - Zoom on MGA

In Figure 5.20, a zoom of the trajectory in its initial phases is depicted. It clarifies that the first energy peak is indeed due to a lunar gravity assist.

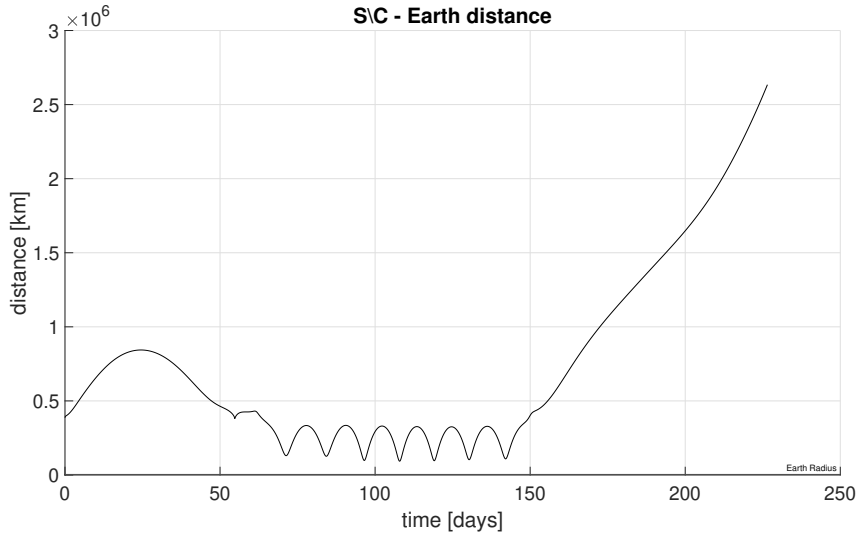

Figure 5.21: WO trajectory - SC-Earth distance

Giving a glance at Figure 5.21, the presence of Earth Gravity Assists is even clearer, and one can simply count six before actually observing the final phase of the transfer coinciding with the spacecraft's departure from the primary body.

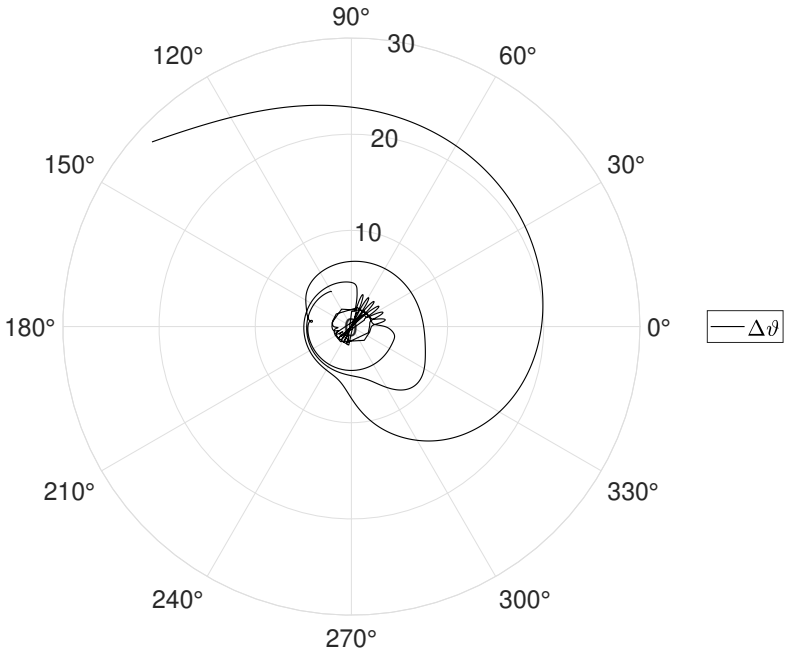

Figure 5.22: WO trajectory - SC-Earth distance

The polar plot in Figure 5.22 is interesting for evaluating the ballistic escape phase. The spacecraft tends to escape when its relative position to the Sun is around 270 degrees and then 150 degrees.

	ΔV [m/s]	In-plane angle ϑ[deg]	Out-of-plane angle φ[deg]	Time of transfer $\mathcal{T}$[days]
21/03/2039	362.5131	135.3429	11.6460	226.5

Table 5.3: Individual for WO trajectory and SME equals to $0.2\text{km}^2/\text{s}^2$

Table 5.3 reports the values related to the individual that generated the trajectory just analyzed: the significant increase in terms of time is evident.

5.4 Ballistic escapes for given values of SME

	ΔV [m/s]	Time of transfer $\mathcal{T}$[days]	Presence of gravity assist	Velocity at escape [m/s]
$\mathscr{C}_3 = 0.2$	357.4652	84.5	YES	730.36
$\mathscr{C}_3 = 0.2$	359.7132	149.0	YES	667.22
$\mathscr{C}_3 = 0.2$	362.5131	226.0	YES	763.34
$\mathscr{C}_3 = 0.2$	370.5233	80.0	NO	646.39
$\mathscr{C}_3 = 0.2$	363.2421	71.5	NO	696.80
$\mathscr{C}_3 = 0.3$	366.8855	134.0	YES	722.66
$\mathscr{C}_3 = 0.4$	367.6164	226.5	YES	848.88
$\mathscr{C}_3 = 0.4$	393.8258	67.5	NO	821.27
$\mathscr{C}_3 = 0.5$	408.4041	221.0	NO	863.08

Table 5.4: List of individuals for different values of SME

Table 5.4 reports the main results obtained by varying the objective function related to the desired final value of specific mechanical energy. In general, the results show that performing a ballistic escape maneuver allows reaching the escape zone with a speed equal to twice the delta-V provided initially. It is possible to assess the effectiveness of this maneuver by estimating the cost of extraterrestrial transfer assuming patched conics model.

5.5 Ballistic escape toward asteroids

In this final section of the present chapter, starting from the results shown in Table 5.4, certain assumptions will be made to simplify the problem and to analyze

an estimation of the impact of a ballistic escape maneuver on an interplanetary mission:

- Planar circular orbit assumed for celestial bodies;
- 2BP-Patched Conics method adopted;
- Optimal conjunction between celestial bodies is assumed to carry out the transfer;
- Hohmann transfer performed;
- Magnitude of the position vector at the starting point equal to the average Earth-Sun distance (one astronomical unit) added to the value of the position vector assumed to identify the WSB in the J2000 reference frame.

For convenience, the basics of the Hohmann transfer (see Figure 5.23) previously analyzed within Section 2.3.3 are summarized below.

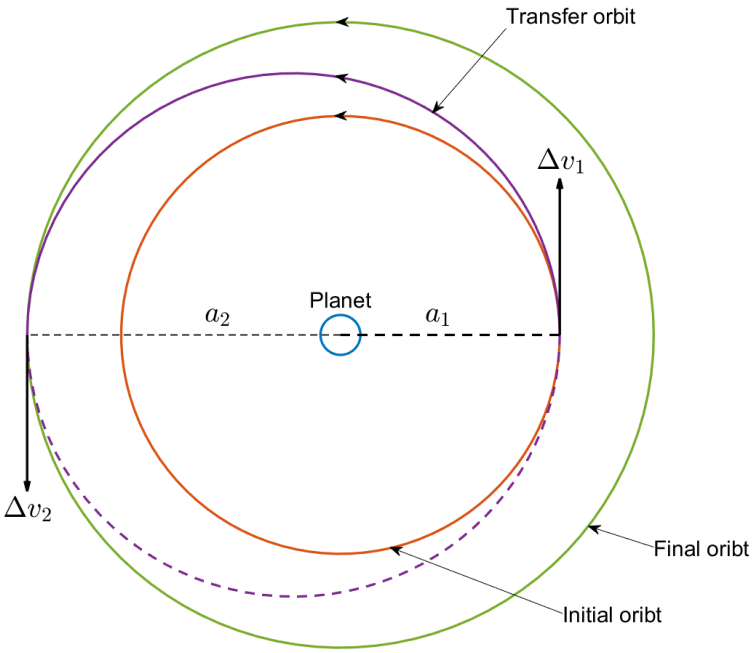

Figure 5.23: Hohmann transfer

Remembering (2.16), the *visviva equation*:

$$\mathscr{E} = \frac{v^2}{2} - \frac{\mu_{\oplus}}{r} + c \tag{5.7}$$

$\mathscr{E}$ varies with height and speed and is zero at the Earth's surface. In astrodynamics c is defined to be zero.

$$\mathscr{E} = \frac{v^2}{2} - \frac{\mu_\oplus}{r} = -\frac{\mu_\oplus}{2a} \tag{5.8}$$

In general, it is possible to calculate the velocity at a point $\bar{v}$ in the orbit from the equation (5.8):

$$\bar{v} = \sqrt{2\left(\mathscr{E} + \frac{\mu_\oplus}{\bar{r}}\right)} \tag{5.9}$$

Velocity of a circular orbit is constant for the orbit itself:

$$v_{circ} = \sqrt{\left(\frac{\mu_\oplus}{r}\right)} \tag{5.10}$$

Because of the perigee and the apogee altitude are known, the semi-major axis of the Hohmann transfer a_H is known too and consequently the time of flight τ:

$$a_H = \frac{r_a + r_p}{2} \tag{5.11}$$

$$T_H = 2\pi\sqrt{\frac{a_H^3}{\mu_\oplus}} \qquad \tau = \frac{T_H}{2} \tag{5.12}$$

At this point, Hohmann's Δv can be calculated as the sum of the two Δv at a and b, defined as the magnitude of the difference in velocity between the orbits at the point.

$$\Delta v_1 = |v_{H,perigee} - v_{circ,1}| \qquad v_{H,perigee} > v_{circ,1} \tag{5.13a}$$

$$\Delta v_2 = |v_{circ,2} - v_{H,apogee}| \qquad v_{H,apogee} < v_{circ,2} \tag{5.13b}$$

$$\Delta v_H = \Delta v_1 + \Delta v_1 \tag{5.14}$$

Exploiting the SOI concept, it may be useful to apply Hohmann for an initial cost estimate of interplanetary manoeuvres by distinguishing between planetocentric and heliocentric phases.

In Figure 5.24, various known (named and unnamed) asteroids reachable with a maximum first delta-V of 12km/s are plotted. Two thresholds are highlighted on the plot:

- the green one set at the value of 0.85km/s, which is equal to the hyperbolic excess velocity reached at escape with a 367.62m/s impulse in lunar orbit (see Table 5.4);
- the second threshold, in red, is set at a value of 3km/s.

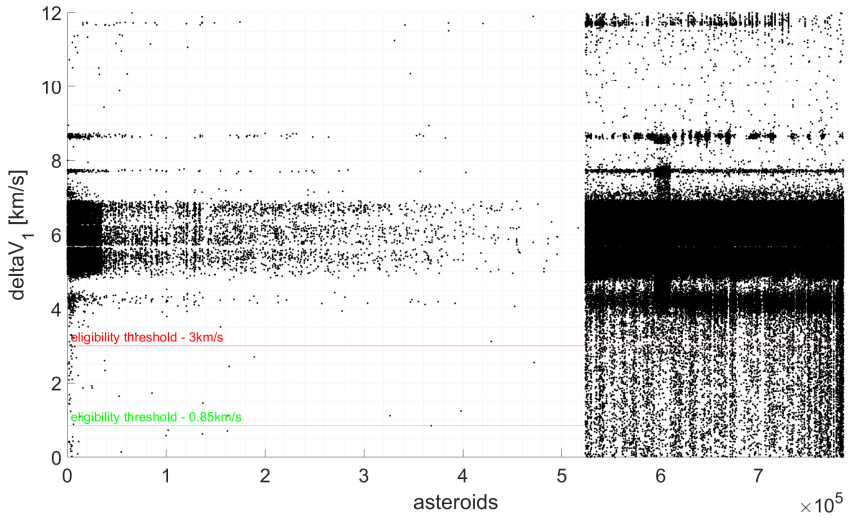

Figure 5.24: Asteroids delta-V treshold

With reference to the first threshold considered, a ballistic transfer would allow reaching 1742 asteroids, reducing, in the worst case, the cost of the first Hohmann delta-V from 0.85km/s to 0.367km/s.

With reference to the first threshold considered, a ballistic transfer would allow reaching 6701 asteroids, covering, in the worst case, 28% of the cost of the first Hohmann delta-V spending only 0.367km/s.

Chapter 6

Conclusion and future steps

In conclusion, this work has focused on the study of a series of escape trajectories from the Earth-Moon binary system constructed in a way to fall within the class of *ballistic escape trajectories*. To identify a proper solution space, a *genetic algorithm* was written capable of directing evolution through ad-hoc merit functions. Starting from a lunar orbit, elite individuals, composed of four genes (delta-V, angle in-plane, angle out-of-plane, propagation time), perturb the orbit triggering the escape maneuver.

In the initial phase, the study was conducted within a simplified physical model (*Planar Circular Restricted Three Body Problem*) in which the concept of *Weak Stability Boundary* is defined. By exploiting this region of gravitational interdiction, it is possible to enable ballistic capture maneuvers towards the primary bodies.

Once an appropriate first attempt delta-V value for reaching the weak stability boundary was identified, the problem was further complicated by using a *High Fidelity Orbit Propagator*, taking into account perturbations such as the non-sphericity of the Earth, solar radiation pressure, the lunisolar effect, and the presence of other celestial bodies in the solar system extracted using the NASA's NAIF SPICE Toolkit. In a model of this type, the influence of the fourth bodies, mainly the Sun, has enabled the possibility of performing a ballistic escape maneuver by exploiting the region of gravitational interdiction previously described as the weak stability boundary.

At the end of the analysis, it became evident that exploiting a low-cost maneuver such as a ballistic one provides a gain, in terms of delta-V and therefore propellant mass, of approximately double compared to a classical maneuver, albeit sacrificing, to some extent, the duration of the transfer.

In any case, following this work, it is evident that the research is not yet complete. Many potential avenues provide opportunities for advancement in the analysis.

- to conduct a precision study to determine the correct launch window for fixed

maneuver durations;

- to carry out a study on the heliocentric phase following the escape phase using the high-fidelity model implemented for this work and to complete the study of missions to Mars or to inner or outer asteroids;
- to deepen the study of the effect of the presence of other celestial bodies along the lines of what was done with the Sun;

In any case, it may be of particular interest to study a low-cost mission from the initial phase (escape maneuver, as done in this thesis) to the final phase, assuming a ballistic capture maneuver towards the target planet and analyzing the feasibility of an aerobraking or aerocapture maneuver for landing on the surface.

Bibliography

[1] Luigi Mascolo. «Low-Thrust Optimal Escape Trajectories from Lagrangian Points and Quasi-Periodic Orbits in a High-Fidelity Model». PhD thesis. Politecnico di Torino, 2023, pp. 1–217 (cit. on pp. 4, 6, 15, 16, 18, 23, 26, 40, 44, 45, 80).

[2] A. L. Fey. «The Status and Future of the International Celestial Reference Frame». In: *Dynamic Planet: Monitoring and Understanding a Dynamic Planet with Geodetic and Oceanographic Tools IAG Symposium Cairns, Australia 22–26 August, 2005*. Ed. by Paul Tregoning and Chris Rizos. Berlin, Heidelberg: Springer Berlin Heidelberg, 2007, pp. 603–609. ISBN: 978-3-540-49350-1. DOI: 10.1007/978-3-540-49350-1_87. URL: https://doi.org/10.1007/978-3-540-49350-1_87 (cit. on p. 5).

[3] Victor Szebehely and R.B. Curran. «The history and background of astrodynamics». In: *Acta Astronautica* 20 (1989), pp. 79–81. ISSN: 0094-5765. DOI: https://doi.org/10.1016/0094-5765(89)90055-6. URL: https://www.sciencedirect.com/science/article/pii/0094576589900556 (cit. on pp. 6, 23).

[4] D.A. Vallado and W.D. McClain. *Fundamentals of Astrodynamics and Applications*. Fundamentals of Astrodynamics and Applications. Microcosm Press, 2001. ISBN: 9781881883128. URL: https://books.google.com/books?id=OCkGmwEACAAJ (cit. on pp. 9, 12, 14, 15).

[5] V.G. Szebehely. *Theory of Orbits, the Restricted Problem of Three Bodies*. Academic Press, 1967. ISBN: 9780126806502. URL: https://books.google.it/books?id=mdTWLrbl3n4C (cit. on pp. 15, 19).

[6] H. Schaub and J.L. Junkins. *Analytical Mechanics of Space Systems*. AIAA education series. American Institute of Aeronautics and Astronautics, Incorporated, 2014. ISBN: 9781624102400. URL: https://books.google.it/books?id=JD3MngEACAAJ (cit. on p. 18).

[7] Elisa Maria Alessi. «The Role and Usage of Libration Point Orbits in the Earth-Moon System». PhD thesis. Oct. 2010 (cit. on p. 22).

[8] George Bozis. «Zero velocity surfaces for the general planar three-body problem». In: *Astrophysics and Space Science* 43 (1976), pp. 355–36. DOI: https://doi.org/10.1007/BF00640013. URL: https://link.springer.com/article/10.1007/BF00640013 (cit. on p. 27).

[9] Luca Biasco Marta Ceccaroni James Biggs. «Analytic estimates and topological properties of the weak stability boundary». In: *Celestial Mechanics and Dynamical Astronomy* 114 (2012), pp. 1–24. DOI: 10.1007/s10569-012-9419-x. URL: https://doi.org/10.1007/s10569-012-9419-x (cit. on p. 30).

[10] Edward Belbruno, Marian Gidea, and Francesco Topputo. «Weak Stability Boundary and Invariant Manifolds». In: *SIAM Journal on Applied Dynamical Systems* 9.3 (2010), pp. 1061–1089. DOI: 10.1137/090780638. eprint: https://doi.org/10.1137/090780638. URL: https://doi.org/10.1137/090780638 (cit. on pp. 30, 32).

[11] Francesco Topputo, Edward Belbruno, and Marian Gidea. «Resonant motion, ballistic escape, and their applications in astrodynamics». In: *Advances in Space Research* 42.8 (2008), pp. 1318–1329. ISSN: 0273-1177. DOI: https://doi.org/10.1016/j.asr.2008.01.017. URL: https://www.sciencedirect.com/science/article/pii/S0273117708000793 (cit. on pp. 30, 33–35, 77, 87).

[12] Edward A. Belbruno and James K. Miller. «Sun-perturbed Earth-to-moon transfers with ballistic capture». In: *Journal of Guidance, Control, and Dynamics* 16.4 (1993), pp. 770–775. DOI: 10.2514/3.21079. eprint: https://doi.org/10.2514/3.21079. URL: https://doi.org/10.2514/3.21079 (cit. on p. 35).

[13] Edward Belbruno. *With Applications to the Construction of Low Energy Transfers*. Princeton: Princeton University Press, 2004. ISBN: 9780691186436. DOI: doi:10.1515/9780691186436. URL: https://doi.org/10.1515/9780691186436 (cit. on p. 35).

[14] E. Belbruno. *Fly Me to the Moon : An Insider's Guide to the New Science of Space Travel*. Princeton: Princeton University Press, 2007. ISBN: 9781400849192 (cit. on p. 35).

[15] Francesco Topputo, Massimiliano Vasile, and Franco Bernelli-Zazzera. «Low Energy Interplanetary Transfers Exploiting Invariant Manifolds of the Restricted Three-Body Problem». In: *Journal of the Astronautical Sciences* 53 (Oct. 2005), pp. 353–372. DOI: 10.1007/BF03546358 (cit. on p. 35).

[16] Jerry E. White Roger R. Bate Donald D. Mueller. *Fundamentals of astrodynamics*. 1st ed. Dover Publications, 1971. ISBN: 9780486600611; 0486600610 (cit. on pp. 35, 38).

[17] Benjamin Stahl and Robert Braun. «Low-Thrust Trajectory Optimization Tool to Assess Options for Near-Earth Asteroid Deflection». In: *AIAA/AAS Astrodynamics Specialist Conference and Exhibit* (Aug. 2008). DOI: 10.2514/6.2008-6255 (cit. on p. 36).

[18] Meysam Mahooti. *High Precision Orbit Propagator*. https://www.mathworks.com/matlabcentral/fileexchange/55167-high-precision-orbit-propagator. [Online; accessed June 20, 2023]. 2023 (cit. on p. 39).

[19] *Jet Propulsion Laboratory Solar System Dynamics. JPL Planetary and Lunar Ephemerides: Export Information, 2020.* URL: https://ssd.jpl.nasa.gov/planets/eph_export.html (cit. on p. 39).

[20] Luigi Mascolo and Lorenzo Casalino. «Optimal Escape from Sun-Earth and Earth-Moon L2 with Electric Propulsion». In: *Aerospace* 9 (Apr. 2022), p. 186. DOI: 10.3390/aerospace9040186 (cit. on pp. 39, 40).

[21] Francesco Simeoni, Lorenzo Casalino, Alessandro Zavoli, and Guido Colasurdo. «Indirect Optimization of Satellite Deployment into a Highly Elliptic Orbit». In: *International Journal of Aerospace Engineering* 2012 (May 2012). DOI: 10.1155/2012/152683 (cit. on p. 40).

[22] *GRACE Gravity Model 03 - Released 2008*. URL: https://www2.csr.utexas.edu/grace/gravity/ggm03/ (cit. on p. 42).

[23] Günter Seeber. *Satellite Geodesy*. Berlin, New York: De Gruyter, 2003. ISBN: 9783110200089. DOI: doi:10.1515/9783110200089. URL: https://doi.org/10.1515/9783110200089 (cit. on pp. 42, 43).

[24] *GRACE*. URL: https://www.jpl.nasa.gov/missions/gravity-recovery-and-climate-experiment-grace (cit. on p. 44).

[25] Oliver Montenbruck and Eberhard Gill. *Satellite Orbits*. Vol. 1. Jan. 2000. ISBN: 978-3-540-67280-7. DOI: 10.1007/978-3-642-58351-3 (cit. on p. 45).

[26] Meysam Mahooti. *Runge-Kutta-Fehlberg (RKF78)*. https://www.mathworks.com/matlabcentral/fileexchange/61130-runge-kutta-fehlberg-rkf78. [Online; accessed June 20, 2023]. 2024 (cit. on p. 46).

[27] Erwin Fehlberg and George C. Marshall. «Low-order classical Runge-Kutta formulas with stepsize control and their application to some heat transfer problems». In: 1969. URL: https://api.semanticscholar.org/CorpusID:117960134 (cit. on p. 46).

[28] Colin F. Mayo. «Implementation of the Runge-Kutta-Fehlberg method for solution of ordinary differential equations on a parallel processor». PhD thesis. Naval Postgraduate School, 1987, pp. 14–15 (cit. on p. 46).

[29] Erwin Fehlberg. «Classical Fifth-, Sixth-, Seventh-, and Eighth-Order Runge-Kutta Formulas with Stepsize Control». In: 1968. URL: https://api.semanticscholar.org/CorpusID:117616857 (cit. on pp. 47, 48).

[30] Vladislav N. Kovalnogov, Ruslan V. Fedorov, Tamara V. Karpukhina, Theodore E. Simos, and Charalampos Tsitouras. «Runge–Kutta Embedded Methods of Orders 8(7) for Use in Quadruple Precision Computations». In: *Mathematics* 10.18 (2022). ISSN: 2227-7390. DOI: 10.3390/math10183247. URL: https://www.mdpi.com/2227-7390/10/18/3247 (cit. on p. 48).

[31] *SPICE Tutorials*. NASA. 2023 (cit. on p. 50).

[32] F. Mazzeo. «Utilizzo di algoritmi genetici per ottimizzazioni di trasferimenti interplanetari a bassa spinta». Università Degli Studi di Pisa, 2008 (cit. on pp. 53–56, 64).

[33] Wenyu Sun and Ya-xiang Yuan. «Optimization theory and methods. Nonlinear programming». In: 1 (Jan. 2006). DOI: 10.1007/b106451 (cit. on p. 54).

[34] Marc Sevaux. «Metaheuristics: strategies for the optimisation of the production of goods and services». In: (July 2004) (cit. on p. 55).

[35] Anil Rao. «A Survey of Numerical Methods for Optimal Control». In: *Advances in the Astronautical Sciences* 135 (Jan. 2010) (cit. on p. 55).

[36] Bruce Conway. «A Survey of Methods Available for the Numerical Optimization of Continuous Dynamic Systems». In: *J. Optimization Theory and Applications* 152 (Feb. 2012), pp. 271–306. DOI: 10.1007/s10957-011-9918-z (cit. on p. 55).

[37] Anil Rao. «Trajectory Optimization: A Survey». In: *Lecture Notes in Control and Information Sciences* 455 (Mar. 2014), pp. 3–21. DOI: 10.1007/978-3-319-05371-4_1 (cit. on p. 55).

[38] John T. Betts. «Survey of Numerical Methods for Trajectory Optimization». In: *Journal of Guidance, Control, and Dynamics* 21.2 (1998), pp. 193–207. DOI: 10.2514/2.4231. eprint: https://doi.org/10.2514/2.4231. URL: https://doi.org/10.2514/2.4231 (cit. on p. 55).

[39] Kristina Alemany and Robert Braun. «Survey of Global Optimization Methods for Low-Thrust, Multiple Asteroid Tour Missions». In: *Advances in the Astronautical Sciences* 127 (Jan. 2007) (cit. on pp. 55, 56).

[40] G. Radice, Massimiliano Vasile, and P Dilizia. «Advanced Global Optimisation Tools for Mission Analysis and Design». In: () (cit. on p. 57).

[41] Pierluigi Di Lizia, G. Radice, Dario Izzo, and Massimiliano Vasile. «On the Solution of Interplanetary Trajectory Design Problems by Global Optimisation Methods». In: Jan. 2005 (cit. on p. 57).

[42] David E. Goldberg and Jon Richardson. «Genetic algorithms with sharing for multimodal function optimization». In: *Proceedings of the Second International Conference on Genetic Algorithms on Genetic Algorithms and Their Application*. Cambridge, Massachusetts, USA: L. Erlbaum Associates Inc., 1987, pp. 41–49. ISBN: 0805801588 (cit. on p. 58).

[43] Zbigniew Michalewicz and Marc Schoenauer. «Evolutionary Algorithms for Constrained Parameter Optimization Problems». In: *Evolutionary Computation* 4.1 (1996), pp. 1–32. DOI: 10.1162/evco.1996.4.1.1 (cit. on p. 58).

[44] G.N. Vanderplaats. *Numerical Optimization Techniques for Engineering Design*. McGraw-Hill series in mechanical engineering. Vanderplaats Research and Development, Incorporated, 2001. ISBN: 9780944956014. URL: https://books.google.it/books?id=vN4mAQAACAAJ (cit. on p. 59).

[45] Matthew Vavrina and Kathleen Howell. «Global Low-Thrust Trajectory Optimization Through Hybridization of a Genetic Algorithm and a Direct Method». In: Aug. 2008. ISBN: 978-1-62410-001-7. DOI: 10.2514/6.2008-6614 (cit. on p. 59).

[46] Aida Mirniazmandan, Matin Alaghmandan, Farzad Barazande, and Ehsan Rahimianzarif. «Mutual effect of geometric modifications and diagrid structure on structural optimization of tall buildings». In: *Architectural Science Review* 61 (May 2018). DOI: 10.1080/00038628.2018.1477043 (cit. on p. 60).

[47] Vijay Chahar, Sourabh Katoch, and Sumit Chauhan. «A Review on Genetic Algorithm: Past, Present, and Future». In: *Multimedia Tools and Applications* 80 (Feb. 2021). DOI: 10.1007/s11042-020-10139-6 (cit. on pp. 61, 67, 68, 70).

[48] Joon-Yong Lee, Min-Soeng Kim, Cheol-Taek Kim, and Ju-Jang Lee. «Study on encoding schemes in compact genetic algorithm for the continuous numerical problems». In: Oct. 2007, pp. 2694–2699. DOI: 10.1109/SICE.2007.4421447 (cit. on p. 61).

[49] S. Sivanandam and S N Deepa. *Introduction to Genetic Algorithms*. Jan. 2008. ISBN: 978-3-540-73189-4. DOI: 10.1007/978-3-540-73190-0 (cit. on p. 61).

[50] Stanley Lima and Sidnei Araújo. «A New Binary Encoding Scheme in Genetic Algorithm for Solving the Capacitated Vehicle Routing Problem». In: May 2018, pp. 174–184. ISBN: 978-3-319-91640-8. DOI: 10.1007/978-3-319-91641-5_15 (cit. on p. 61).

[51] B.R. Fox and M.B. McMahon. «Genetic Operators for Sequencing Problems». In: ed. by GREGORY J.E. RAWLINS. Vol. 1. Foundations of Genetic Algorithms. Elsevier, 1991, pp. 284–300. DOI: https://doi.org/10.1016/B978-0-08-050684-5.50021-5. URL: https://www.sciencedirect.com/science/article/pii/B9780080506845500215 (cit. on p. 61).

[52] Khalid Jebari. «Selection Methods for Genetic Algorithms». In: *International Journal of Emerging Sciences* 3 (Dec. 2013), pp. 333–344 (cit. on pp. 62, 67, 70).

[53] Edward Belbruno and John Carrico. «Calculation of weak stability boundary ballistic lunar transfer trajectories». In: Aug. 2000. DOI: 10.2514/6.2000-4142 (cit. on p. 65).

[54] Kalyan Deb. «Multiobjective Optimization Using Evolutionary Algorithms. Wiley, New York». In: Jan. 2001 (cit. on p. 66).

[55] J. Fossen. «Analysis of the porkchop plot considering eccentric and inclined planetary orbits». Politecnico di Milano, 2022 (cit. on p. 74).